NORTHWESTERN UNIVERSITY

Unconventional Approaches to High Throughput Nanolithography and
3D Printing

A DISSERTATION

SUBMITTED TO THE GRADUATE SCHOOL
IN PARTIAL FULFILLMENT OF THE REQUIREMENTS

for the degree

DOCTOR OF PHILOSOPHY

Field of Chemical and Biological Engineering

By

James Lupton Hedrick III

EVANSTON, ILLINOIS

June 2019

Abstract

Unconventional Approaches to High Throughput Nanolithography and 3D Printing.

James Lupton Hedrick III

This thesis centers around the development and application of novel high throughput lithography tools. These advances help: 1) establish the field of nanocombinatorics, where massive libraries (termed megalibraries) of materials can be prepared in a positionally encoded manner and then screened for functional activity, and 2) advance stereolithographic 3D printing of materials by increasing the throughput, materials compatibility, and the size of the structures that can be made. The latter has significant implications for using 3D printing in the field of manufacturing. The first four chapters focus primarily on developing nanolithography systems to better study the properties of nanostructures as a function of size and composition. Chapter 5 shifts from the nanoscale to the macroscale by building off the findings in the previous chapters and applying it to stereolithography. Finally, Chapter 6 looks towards the future of lithography and the next possible steps in the progression of these and related lithographic tools.

Chapter 1 introduces cantilever-free scanning probe lithography (CF-SPL) as a powerful tool in the emerging field of nanocombinatorics. At the nanoscale, small changes in the size and composition of materials can dramatically affect their chemical reactivity, catalytic activity, energy capture capabilities, and mechanical properties. To probe material properties at these length scales, specialized tools are needed for both synthesizing and characterizing them. In addition to

controlling size and composition, new tools must be developed to efficiently probe the possible combinations. The development of CF-SPL techniques has allowed inexpensive, reproducible, and high throughput patterning of both hard and soft nanomaterials over large areas (> 1 cm^2).

Chapter 2 addresses the problem of patterning uniformity and density limitations that have traditionally limited CF-SPL. Polymer pen lithography (PPL) utilizes an array with millions of pyramidal pens to deposit single attoliter features on a surface. However, the pen array is composed of a soft polymer that results in increased feature sizes due to poor control over the force applied by the pens on the surface. Extending this technology to include a hard-transparent array that exhibits a force-independent contact area improves its patterning capability by reducing the minimum feature size (~40 nm), minimum feature pitch (<200 nm for polymers), and pen-to-pen variation.

Chapter 3 examines the use of CF-SPL to create megalibraries and its implication on the field of nanocombinatorics and materials discovery. The ability to synthesize millions of particles on a single 4 cm^2 chip in parallel creates an unprecedented way to explore the materials genome. This is done through a dual spray coating approach to deliver ink to polymer pen lithography (PPL) arrays in which combinatorial libraries with size and composition gradients can be synthesized, creating a platform for printing complex nanoarrays for screening. Combining this new inking system with a materials synthetic strategy such as scanning probe block copolymer lithography (SPBCL) enables the printing of nanoparticle libraries, with features that systematically vary in terms of size and composition. Such libraries then can be screened for different properties. The nanoparticle library can include structures composed of single metals, metal oxides, multimetallic

alloys, and janus structures. This novel approach enables the synthesis and screening of an extraordinarily large material parameter space.

Chapter 4, like Chapter 2, addresses the problem of patterning uniformity and density limitations that have traditionally been inherit to CF-SPL with systems that deliver energy rather than materials. Beam pen lithography (BPL) is built upon platform related to PPL, but where the tips are used as light guides to pattern photochemically. Pen-to-pen height variation from the array fabrication process results in non-uniform apertures, a major problem that limited the wide-spread use of BPL. Previous aperture fabrication methods relied on spin coating photoresist onto uniform arrays which works to some extent for thousands of pens but no longer possible when scaling to millions of pens in a single array. To overcome this problem, a new type of etching technique was invented to make more uniform apertures: liquid mask etching. Utilizing a liquid mask enables the protection of the BPL arrays in a uniform way regardless of height. This results in the synthesis of 2.84 million uniform apertures with sizes as low as 250 nm. These new arrays are then used in the development of a CF-SPL nano 3D printer that utilizes the liquid mask as protection during printing.

Chapter 5 builds on the nano 3D printer from Chapter 4 but takes it out of the CF-SPL system and explores it in the opposite end of the length scale spectrum. With High Area Rapid Printing (HARP), it is possible to fabricate 3D printed parts at an unprecedent rate. As a proof-of-concept, a printer utilizing HARP was built with continuous vertical print rates exceeding 430 mm/hr with a record-breaking throughput of 3.75 ft^3/hr.

Chapter 6 discusses the future of CF-SPL and HARP. There is a bright future for both nanolithography and additive manufacturing. While neither are in their infancy, both can still dramatically change our lives.

Acknowledgements

First, I would like to thank my advisor Professor Chad Mirkin. Over the course of my PhD, Chad has given me the tools necessary to succeed as a researcher. Chad has given me the right mixture of independence and guidance to take new ideas and distill them into proof-of-concept and significant scientific and engineering advances. I have become a better scientist and engineer during the time spent in his lab. While some of our debates have gotten heated over the years, I know I am better for it. I thank Professor Donna Jurdy. She has been a great source of advice, especially in my endeavors outside of my primary studies. I appreciate all of the support you gave me in pursuing space research and attempts at the astronaut program. I enjoyed being able to talk about science that interested me that was outside the scope of my PhD. I thank Professor Vinayak Dravid. There was never a conversation that we had where I did not leave without a smile on my face. I thank my additional committee members Professor Wesley Burghardt and Professor Justin Notestein. The advice I received was incredibly helpful and always pushed me to become better.

I have had the pleasure to work with phenomenal researchers during my PhD tenure. My achievements would not have been possible without the great group of colleagues, mentors, and mentees including David Walker, Keith Brown, Maria Cabezas, Ed Kluender, Andrey Ivankin, Brian Meckes, and PC Chen. Many discussions, late nights, and whiteboard brainstorming sessions have been had as well as sky diving, paintball, and great meals. Furthermore, long lasting friendships have been formed. The dip-pen nanolithography subgroup has been a great resource for me. It was always a place to test my ideas and help me poke holes into them to make sure I spent my time as wisely as possible.

Outside of my group, I have made many friends in my department. The Peanuts intramurals teams have been a great stress reliever and place to make friends. It was a real joy to play with and captain teams to victories and championships.

I need to thank my investors and employees at CDJ Technologies, Inc/Azul 3D. It has been a wonderful experience seeing an idea go from conception to reality in the lab and then transitioned to a commercialized product. To have an amazing group of people believe in the technology and the future that is possible is one of the most gratifying parts of my PhD experience. Having employees that put their heart and souls into their work and have moved across the country and globe to help take an idea and make it reality is an amazing experience. Not everyone has the opportunity to have this experience and even fewer take it. It never would have been possible if I did not go to Northwestern.

Finally, I thank my family. Without them, none of this would have been possible. Starting with the push to get me to apply to a PhD my senior year at MIT, my parents have been a constant source of strength. They have talked to me for hundreds of hours on the phone, helping me to work through my ideas and keep me company on my bike rides to and from work. My wife has had to learn patience as this thesis has been a long time coming. She has listened to my presentation so many times she could probably give it better than I did. Late nights, coming home, well past the time she would like to have gone to sleep and still making me dinner because I made a stupid rule of no dinner until I finish lab work for the night. I always thought it might help push me to end early, but little did I know it would just mean dinner was at 10 pm every night. I cannot not thank my family enough for supporting me every step of the way. Without them, none of this would have been possible.

This dissertation is dedicated to my family and my wife.

Table of Contents

List of Figures and Schemes

1. Chapter One

Nanocombinatorics with Cantilever-Free Scanning Probe Arrays

Reprinted/adapted with permission from Brown†, K.A.; Hedrick†, J. L.; Eichelsdoerfer, D. J.; Mirkin, C. A., "Nanocombinatorics with Cantilever-Free Scanning Probe Arrays." ACS Nano 2019, 13, 8-17. Copyright 2019 American Chemical Society.

1.1. Cantilever-free Scanning Probe Lithography

One of the cornerstone advantages inherent to nanotechnology is that miniaturized systems occupy less space, and therefore extraordinarily large numbers of components can occupy small areas.[1-3] The semiconductor industry has taken full advantage of this fact by continually increasing the areal density of electrical devices in microelectronics to the point where each processor now contains billions of transistors.[4] From a research perspective, this scaling presents major opportunities because it, in principle, allows one to multiplex experimental conditions to perform classes of experiments that involve too many permutations to be undertaken at the bench-top scale. While miniaturization is important from an efficiency perspective, materials that are nanometer-scale can exhibit properties that differ from those observed at the bulk scale. For example, nanometer-scale metallic nanoparticles exhibit enhanced activity as heterogeneous catalysts and nanoscale domains of biomolecules can cooperatively interact with biological cells to dictate the formation of focal adhesions, which in turn, can affect important processes like differentiation.[5, 6] This field that involves the massive parallelization of experimental conditions at the nanoscopic scale where properties emerge is known as nanocombinatorics or combinatorial nanoscience.[7] Due to the wide range of applications of nanotechnology, this field is ideally suited to address questions that require screening enormous numbers of experimental conditions in fields including biotechnology, catalysis, and nanoelectronics.

The success of combinatorial nanoscience experiments, and consequently the major challenges in this field, are dictated by how effectively nanomaterials can be *synthesized* and *screened*. Two areas where this challenge is abundantly clear are catalysis and tissue engineering. In heterogeneous catalysis, it has been shown that nanoparticles can exhibit higher activity than

one would expect based upon their surface area.[5, 8] This synergistic effect has been hypothesized

to arise from a number of sources including the curvature of the surface or high densities of grain

boundaries. However, understanding the origins of this enhancement, or simply finding the optimal

nanoparticle to catalyze a given reaction, has been a major challenge due to the difficulty inherent

in preparing large numbers of particles that only differ by a single parameter (*e.g.* composition or

size). In the case of tissue engineering, it is known that interactions between cells and the

extracellular matrix can dictate the phenotype and even differentiation pathway of those

cells.[6, 7, 9] While myriad experiments have explored the behavior of cells on a variety of

surfaces,[10, 11] culture-to-culture variations complicate interpretation of these experiments.

Furthermore, patterning multiple biological materials on the scale of individual focal adhesions is

difficult because conventional patterning techniques used in microelectronics processing are not

biocompatible due to their reliance on harsh acids, bases, and organic solvents. These two fields,

catalysis and tissue engineering, represent major candidates for nanocombinatorics as they (1)

exhibit important features at the nanoscale and (2) have enough experimental parameters that they

require massive numbers of experiments to fully elucidate phenomena.

In this chapter, we overview cantilever-free scanning probe lithography (CF-SPL) as a

collection of synthetic processes that enable nanocombinatoric experiments by addressing the

challenge of making large-scale arrays of nanoscale soft materials. Conceptually, CF-SPL

represents the convergence of soft lithography[12] and scanning probe lithographic techniques such

as dip-pen nanolithography (DPN) where, instead of a cantilever supporting a single pen, an

elastomeric film on a rigid backing layer supports a massive array of pens (Figure 1.1A). [13-15]

Initially, CF-SPL was developed as a process for parallelizing DPN in a manner that addressed the

throughput challenge associated with serial scanning techniques. While DPN was parallelized through the development of cantilever arrays,[16-18] the widespread applicability of these approaches were limited by the reliance on delicate structures made through complex micromachining. The first CF-SPL approach is known as polymer pen lithography (PPL) and utilizes a massive array (11 million pens were initially demonstrated) of elastomeric pens to define patterns using a material transfer process analogous to DPN.[15] Based upon this architectural advance, a host of experiments and protocols have been made possible, including those that achieve nanoscale feature resolution across centimeter-scales – patterns that represent control over *seven orders of magnitude in length or 14 orders of magnitude in area*.[19-21] This advance is particularly relevant for nanocombinatorics as CF-SPL allows one to rapidly and arbitrarily pattern hard and soft materials with nanometer-scale features over large spatial scales. Previous reviews touched on how material transport in CF-SPL differs from transport in DPN[22, 23] or the evolution of CF-SPL.[19-21, 24] Herein, we review recent progress and future directions of this discovery platform with a specific focus on the scientific questions that can be addressed using CF-SPL to perform nanocombinatorial experiments. As case studies, we discuss recent advances in understanding nanoparticle-based heterogeneous catalysis and directing the differentiation of stem cells with nanopatterned surfaces.
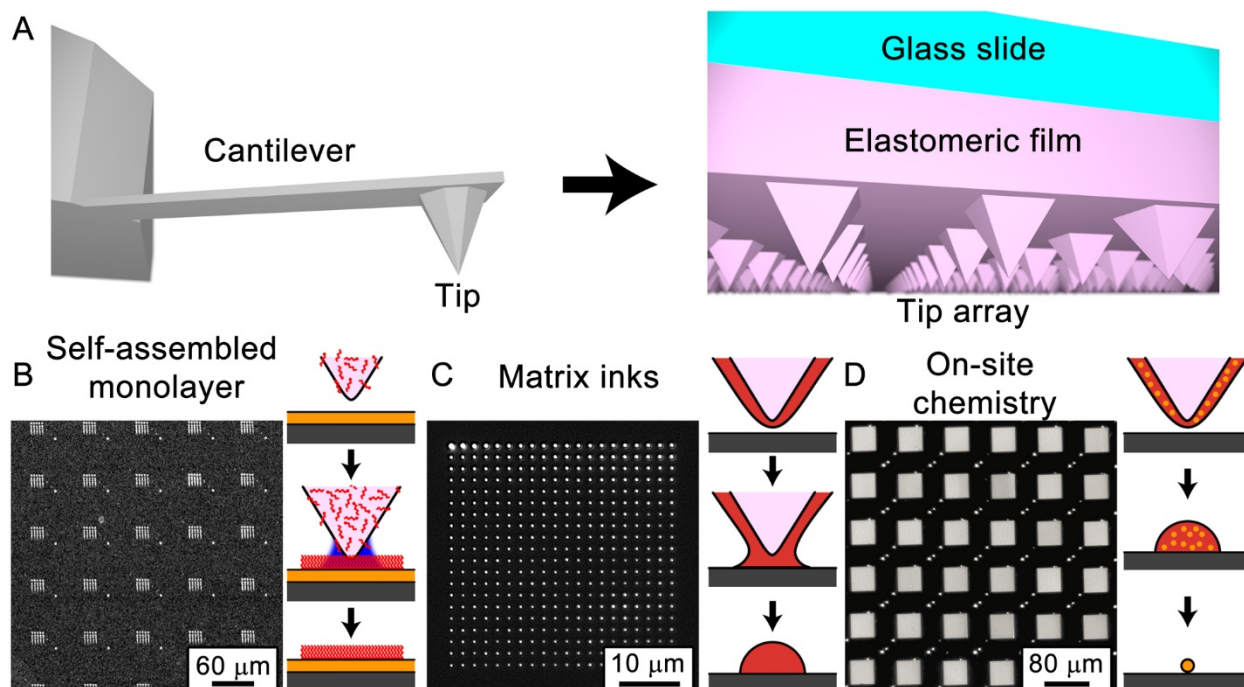
Figure 1.1. Cantilever-free scanning probe lithography (CF-SPL). (A) Schematic showing the evolution from a cantilever-based scanning probe with a single tip to an array of probes resting on an elastomeric film on a glass slide. (B) Schematic and electron micrograph depicting self-assembled monolayers printed using CF-SPL.[25] From ref (25). Copyright 2010 Wiley-VCH Verlag GmbH & Co. KGaA, Weinheim. Reproduced by permission of John Wiley & Sons, Inc. (C) Schematic and fluorescence image depicting matrix-ink features printed using CF-SPL.[26] Reprinted with permission from ref (26). Copyright 2013 American Chemical Society. (D) Schematic and electron micrograph depicting on-site chemistry being performed in features printed by CF-SPL, specifically, the synthesis of single metal nanoparticles in polymer nanoreactors.[27] Reprinted with permission from ref (27). Copyright 2010 National Academy of Sciences.

1.2. Directly Writing Materials with CF-SPL

The principal reason that CF-SPL probes are enabling tools for combinatorial nanoscience is that they can be used to directly write patterns of a specified "ink" on a surface. In this arena, CF-SPL benefits from a large body of work wherein DPN has been used to pattern myriad materials including biological molecules such as DNA or proteins, magnetic nanostructures, nanoparticles, viruses, and polymers.[28-37] Much like the invention of DPN,[38] material transport using CF-SPL was first demonstrated through writing self-assembled monolayers (SAMs)

composed of the small molecule 16-mercaptohexadecanoic acid (MHA) onto gold surfaces using PPL (Figure 1.1B).[15, 39] The initial focus on SAM-forming molecules was due to the fact that small molecules are an important class of inks that represent a modular way of defining surface chemistry. Specifically, PPL-patterned SAMs have been used for applications such as immobilizing proteins,[7] nanoparticles,[40] directing the surface-initiated growth of polymers to produce microelectrode arrays,[41] and preparing anti-fouling surfaces.[42]

While SAM-forming molecules are a modular way of dictating surface chemistry, it is often advantageous to directly write more complex or diverse materials. An alternate paradigm for direct writing utilizes inks containing water soluble polymers such as polyethylene glycol (PEG) with typical molecular weights of ~2 kDa.[23, 43] Such polymers are an important class of patterning material because they can be used as a vehicle for the transport (or "matrix") of larger materials such as nanoparticles (Figure 1.1C).[43, 44] Phospholipids and cholesterol have also been used as a matrix for the deposition of nanomaterials.[45] Furthermore, matrix materials can be engineered to bind to the material of interest, a principle which was demonstrated by using the block copolymer poly(ethylene oxide)-*b*-poly(vinylpyridine) to transport metal salts onto surfaces in a process known as scanning probe block copolymer lithography (SPBCL).[27, 46] Interestingly, SPBCL highlights a use of polymers beyond acting as a matrix for transport as the deposited polymer features can also serve as nanoreactors that facilitate chemical reactions such as the synthesis of inorganic nanoparticles[27] or Staudinger ligation (Figure 1.1D).[47]

It is important to note that the soft material composition of PPL pen arrays also make them capable of patterning materials that cannot be patterned using conventional DPN. Specifically, it has been found that nonpolar solvents can be absorbed into the pen array to allow the patterning

of water insoluble materials such as poly(styrene)-*b*-poly(vinylpyridine).[26] In this way, CF-SPL provides greater materials diversity than DPN.

1.3. Control over feature size with CF-SPL

With any discussion of a patterning technique, it is important to address the ability to control the size of the patterned features. Due to the fact that depositing small molecules from a scanning probe is understood to be a diffusion process,[48] the principal experimental factor used to control feature size is dwell time.[38, 48] In the case of patterning polymeric or liquid inks, transport can be understood to be a fluid flow[34, 49] and retraction speed can be used as an additional parameter to dictate feature size.[50] Elastomeric pens, as used in PPL, add an additional factor for controlling feature size as the pens themselves may deform, resulting in a force-dependent contact area between the pen and surface.[51, 52] Furthermore, the ability to locally control pressure allows the exploration of tip-directed chemistry: for example, force has been used to control the kinetics of the Huisgen reaction[53] as well as the Diels-Alder reaction.[54] While a force-dependent feature size indicates that pen arrays must be level with respect to the patterning surface in order to write uniform arrays of features, the force-distance relationship is predictable, thus providing a way for algorithmically leveling the pen array with respect to the surface.[55-57]

While leveling a pen array with respect to a surface is important for uniform patterning, one advantage of PPL in the context of nanocombinatorics is that deliberately tilting an array with respect to a surface will generate gradients in feature size (Figure 1.2A).[7] This capability was later verified to also allow a gradient of lipid features to be patterned in a single process.[58] The ability for a uniform array of pens to generate a predictably non-uniform array of features is a critical aspect for performing nanocombinatorics. Beyond gradients of feature sizes, ideally, one would

be able to generate arbitrary features with each pen independently. Borrowing techniques from the microfluidics community,[59, 60] pressurized microchannels can actuate individual pens by moving them in and out of contact with a surface.[61, 62] However, the scalability of this method is poor as separate pneumatic controls are required for each pen. In contrast, local thermal actuation can be used to reliably actuate pens by taking advantage of the high coefficient of thermal expansion inherent to elastomers (Figure 1.2B).[63, 64] Strikingly, this method can be used to move pens at speeds over 300 μm/s through distances of several micrometers using powers commensurate with those required to operate cantilever-based probes that are thermally actuated,[65, 66] thereby making it an appealing method for facile large-scale pen actuation. Recently, a method was demonstrated that further improved on the scalability of actuation wherein the pen array was rendered partially opaque through the inclusion of carbon-nanotubes into the elastomeric support and local light absorption was used to actuate pens.[67] This photothermal method was shown to be able to move pens up to three micrometers out of plane using modest illumination intensities, providing a path towards massively parallel actuation.
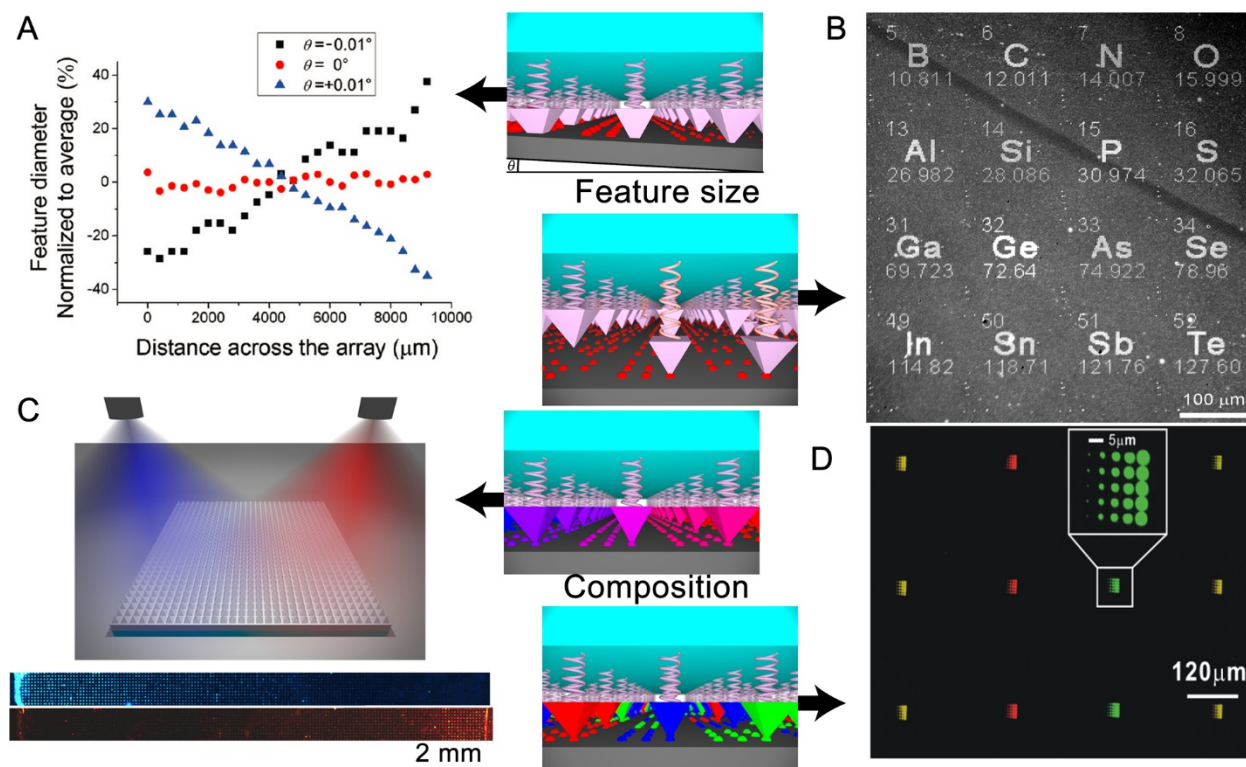
Figure 1.2. Printing features that vary in size and composition with CF-SPL. (A) Tilting the pen array with respect to the surface allows one to synthesize features whose sizes vary across the sample.[25] From ref (25). Copyright 2010 Wiley-VCH Verlag GmbH & Co. KGaA, Weinheim. Reproduced by permission of John Wiley & Sons, Inc. (B) Thermally actuating individual tips allows for printing arbitrary features and stitching together patterns written by multiple pens.[68] Reprinted with permission from ref (68). Copyright 2013 National Academy of Sciences. (C) Spray-coating the pen array with different inks from multiple nozzles allows for a gradient of ink compositions to be written using a single pen array.[69] Reprinted with permission from ref (69). Copyright 2018 National Academy of Sciences. (D) Ink-jet printing can be used to ink individual pens such that patterns with arbitrary compositions can be written.[70] From ref (70). Copyright 2009 Wiley-VCH Verlag GmbH & Co. KGaA, Weinheim. Reproduced by permission of John Wiley & Sons, Inc.

1.4. Control over feature composition with CF-SPL

In addition to controlling feature size, it is necessary to control feature composition. Both drop casting and spin coating have been successfully used to introduce a uniform quantity of ink across arrays for patterning single-material patterns.[15, 39] While patterns of a single material are

important for some applications, intentionally synthesizing patterns with spatially heterogeneous compositions is more powerful from a combinatorial perspective. Toward this end, recent work has shown that by spraying different ink solutions from multiple nozzles onto a pen array, pens can be inked with a continuous linear compositional gradient in a manner that allows compositional gradients to be synthesized using PPL (Figure 1.2C).

Typically, the pen-to-pen spacing in CF-SPL is tens of micrometers, allowing direct inking *via* low resolution additive methods. For example, inkjet printing can be used to deposit inks into a periodic array of wells. Subsequent dipping of a PPL pen array into these wells allows for independent control over the ink coating each pen in the array, a process that has been used to pattern multi-component protein arrays (Figure 1.2D).[71] Integrated microfluidics can also be used to automatically fill such ink wells.[72, 73] Additionally, one can microcontact print as well as pipette inks onto large regions of the array to specify the ink composition for predetermined blocks of pens.[74, 75] These approaches have allowed PPL-based experiments to pattern chemically inhomogeneous patterns to serve as stamp pads for subsequent functionalization[76] and for direct writing onto microdevices.[77] It is worth emphasizing that the ability to directly write dissimilar soft materials in coordinated nanoscale regions is a key advantage of CF-SPL as it is difficult if not impossible to achieve by other techniques, especially those that require sequential exposure and development processes.

1.5. Pen array architectures

An important advantage of the cantilever-free architecture is that pen arrays themselves are modular: pen composition can be chosen to obtain desired printing properties. Originally, the pens and elastomeric backing film were composed of either commercially available

polydimethylsiloxane (PDMS) or a stiffer formulation known as hard PDMS (Figure 1.3A).[15, 39] Pens composed of PDMS have also been modified to include PEG to allow them to better absorb water for humidity-independent patterning.[78] Other polymers besides PDMS have been explored, and stiffer polymers result in a slightly decreased sensitivity to applied force in terms of feature size.[79] Building on this realization, by making a polymer pen array composed of two elastomers of different moduli (*i.e.* the pens are stiffer than the backing layer), it is possible to reduce the sensitivity to tip-sample extension and more reliably print small features.[80] More drastic alterations to pen array architecture have been explored including making the pens different heights to encode a distribution of feature sizes,[81] or using close packed spherical microparticles as pens.[82] Finally, the planar architecture of these pen arrays allow them to be easily coated with graphene, a process which renders them conductive and reduces wear during tip-sample contact.[83] Interestingly, the idea of coating pen arrays has translated to the biological realm where enzyme-coated pen arrays have been used to drive chemical transformations in a contact-dependent manner.[84]
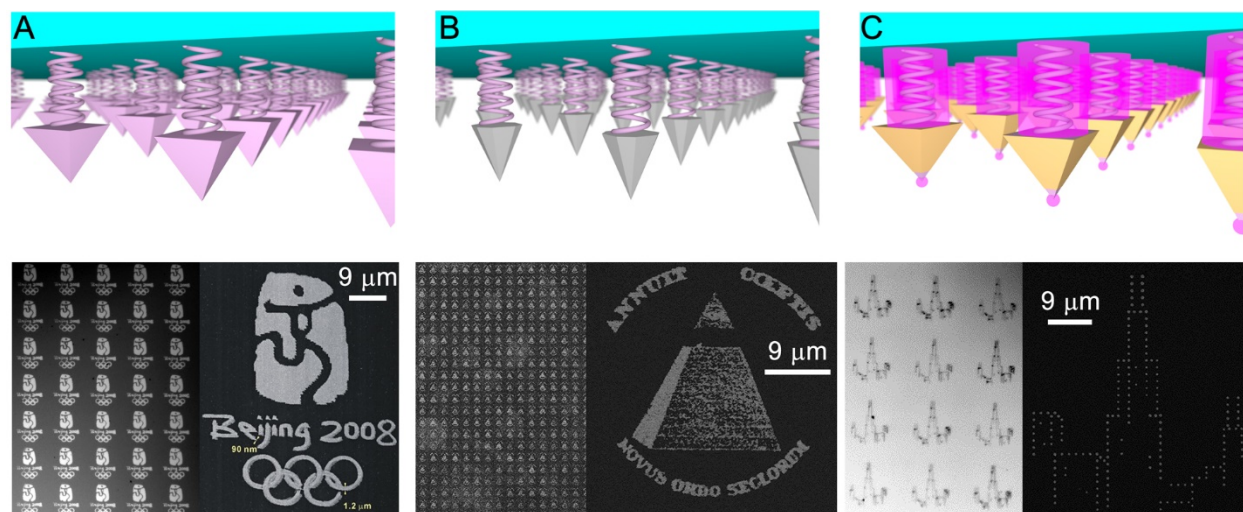
Figure 1.3. CF-SPL pen array architectures. (A) Elastomeric pens are used for polymer pen lithography (PPL).[15] This technique has the advantage that tips can be intentionally deformed to adjust feature size without changing writing speed. From ref (15). Reprinted with permission from AAAS. Copyright 2008 AAAS. (B) Hard silicon pens are used for hard-tip, soft-spring lithography (HSL) which achieves consistently high resolution across centimeter scales.[85] Reprinted with permission from ref (85). Copyright 2011 Springer Nature. (C) Elastomeric pen arrays that are coated with an opaque layer can be used for diffraction-unlimited near-field photolithography provided that sub-wavelength apertures are constructed at the apex of each pen.[86] Reprinted with permission from ref (86). Copyright 2010 Springer Nature.

A key observation in CF-SPL was the realization that by making the pens rigid but retaining the compliant backing layer, one can achieve force-independent patterning. Specifically, in hard-tip soft-spring lithography (HSL), arrays of pyramidal silicon pens on a PDMS backing layer are used to reliably print features as small as 40 nm over centimeters (Figure 1.3B).[87] The mechanical properties of these pens are well understood in that they exhibit linear force-distance relationships and their spring constants can be tuned in the 7 to 200 N/m range, a range consistent with intermediate to high stiffness cantilever-based systems.[88] Interestingly, due to the linear dependence of the spring constant on the geometric properties of the pen array, the spring constant in HSL can in principle be specified with greater precision than is commonly obtained in cantilever-based systems in which the spring constant is dependent on geometric parameters such

as cantilever length and thickness to the third powers.[89] Importantly, more easily synthesized PPL pen arrays can be modified to have the same force-independent patterning capability of HSL – PPL arrays coated with silica using a low temperature plasma enhanced chemical vapor disposition step were found to have the force-independence inherent to HSL, while at the same time, retaining the optical transparency of PPL.[90]

1.6. Patterning with Energy

While many of the enabling capabilities of CF-SPL stem from directly depositing materials, the ability to direct the transfer of energy bears extreme promise for realizing synthetic capabilities for nanocombinatorics. An early example of transferring energy with CF-SPL was the use of HSL to mechanically deform polymeric surfaces.[87] Since this observation, graphene-coated HSL pen arrays have been used to pattern with electrical energy or heat with sub-100 nm resolution.[83]

In general, the most widely used lithographic methods use light to define patterns,[91] and CF-SPL has been extensively explored in this context. The transmission of light through elastomeric pyramidal pens has been studied from the perspective of photolithography[92] and adaptive optics,[93] but the attainable resolution is not better than the far-field diffraction limit when unmodified elastomeric pyramids are used.[94] In contrast, by depositing opaque layers on the pyramidal pen arrays that have sub-wavelength apertures at the tip of each pen, the pen arrays can be used for diffraction-unlimited lithography (Figure 1.3C).[95] This approach, known as beam pen lithography (BPL), has been used to pattern 100 nm scale features over centimeters. In this context, light is an especially useful form of energy for patterning because it can be massively multiplexed with relative ease using technologies such as digital micromirror devices. Such multiplexing

capabilities grant the ability to pattern arbitrary nanoscale features with each pen in a centimeter-wide array.[96] This technology has been utilized as a lithographic tool to define nanoreactors to synthesize oxide nanostructures in high throughput.[97]

Due to the widespread interest in patterning with light, many cantilever-free pen array architectures for optical lithography have been explored. For example, pen arrays coated with metal films featuring apertures at the tips of each pen have been made serially by focused ion beam milling[95] or in parallel using either reactive ion etching or electrochemical processes.[96, 98-100] It has also been shown that pens without apertures (*i.e.* those that feature continuous metal films across the entire pen array) still allow one to pattern, but with lower resolution.[101-103] The degradation in resolution associated with having no apertures is somewhat mitigated if the pens are composed of a high refractive index material.[104] Alternatively, carbon black can be placed in the space between the tip array in the surface,[105] as was originally reported in the context of light valves.[93] Importantly, detailed study of the optics of BPL has shown that an opaque film on the backing film is very important for reducing unwanted illumination in all cases.[94]

A recent advance that has great significance for the prospects of performing nanocombinatorial studies using CF-SPL is the ability synthesize materials using BPL in a fluid environment. This concept was first proved by synthesizing nucleotide nanoarrays in an aqueous environment.[106] Significantly, these first explorations showed that, much like immersion lithography techniques used by integrated circuit manufacturers,[107] operation in a high refractive index environment can increase the resolution of BPL.[106] Furthermore, by encompassing the BPL pen array inside a microfluidic channel with inlet and outlet ports, it is possible to introduce a series of chemical reagents without removing the pen array, thus allowing for the synthesis of

multi-component structures such as multi-color brush polymers.[108] This advance is particularly enabling because it means that BPL could be used to synthesize highly complex biomolecular arrays with higher resolution than is possible using far-field optics.[109] Additionally, BPL is well suited for use with the myriad photochemistries that have been explored to define functional surfaces, of which applications in biology are particularly promising.[110]

1.7. Combining patterning with energy and materials

Ultimately, there are many ways of patterning using energy, but a truly enabling capability afforded by CF-SPL is the ability to simultaneously deliver materials and energy with the same pen array. Indeed, the local delivery of energy can be used to control both feature size and structure composition, and the combination of the two can yield distinct structures. For example, a BPL pen array has been used to directly write polymer features containing carbohydrate precursors.[111] The pen array was subsequently used to illuminate each individual feature for a prescribed amount of time, thereby controlling the degree of carbohydrate polymerization. Thus, two independent variables were controlled: (1) the area of the pattern (dictated by material transfer) and (2) the chain length of the carbohydrate (dictated by illumination).[111] Since then, several other synergistic approaches have been explored, including sequentially printing chemicals and modifying them with light,[94] or modulating the ink itself through photopolymerization or photoisomerization reactions to change patterning dynamics *in situ*.[112] Because of the multiple degrees of freedom, and the ease of multiplexing the delivery of light, these approaches exhibit considerable promise for realizing multicomponent libraries for nanocombinatorics.

1.8. Nanocombinatorial studies with CF-SPL

Based on these synthetic capabilities, reports of nanocombinatoric experiments performed using CF-SPL have begun to emerge. The first example was a study of the differentiation of mesenchymal stem cells as a response to their local extracellular environment. Specifically, by utilizing a tilted-PPL patterning experiment to generate a gradient of features composed of extracellular matrix (ECM) proteins, it was possible to ascertain the ECM protein density that allowed cells to adhere and differentiate down osteogenic pathways (Figure 1.4A).[7] Cell biology experiments such as this are an ideal use of CF-SPL due to the connection between the length scales of the experiments: cells tens of microns in size are commensurate with typical pen-to-pen pitches while the focal adhesions are tens to hundreds of nanometers, which is the scale of individual features written by CF-SPL.[7] It was also recently shown that multi-component patterns composed of up to three independently patterned biomolecules can be used to interact with cells, as was shown in experiments exploring the interactions between MCF7 cells and combinatorial sets of patterns of proteins.[75] Interestingly, multicomponent patterning was achieved in this case by using different oligonucleotide strands that were subsequently used to orthogonally immobilize different peptides.[75] Such complex multicomponent patterns of biomolecules can also be used to capture rare circulating tumor cells.[113] In another promising example of combinatorial studies of cell-surface interactions enabled by CF-SPL, arrays of allergens were patterned using PPL and used to study the activation of mast cells (Figure 1.4B).[114] Finally, by combining PPL with self-assembled monolayer laser desorption-ionization (TCAL-SAMDI) mass spectrometry, it is possible to quantify the enzymatic activity of individual cells in massively parallel arrays, in a post-cell lysing format.[115]
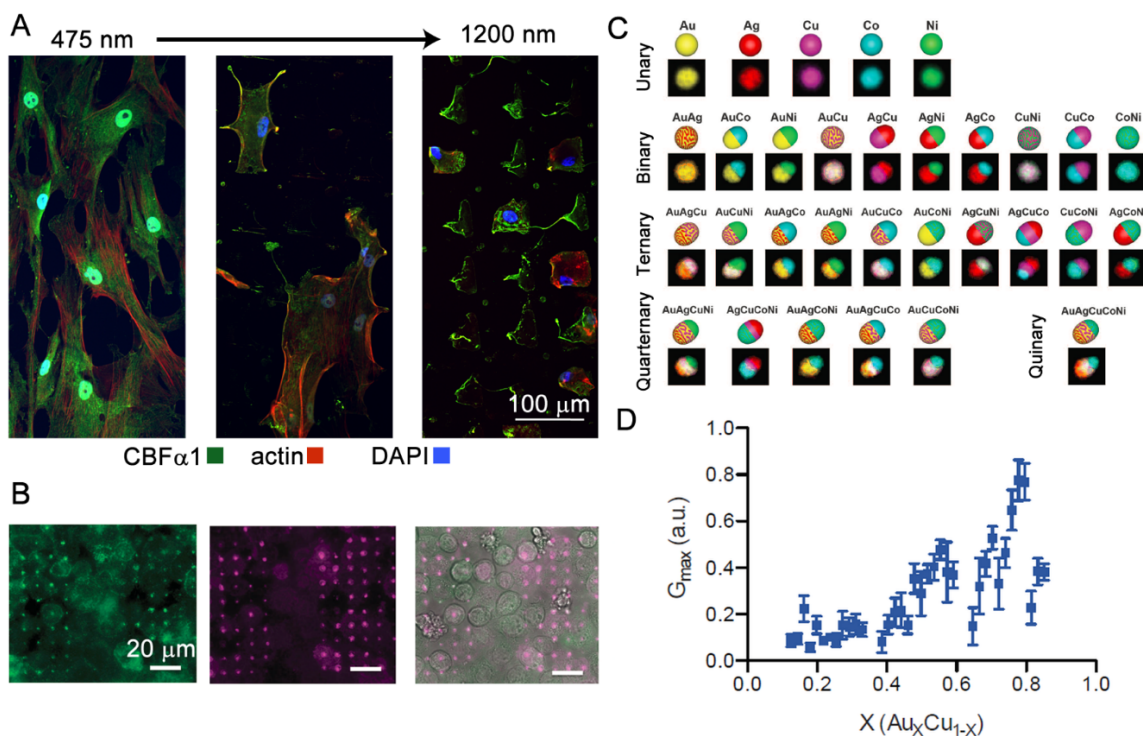
Figure 1.4. Nanocombinatorial studies using CF-SPL. (A) Tilted polymer pen array experiments were used to pattern a surface with a gradient of fibronectin features between 475 and 1200 nm in size. The behavior of mesenchymal stem cells was observed to be dramatically different using epifluorescence microscopy.[116] Reprinted with permission from ref (116). Copyright 2012 National Academy of Sciences. (B) Patterned allergens were used to study the activation of mast cells. The green activation signal (left) and purple colocalization signal (middle) are merged with a bright field image (right).[117] From ref (117). Copyright 2016 Wiley-VCH Verlag GmbH & Co. KGaA, Weinheim. Reproduced by permission of John Wiley & Sons, Inc. (C) Up to five-component nanoparticles synthesized using a combination of CF-SPL and scanning probe block copolymer lithography (SPBCL).[118] From ref (118). Reprinted with permission from AAAS. Copyright 2016 AAAS. (D) First example of combinatorial screening with a single CF-SPL patterned array to discover an optimal catalysis for the synthesis of nanomaterials.[69] Reprinted with permission from ref (69). Copyright 2018 National Academy of Sciences.

A second major example of nanocombinatoric studies relying on CF-SPL is the study of nanoparticle-based heterogeneous catalysis. Together with SPBCL, CF-SPL represents a way of reliably patterning single nanoparticle features with controllable sizes and compositions in desired locations. Indeed, it was recently shown that in addition to two-component alloys,[119] as many as five-component alloys can be robustly synthesized with predictable composition and structure

(Figure 1.4C).[120] Since synthesizing these structures is difficult through other means, this methodology allows one to synthesize and study particles from a vast size and compositional parameter space to identify structures that are worth investigating at a larger scale. As the first example of this, the catalytic reduction of 4-nitrophenol using CF-SPL patterned nanoparticles revealed that AuPd alloy nanoparticles have enhanced catalytic activity compared to their monometallic counter parts.[119] In the field of electrochemistry, the combination of CF-SPL based experiment and computational predictions prompted the discovery of AuCuPt nanoparticles as high performing catalysts for the hydrogen evolution reaction.[121] Recently, CF-SPL was used to generate combinatorial megalibraries that were compatible with high-throughput automated experimentation[122] to allow nanoparticles chosen from the AuCu parameter space to be rapidly screened for the growth of single walled carbon nanotubes.[69] Importantly, these experiments led to the discovery of Au_3Cu_1 as a previously unidentified optimal composition (Figure 1.4D). These examples have set the stage for CF-SPL to provide a rapid means of determining the structure-property relationships that govern nanoparticle heterogeneous catalysts in a nanocombinatorial setting.

These two nanocombinatorial studies serve as examples that CF-SPL can be used to realize arrays of nanoscale structures with sufficient variety and complexity to enable diverse experiments and that there is knowledge to be gained by performing these types of experiments in diverse fields ranging from biology to catalysis. In the coming years, it is expected that many more examples will come to light. This trend will become increasingly apparent as advanced materials and devices are realized through non-traditional patterning approaches. For instance, electron beam lithography was used to pattern DNA molecules which templated the assembly of optical

metasurfaces.[123] CF-SPL is ideally suited for these type of patterning tasks where soft or bioactive materials are patterned with spatial control over their composition.

1.9. Conclusions and Outlook of Nanocombinatorics and CF-SPL

Collectively, the studies described above represent not only the power of CF-SPL as an enabling synthetic tool for nanocombinatoric studies, but also the potential of CF-SPL as a discovery tool. However, synthesis is only half of the nanocombinatoric challenge – screening the product rapidly becomes a rate-limiting step as the scale of the experiments continues to increase. Given the success of CF-SPL for nanocombinatorial synthesis with millions of discrete features, the need in nanocombinatorics shifts from improving CF-SPL resolution and throughput to the development of methods that can analyze these patterned systems at a rate comparable to their production. With the development of this versatile platform, it is possible to expand the materials genome by utilizing the nanoscale in a way that was not previously possible before now.

In closing, CF-SPL brings capabilities to the table in terms of throughput, materials versatility, and pattern complexity, all in a low cost – and therefore widely adoptable – format. The ability to positionally encode nanoscale domains of soft and hard materials across centimeters has ramifications that spans chemistry, biotechnology, and materials science; thus, CF-SPL may be regarded as an "experimental sandbox" that enables diverse experiments.

2. Chapter Two

Hard Transparent Arrays for Polymer Pen Lithography
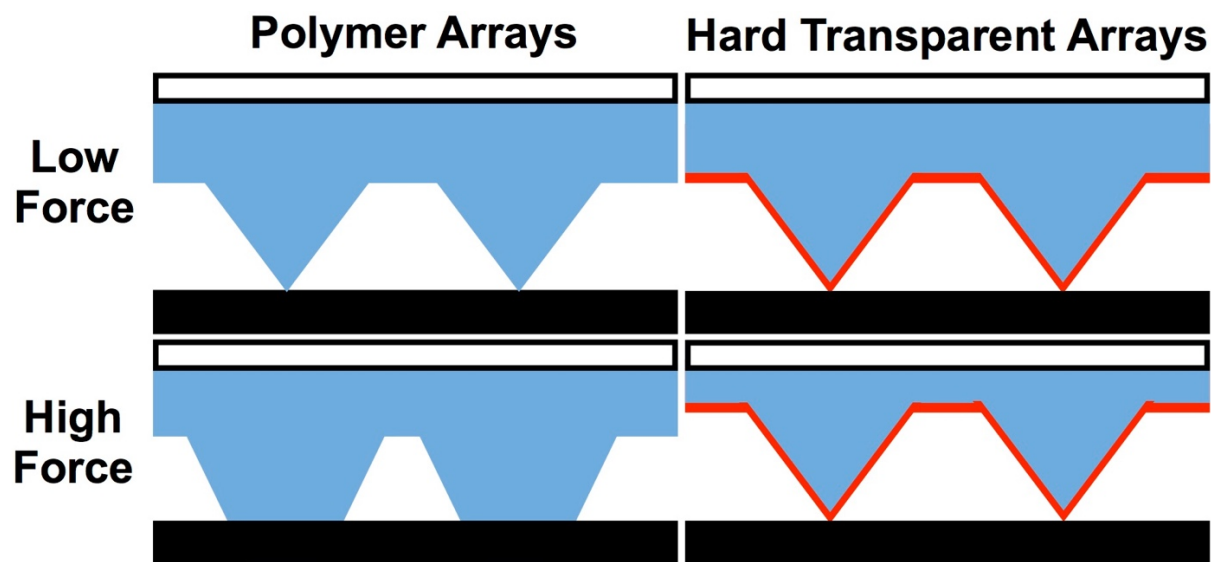
Reprinted with permission from Hedrick, J. L.; Brown, K. A.; Kluender, E. J.; Cabezas, M. D.; Chen, P.-C.; Mirkin, C. A. Hard Transparent Arrays for Polymer Pen Lithography. *ACS Nano* 2016, *10*, 3144-3148. Copyright 2016 American Chemical Society.

2.1. Increasing Density with Hard Transparent Arrays for Polymer Pen Lithograph

One limitation of previous studies of catalysts with PPL was poor signal from having a low catalytic density of nanostructures synthesized using a polymeric pen array. In PPL, each pen deposits ink when it comes into contact with a surface. The pens deform in a force dependent manner that can be conceptually separated into (1) a tip deformation that increases the tip-sample contact area and (2) a deformation of the support that does not change the tip-sample contact area. While the force dependent increase of contact-area upon deformation is useful as a means to vary feature size,[79, 124, 125] it limits the minimum achievable size and sensitizes patterning to variations in pen array height.[126] As a result, the minimum feature size achieved by PPL is larger than the smallest written by its cantilever-based predecessor dip-pen nanolithography (DPN), which features non-deformable pyramids in contact with the surface, by a factor of ~3.[126-133] The dependence of feature size on tip-sample force further limits pattern uniformity because of: (1) uncertainty in knowing the tip-sample height and (2) variation of tip height across the array. While both of these factors are reported to be under ~250 nm, there is nearly a 1:1 relationship between extension and feature size, so this effect can be quite significant when considering the desire to write large scale arrays of sub-micron features.[126, 134, 135]

Significantly, if the elastomeric pens are replaced with rigid silicon pens (while retaining the elastomeric backing film), force-independent patterning is possible.[136, 137] This technique, known as hard-tip, soft-spring lithography (HSL), offers an 8 μm range in extension over which the feature size does not change. The drawback to HSL is that making each pen array consumes a 50 μm thick Si wafer, in contrast to PPL which utilizes pen arrays that can be casted nearly

indefinitely from a single Si mold. Additionally, HSL pens are not transparent, which precludes their use for patterning with energy *via* optical methods.[46, 138] Other attempts to improve resolution of PPL have relied on using pen arrays composed of other polymers or hard polymer pens on a soft elastomer support.[139-141] These approaches reduce the feature size dependence on force by at most ~1/4, but none have produced extension-independent patterning. In order to have effective combinatorial synthesis, evaluation of small features with consistent and predictable sizing at a high density is necessary. To improve PPL for this application, a new cantilever-free pen array architecture is presented that affords the ability to write with high resolution in an extension-independent manner using transparent pen arrays that are simple modifications of inexpensive PPL pen arrays.
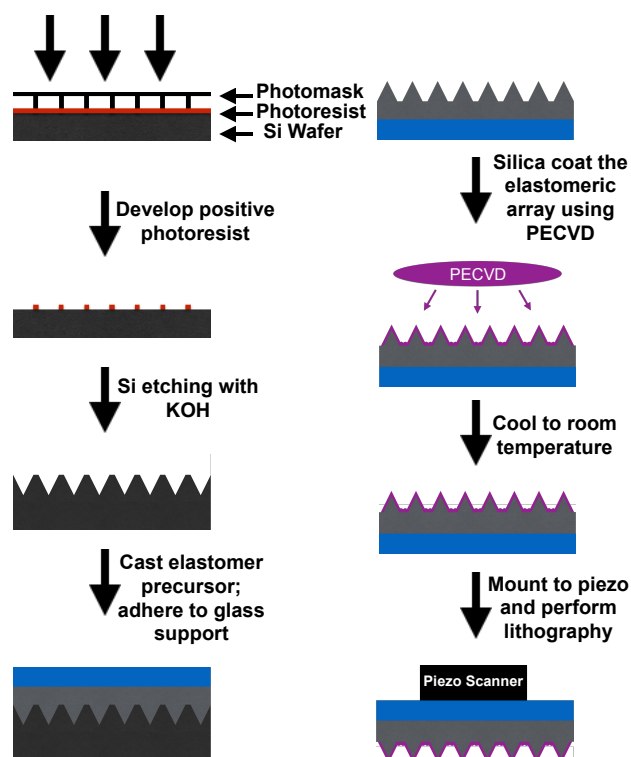
Scheme 2.1. Fabrication process for hard transparent polymer pen arrays.

The central hypothesis of this work is that by coating PPL pen arrays with a thin hard layer, the tip of each pyramid will retain its shape during patterning because strain due to tip-sample contact will be absorbed by the elastomeric layer (Scheme 2.1). Specifically, coating PPL pen arrays composed of polydimethylsiloxane (PDMS) with silica using plasma-enhanced chemical vapor deposition (PECVD) was found as an effective way to construct pen arrays capable of patterning small molecules and polymers at high resolution without dependence on tip-sample contact force.

In principle, the presence of a conformal hard layer could enable pen arrays to write in a consistently high resolution and extension-independent manner. However, depositing a hard material on a soft material is challenging and often results in buckling[142-144] and delamination.[145] To address this problem, a low temperature PECVD process was developed to minimize the degree of thermal expansion that would lead to residual strain between the hard layer and the elastomeric pen array. Specifically, this deposition process was carried out at 200 ºC using 900 mTorr with 500 sccm SH_4, 1420 sccm O_2, and 30 W of high frequency power. By performing spectroscopic ellipsometry of films grown on Si wafers, a growth rate of 0.92 ± 0.01 nm/s was extracted with a refractive index of 1.49 ± 0.01 at a wavelength of 630 nm, as expected for silica. While silica films grown on PDMS films could not be measured using ellipsometry due to the buckling pattern that emerged, this periodic buckling pattern itself was used to compute the film thickness (Figure 2.1A and 2.1C).[146] By assuming that the modulus of the silica film is the same as bulk silica, the rate of deposition of silica on the PDMS surface was calculated to be 0.55 ± 0.03 nm/s (Figure 2.1B).
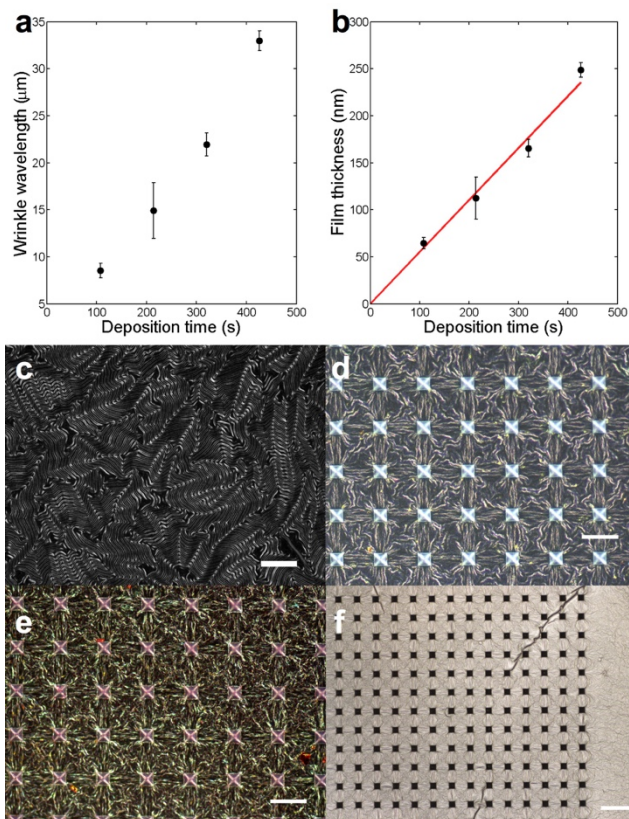
Figure 2.1. (a) Wrinkle wavelength as a function of silica thickness. (b) Silica thickness as a function of deposition time (slope 0.55 ± 0.03 nm/s). (c) Bright-field image of silica deposited onto a slab of PDMS, 200 µm scale bar. (d) Dark-field image of hard transparent array when it is at the goldilocks thickness of 175 nm, 50 µm scale bar. (e) Dark-field image of shattered hard transparent array tips after patterning rhodamine 6G when silica thickness is too thin at 83 nm, 50 µm scale bar. (f) Bright-field image of hard transparent array when silica thickness is too large, here 250 nm, buckling goes through the tips, 100 µm scale bar.

In order to determine the optimal thickness of silica that would allow for force- independent patterning, five PPL pen arrays were coated with silica films of different thicknesses and subsequently evaluated for their morphology and behavior during tip-sample contact. When the thicknesses were small (< 100 nm), the force on the pens during contact caused the thin silica layer to delaminate from the tip (Figure 2.1E). In contrast, when the thickness was large (> 250 nm), the buckling effect was so great that it substantially deformed the pens and perturbed the uniformity

of the pen array (Figure 2.1F). Pen arrays with ~175 nm thick silica films were found to be optimal compromises that mitigated these effects (Figure 2.1D). While CVD-grown silica was found to be robust for patterning, it has been previously noted that exposing a PDMS film to an O_2 plasma forms a silica film on the surface of the PDMS.[147] This observation could explain the change in writing performance of PPL pen arrays following repeated exposure to O_2 plasma, however this approach to deposit silica layers is impractically slow for generating robust hard layers.
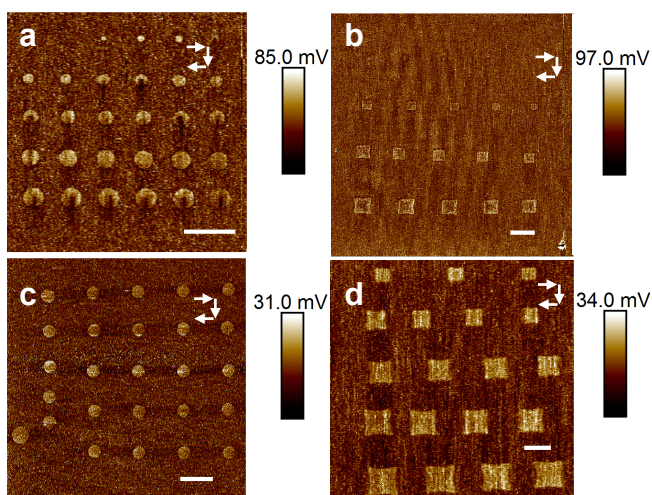
Figure 2.2. Patterning MHA using (a) a hard transparent array and (b) a polymer array, both with an extension sweep covering 5 μm piezo range with 1.5 μm/s extension and withdraw speed and no dwell time at full extension. Patterning MHA using (c) a hard transparent array and (d) a polymer array, both with an extension sweep over 5 μm piezo range with 100 μm/s extension and withdraw speed and 5 second dwell time. All scale bars are 2.5 μm. Images were taken using lateral force microscopy using AFM.

In order to explore the force-dependent feature size of polymer arrays versus hard transparent arrays, 16-mercaptohexadecanoic acid (MHA) features were patterned onto gold whereby each pen wrote 25 individual dots in an array that varied in extension across the pattern with a constant dwell time. MHA was chosen because it is well known to form monolayers on gold and has been patterned extensively by PPL and DPN.[130] Features written by polymer arrays were observed using atomic force microscopy (AFM) to be square with edge lengths that depended

on extension. The square morphology originates from the deformation of the tips during patterning. In contrast, the features written by hard transparent arrays were found to be independent of tip-sample force over a 5 μm extension range (Figure 2.2B and 2.2C). PPL performed with hard transparent arrays is more reminiscent of conventional DPN, which generates circular features with dwell time-dependent diameters (diffusion-mediated).[125]

While force-independent patterning will allow for more consistent patterns, intentionally varying pen deformation allows one to pattern macroscopic gradients by tilting the pen array with respect to the patterning surface, which enable nanocombinatoric patterns of a gradient of features.[124, 125, 148-150] In order to regain this ability in these hard transparent arrays, it was hypothesized that tilting the array and approaching the surface slowly would result in a positionally-dependent tip-sample contact time, giving a gradient of feature sizes as a result of an increase in diffusion time between the tip and substrate. To test this hypothesis, a patterning experiment was performed in which extension was increased over a 5 μm range with a 1.5 μm/s approach and retraction speed. At most, this would result in a ~3 s difference in tip-sample contact time for every micron difference in extension. Indeed, after patterning, MHA features ranging from 250 nm to 1 μm in a smooth size gradient were observed (Figure 2.2A and 2.2B). This is an important capability as it allows one to contemplate constructing nanocombinatoric arrays for experiments with PPL arrays coated with silica by making gradients of feature sizes.[124, 151]

As polymers comprise an important class of inks, it is important to verify that hard transparent arrays can pattern polymer inks effectively. In order to test this capability, polymer arrays and hard transparent arrays were used to pattern a square dot array with an extension that varied over 5 μm after being inked with a 5 mg/mL solution of the block copolymer poly(ethylene

oxide)-*b*-poly(2-vinyl pyridine) (PEO-*b*-P2VP, Mn=2.8-*b*-1.5 kg·mol^{-1}) in water. In this experiment, the approach speed was 100 μm/s, which indicates that varying tip extension over a 5 μm range had a negligible effect on the fixed 2.5 s tip-sample contact time.

Following patterning, AFM imaging revealed that features written by conventional polymer arrays exhibited a large square contact area while those written by hard transparent arrays had small round contact areas that were independent of extension (Figure 2.3A and 2.3C). Furthermore, as with patterning alkanethiols on gold, it was possible to vary the feature size of polymers by changing approach speed. Specifically, the tip extension was varied by 4.2 μm while writing a dot array with an approach speed of 3 μm/s, resulting in gradients of feature sizes from 40 to 160 nm (Figure 2.3B and 2.3C).
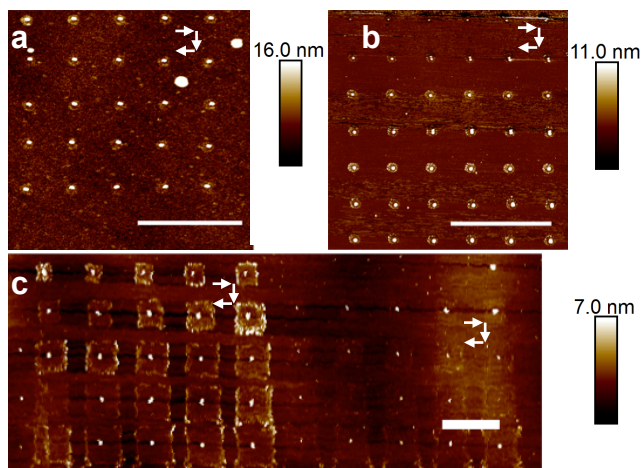
Figure 2.3. Patterning polymer ink with an (a) extension sweep over 5 μm piezo range with 100 μm/s extension and withdraw speed using hard transparent arrays and a dwell time of 2.5 s at full extension, (b) hard transparent arrays extension sweep over 4.2 μm piezo range with 3 μm extension and withdraw with no dwell time at full extension, and (c) PPL extension sweep over 5 μm piezo range with the left half corresponding to the conditions in (a) and the right half corresponding to (b). Scale bars are 2.5 μm. Images were taken with AFM in taping mode.

As previously discussed, effective screen of catalysts requires higher density patterns and a problem associated with tip deformation is that it can limit feature pitch. While small molecules

that covalently bind to the patterning surface are robust after patterning, large molecules that physically adsorb to a surface, such as polyethylene glycol, can be disturbed after patterning because they behave as fluids in the high humidity environment needed for patterning.[152, 153] Because of this phenomenon, if the tip-sample contact diameter is on the order of the feature pitch, the tip will perturb neighboring features when patterning. With polymer arrays, this manifests as a row of features merging into a single large feature. In principle, this would be mitigated with hard transparent arrays because of the lack of tip deformation. Specifically, by patterning PEO-*b*-P2VP, hard transparent arrays yielded feature pitches of 175 nm with a hexagonal array (Figure 2.4A and 2.4B). By switching from a square pattern array to hexagonal pattern array, the feature density was even further increased by ~15%. The capability of patterning smaller pitches indicates that it is possible to pattern extraordinary numbers of features. Specifically, by patterning 14,641 polymer dots with each of the four hundred thousand pens in a 14.5 cm^2 array, it was possible to generate a total of 5.9 billion polymer dot features (Figure 2.4C and 2.4D).

Cantilever-free scanning probe lithography is poised to become an important tool for rapidly performing nanocombinatoric experiments.[124, 149-151] In this work, it is shown that the use of hard transparent arrays allows one to write higher density and more reliable patterns than is possible using polymer pen arrays. While this silica coating was found to render patterning of polymers and small molecules to be force-independent, it also enables a method of writing gradients with force-independent probes. Importantly, hard transparent arrays are a simple post-modification of polymer pen arrays, indicating that the barrier to adoption is extremely small. When combined with a technique like scanning probe block copolymer lithography (SPBCL),[154-156] which utilizes PEO-*b*-P2VP and a metallic precursor to direct the on-surface and spatially

confined synthesis of metal nanoparticles, one can create high-density nanoparticle arrays with potentially important implications in areas such as plasmonics, nanomagnetics, and catalysis.[157, 158] Ultimately, the ability to directly write billions of discrete features on a surface is a significant advance for nanolithography and could open avenues for using cantilever-free scanning probe lithography as a combinatorial discovery tool, especially when combined with a technique to combinatorially ink an array.

3. Chapter Three

Synthesis of Nanocombinatorial Megalibraries
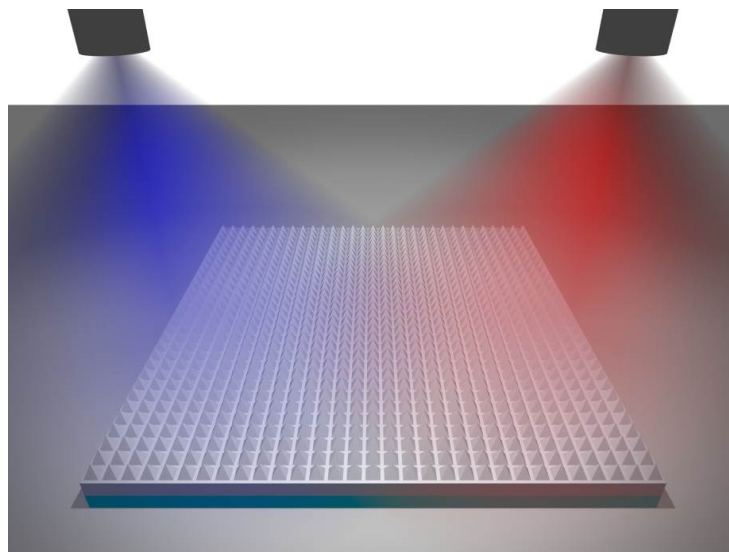
Reprinted with permission from Kluender, E. J.; Hedrick, J. L.; Brown, K. A.; Rao, R.; Meckes, B.; Du, J.; Moreau, L.; Maruyama, B.; Mirkin, C. A., Catalyst Discovery through Megalibraries of Nanomaterials. *Proc. Natl. Acad. Sci. USA* **2019, 13 (1), 8-17. doi: 10.1073/pnas.1815358116. Copyright 2019 National Academy of Sciences.**

3.1. Combinatorial Synthesis

High throughput screening is an invaluable tool for scientific discovery in many fields.[159-161] As a key technology for discovery, high throughput approaches enable the ability to synthesize combinatorial libraries of compounds and simultaneously probe numerous reaction conditions that allow for the study of a variety of samples in unison. As such, combinatorial libraries have been utilized in diverse fields including: catalysis, drug discovery, and basic cell biology.[162-164] Such massively parallel experiments are typically performed using advanced liquid handling systems that deposit nanoliter scale fluid volumes into plates with as many as 1536 distinct wells.[165] However, the path to utilizing smaller volumes with higher throughput faces major challenges as techniques for depositing controlled quantities of chemically specific materials are limited. Ink jet printing, both through electrohydrodynamic jetting and ultrasonic focusing, can in some cases generate sub femtoliter-scale volumes, but is limited in throughput by serial printing afforded by a single nozzle and low registration accuracy resulting from the dewetting process. Similarly, the direct write of materials from a physical scanning probe, such as dip-pen nanolithography, can reliably pattern sub-attoliter volumes, but throughput is a critical limitation. PPL and related technologies, including SPBCL, deposit attoliter quantities of ink onto the surface, but have been been limited to a single ink type for each experiment. Chemical heterogeneity has proven more difficult to systematically introduce as the only methods that have been explored for inking tips are microcontact printing of blocks of tips or individually inking them using ink jet printing. While these present an advantage in terms of scaling, one ink jet printing operation is needed to ink each

individual pen with ~50 micron pitch, which will subsequently be used to pattern thousands of features with a sub-micron pitch. It is still not practical to scale to millions of pens. Indeed, for many types of experiments, independent control over every pen in the array is unnecessary because a linear continuum of ink composition is desirable. From this perspective, advances in how to rapidly ink polymer pen arrays with non-uniform ink composition would bear important implications for the synthesis of combinatorial arrays for rapid materials discovery.

Here, I describe a method for inking PPL pen arrays with a linear gradient of ink composition using a dual-spray coating procedure. While inking PPL pen arrays may be a new task, the process of coating materials with uniform thin films is a widely used industrial process encompassing methods that include spin coating, dip coating, and spray coating. The advantages and drawbacks of these techniques are well known; spin coating is compatible with high viscosity inks but is limited to relatively small surfaces. Spray coating requires relatively low viscosity solutions, but is extremely scalable.[150, 166] However, both of these methods are typically optimized to generate uniform films. Here, we study the radial distribution of spray-coated ink and explore the possibility of using multiple spray coating nozzles with overlapping distribution areas as a method for inking pen arrays with a compositional gradient. Importantly, by combining a compositional gradient in one dimension with a size distribution in the other, we synthesize centimeter-scale surfaces coated with a combinatorial array of sub micrometer soft materials.
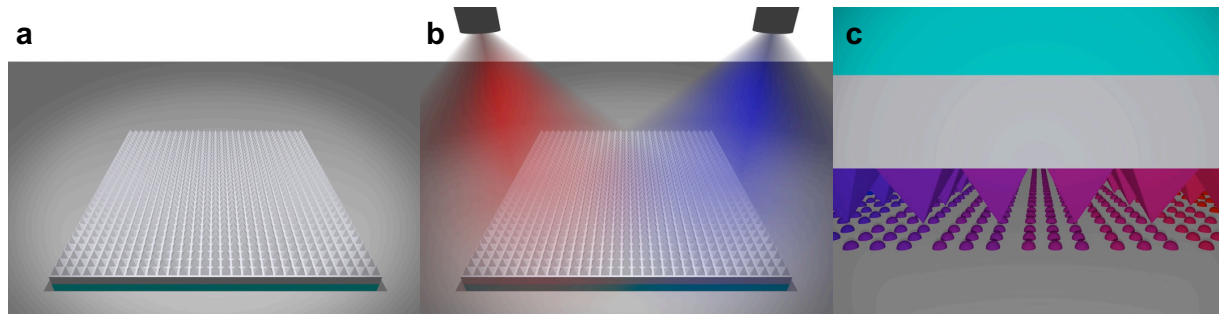
Scheme 3.1. (A) PPL array before inking, (B) dual spray coating of two different inks onto the PPL array to make composition gradients, and (C) patterning combinatorial libraries of nanomaterials by mounting the PPL array to a piezo scanner.

In order to explore spray-coating as a method for depositing linear gradients onto surfaces, the radial distribution of the gradient was evaluated by performing a spray-coating operation on a target substrate and mapping its distribution to a gaussian plot (Figure 3.1D). In particular, a commercially available Harder Steenbeck Infinity CR plus airbrush was loaded with aqueous ink composed of 10 mg/ml rhodamine 6G and 5 mg/ml poly(2-vinyl pyridine -b- ethylene oxide) (P2VP-b-PEO) and sprayed with a air flow pressure of 20 psi onto a piece of blank printer paper being held at distances of 5, 10, 15, and 20 cm from the surface. The choice of a colored ink enables the evaluation of the spray scatter from a scanned grayscale image (Figure 3.1B).
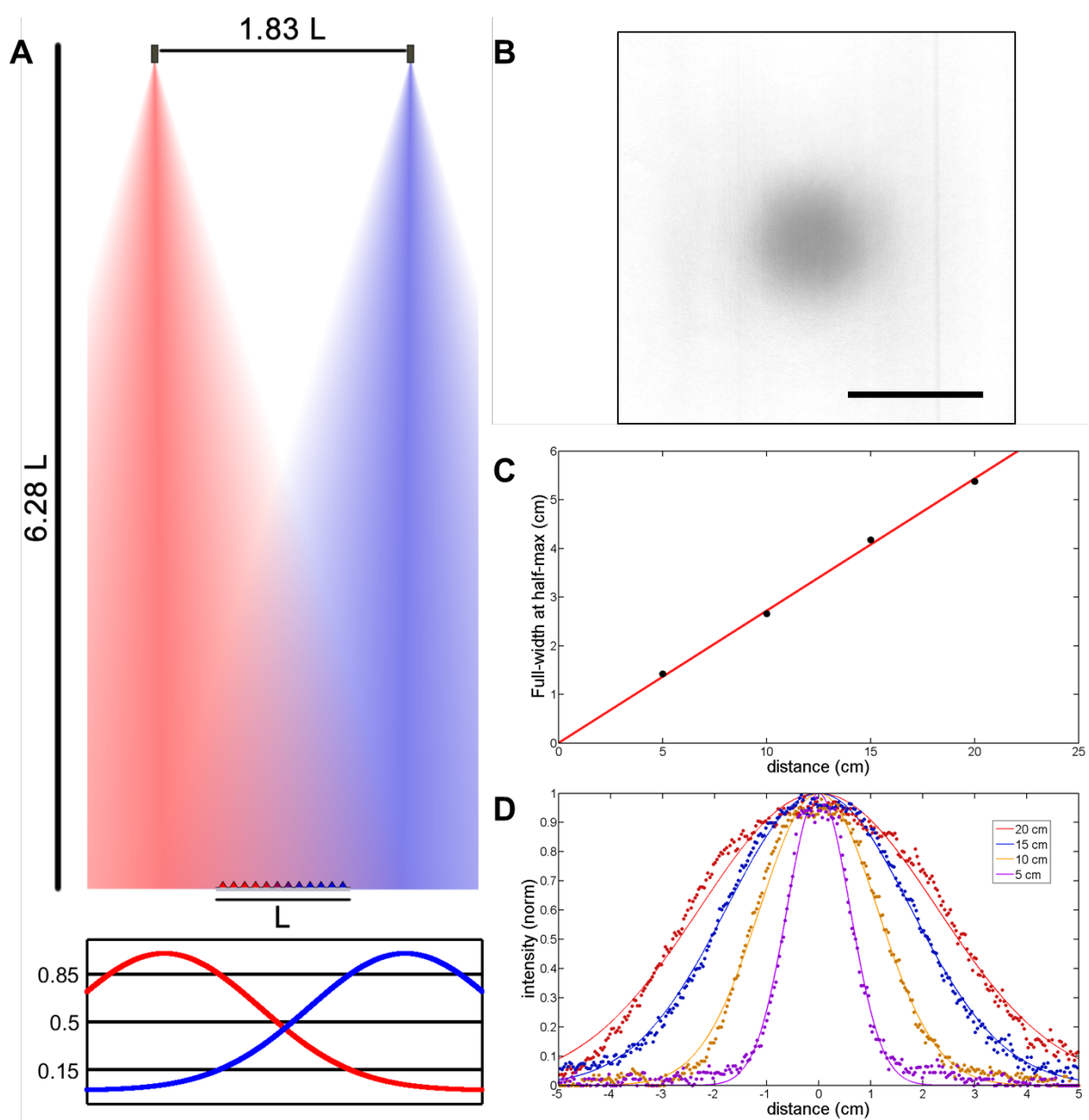
Figure 3.1. (A) Diagram of how to position spray guns to PPL array based on size, (B) scanned spray used to quantify intensity, scale bar 5 cm (C) linear full width half max slope showing a linear scaling trend for PPL arrays, (D) equation fitting of spray intensity data at different distances.

Quantitative evaluation of this distribution was done by examining the intensity of the image in a line across the center of the image, which shows a linear full width half max (FWHM) of radial spray distribution 0.2717 (Figure 3.1C). Utilizing this trend, it is possible to tailor the

airbrush separation from the second airbrush as well as the PPL array based on the dimensions of the array being inked with simple linear relationship (Figure 3.1A). In this work, a 1.5 cm by 1.5 cm PPL array was used. Utilizing the relationship between FWHM and separation distance, the dimension of this PPL array requires separation of 5 cm between spray guns and 20 cm from the target.

While spray-coating a uniform film on a flat surface is well understood problem, forming a compositional gradient on a surface decorated with a periodic array of pyramidal tips could introduce problems stemming from inhomogeneous drying and diffusion of the constituent materials. Considering a small molecule with a diffusion constant $D \sim 3.5*10^{-6}$ cm^2/s, one may compute the time over which molecules of interest will diffuse between pens and across the whole array.[167] In particular, for 1.5 cm width pen array with a pen to pen pitch of 120 μm, the molecule will diffuse between pens in ~20 s and across the whole array in ~400 days, predicting an extremely long window over which drying can occur and still maintain the compositional gradient. Importantly, we hypothesize that allowing for enough time for diffusion to occur around a specific pen may be very important as it could allow for localized diffusive mixing of the multicomponent ink sprayed near a given pen (Figure 3.1A). In order to test this, two aqueous inks were synthesized consisting of 5 mg/ml P2VP-b-PEO and 10 mg/ml of a fluorophore (quantum dots). The peak emission wavelengths of the two fluorphores were different (*i.e.* one at 490 nm and the other at 575 nm), such that under a fluorescence microscope the inks would be distinguishable without fluorescent overlap. A typical inking procedure consisted of simultaneously spraying the two inks, each aimed at different edges of the PPL pen array. The solutions were then allowed to completely dry and the process was repeated once to ensure uniformity of the gradient across the array. Once

the array was completely dried, optical microscopy was used to characterize the ink distribution in the vicinity of the pens. Specifically, by observing a pen in the center of the array, such that it was exposed to both inks being sprayed, dark field (Figure 3.2B) and fluorescence (Figure 3.2C) microscopy revealed a uniform ring of ink around a pen, suggesting both uniform mixing and that capillary effects during drying result in the ink being localized around the pen.[168-170]
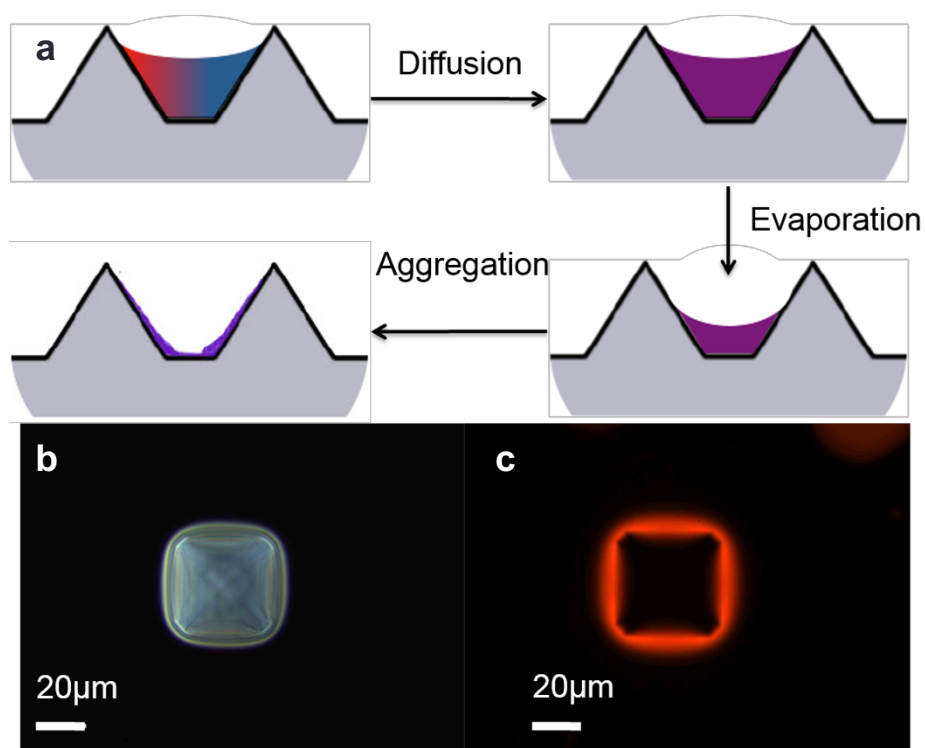
Figure 3.2. (A) Proposed mechanism of ink evaporation following spray coating in which evaporation and diffusion leads to homogenous mixing of the inks and preferential deposition of the ink on the pens. Optical image of a single pen under (B) dark field and (C) fluorescence showing preferential inking at the base of the pen.
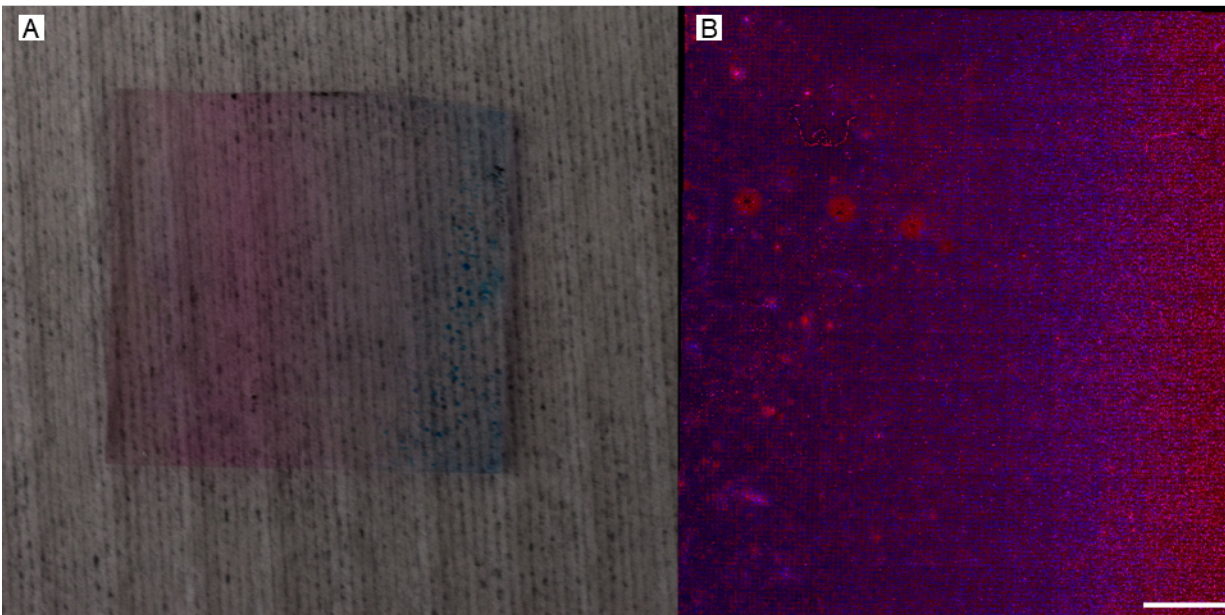
Figure 3.3. PPL array spray-coated with a composition gradient. (A) Photograph and (B) confocal micrograph of the composition gradient spray coated onto the PPL array.

In order to test the hypothesis that local mixing can equilibrate the ink concentration in the vicinity of individual pens but not across the array and can be subsequently transferred to the substrate, two aqueous inks were synthesized consisting of 5 mg/mL P2VP-*b*-PEO and 10 mg/mL of a fluorophore. The peak emission wavelengths of the two fluorophores were different (*i.e.* one, Rhodamine 6G, at λ_{ex} = 528 nm; λ_{em} = 551 nm and the other, Sulfo-Cyanine5 NHS ester at λ_{ex} = 640 nm; λ_{em} = 670 nm), such that the inks would be spectrally distinguishable using a fluorescence microscope. A typical inking procedure consisted of simultaneously spraying the two inks, each aimed at the center of opposing edges of the PPL pen array. The solutions were then allowed to completely dry, and the process was repeated to ensure uniformity of the gradient across the array. To characterize the gradient, the whole PPL array was imaged utilizing a confocal microscope. In order to maintain high resolution to visualize the nanoscale features across the whole array, thousands of images where taken on two tracks, one for each fluorophore, and subsequently stitched and stacked to make a single image with 268 million

pixels (Figure 3.3B). The counter propagating changes in fluorescence contrast indicate that the spray-coating was indeed localized to either side of the array as a clear contrast change was observed when scanning from one side of the array to the other. In order to quantify the distribution of the ink, the image stacks were averaged to construct a profile plot of fluorescence intensity (Figure 3.3B). The dual gradient could be seen by eye as seen by the camera image in Figure 3.3A.

In order to verify that spray-coated PPL pen arrays can be used to pattern surfaces with the same compositional gradient, a dual spray-coated PPL array was used to print polymer dots onto a substrate (Figure 3.4D). Prior to patterning, the pen array and patterning instrument were incubated post-leveling in a chamber held at 90% relative humidity (RH) for 30 min to ensure that the ink was hydrated. Subsequently, PPL was performed with each pen in the array being used to print a 30 × 30 array of dot features (~800 nm) on a silicon wafer that had been vapor coated with hexamethyldisilazane to render the surface hydrophobic (Figure 3.4C). Given that this 126 × 126 pen array contained 15,876 pens, the final pattern was composed of over 14 million discrete polymer features (Figure 3.4A). To characterize this massive array of features, large-scale fluorescence images were acquired, which clearly showed a macroscopic gradient in fluorescence across the patterned surface (Figure 3.4A). Indeed, the average fluorescence intensity is well described by a linear gradient across the entire patterned surface (Figure 3.4B).
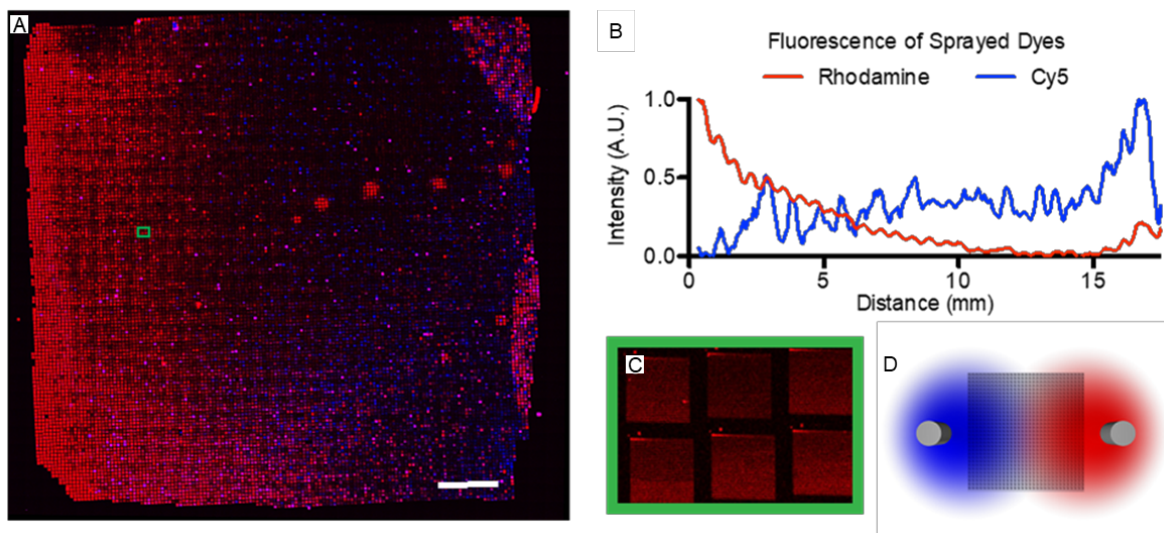
Figure 3.4. Large scale gradients of patterned nanomaterials. (A) Stitched confocal fluorescence image of a compositional gradient of two different fluorophores in patterned polymeric domes, scale bar is 2 mm, and (B) fluorescence intensity across of each region. (C) A magnified fluorescence image showing a single tile from (A), illustrating the dot arrays pattern, as well as the resolution of (A). (D) Schematic of the airbrush position during spraying.

To demonstrate the reproducibility of this system, we used new spray guns that are the same model and make. Then we spray-coated ink with two aqueous inks, both with 5 mg/ml P2VP-b-PEO and one also having 10 mg/ml fluorescein to offer fluorescent contrast. Prior to patterning, the pen array and patterning instrument was held at 90% relative humidity (RH) for 30 min to ensure that the ink was hydrated. Subsequently, the array was used to print a 30 × 30 array of dot features on a silicon wafer that had been vapor coated with hexamethyldisilazane to render it hydrophobic (Figure 3.5C). To characterize this massive array of features, large-scale fluorescence images were acquired, which clearly show a macroscopic gradient in fluorescence across the patterned surface (Figure 3.5A). Indeed, the average fluorescence intensity is well described by a linear gradient across the entire patterned surface (Figure 3.5B).
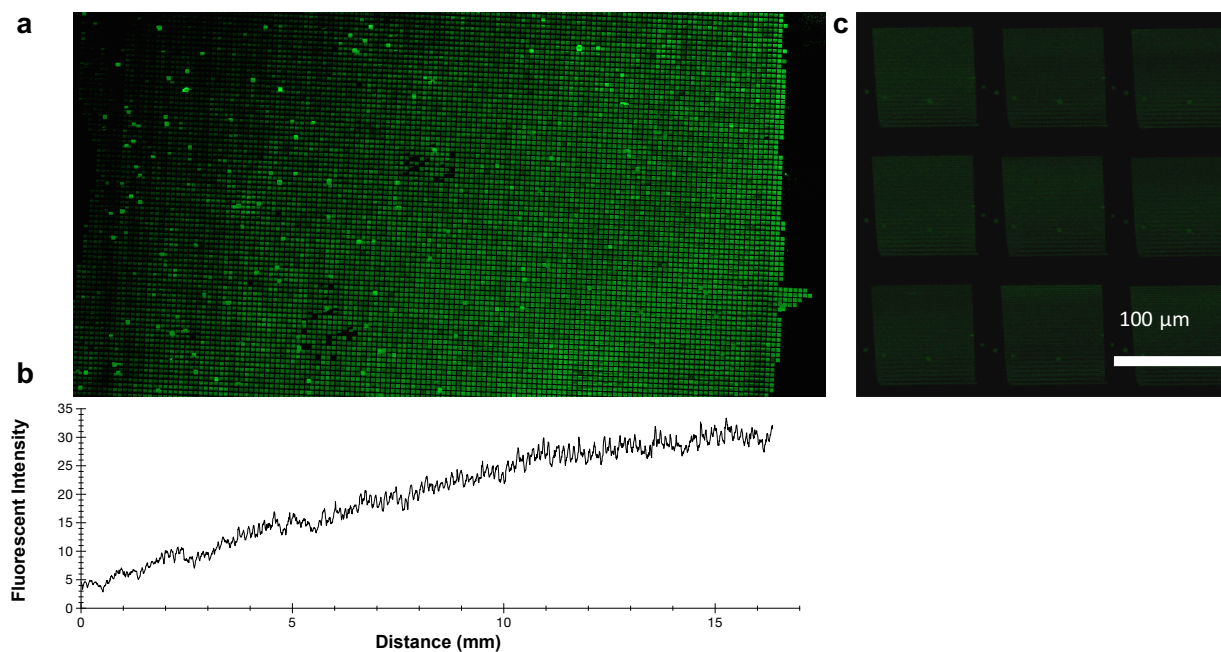
Figure 3.5. (a) Stitched confocal fluorescent image of compositional gradient with the left side sprayed with P2VP-b-PEO and no dye and the right side sprayed with P2vP-b-PEO and a fluorescent dye, (b) fluorescent intensity across (a) with distance directly matching, and (c) a single tile from (a), illustrating the dot arrays pattern as well as the resolution of (a).

3.2. Size as a Combinatorial Parameter

In addition to inking the pen arrays with uniform quantities of ink while varying their composition, it is possible to vary the quantity of ink on each pen as a means to change the rate of ink deposition. In this way, size gradients can be formed. It is important to note that while similar linear gradients have been previously achieved by patterning with pen arrays that have been deliberately tilted to change tip-sample contact area or contact time across the array, controlling feature size with ink loading affords the option of realizing non-linear and even non-monotonic gradients in patterned feature size.[27,47] In order to explore the concept, a single spray gun was used to deposit a gradient of ink quantity by spraying an aqueous solution of 5 mg/ml P2VP-b-PEO and 10 mg/ml rhodamine 6G onto one edge of a PPL array. Following the same protocol that was used in the previous experiment, the pen array was used to print a 25 × 25 array of dot features, which

was subsequently characterized by large scale fluorescence imaging (Figure 3.6A). The imaging revealed a clear gradient in fluorescence intensity across the array. Unlike in the previous experiment, the intensity variation was based upon a change in deposited feature size, a conclusion supported by measurements of the average feature size by atomic force microscopy (AFM) performed at different regions across the array (Figure 3.6B-D). Indeed, the average polymer feature size was observed to increase from 190 nm to 290 nm from the left to right side of the deposited pattern. It is important to note that while similar linear gradients have been previously achieved by patterning with pen arrays that have been deliberately tilted, controlling feature size with ink loading affords the option of realizing non-linear and even non-monotonic gradients in patterned feature size.
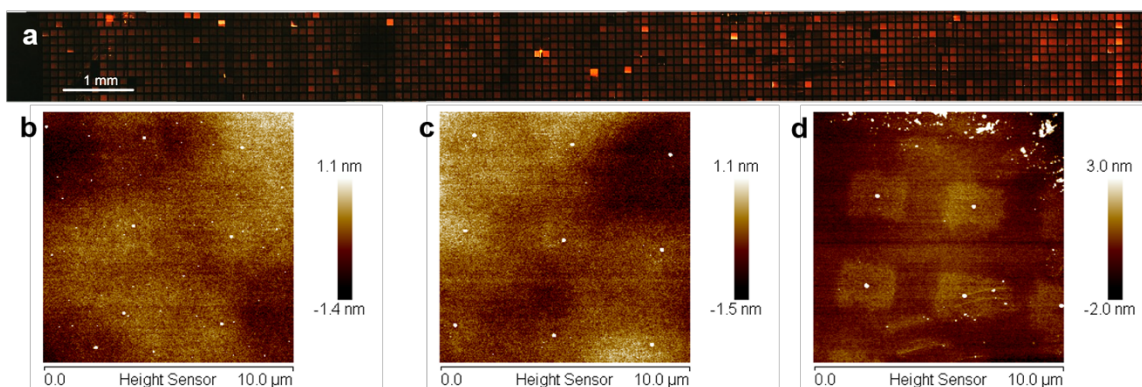
Figure 3.6. (a) Fluorescent image of a printed pattern generated by printing with a pen array sprayed only on the right side with 20 mM Rhodamine 6G. AFM images show the varying size of written features as they increase from the (b) left, (c) middle, and (d) right.

3.3. Megalibrary Synthesis

While the ability to generate patterns with compositional or size gradients separately is enabling, realizing combinatorial patterns with control over the size and composition of every feature in the pattern is the ultimate goal for high throughput screening. In addition to inking the pen arrays with uniform quantities of ink while varying their composition, it is possible to vary

the quantity of ink on each pen as well as composition at the same time. In order to explore the ability of spray-inking to generate such combinatorial libraries, a dual-spray inking experiment was performed in which the two airbrushes loaded with aqueous inks containing a hygroscopic polymer and a fluorophore were aimed above two adjacent corners of the pen array (rather than along a line that passes through the center of the array) (Figure 3.7 and 3.8E).
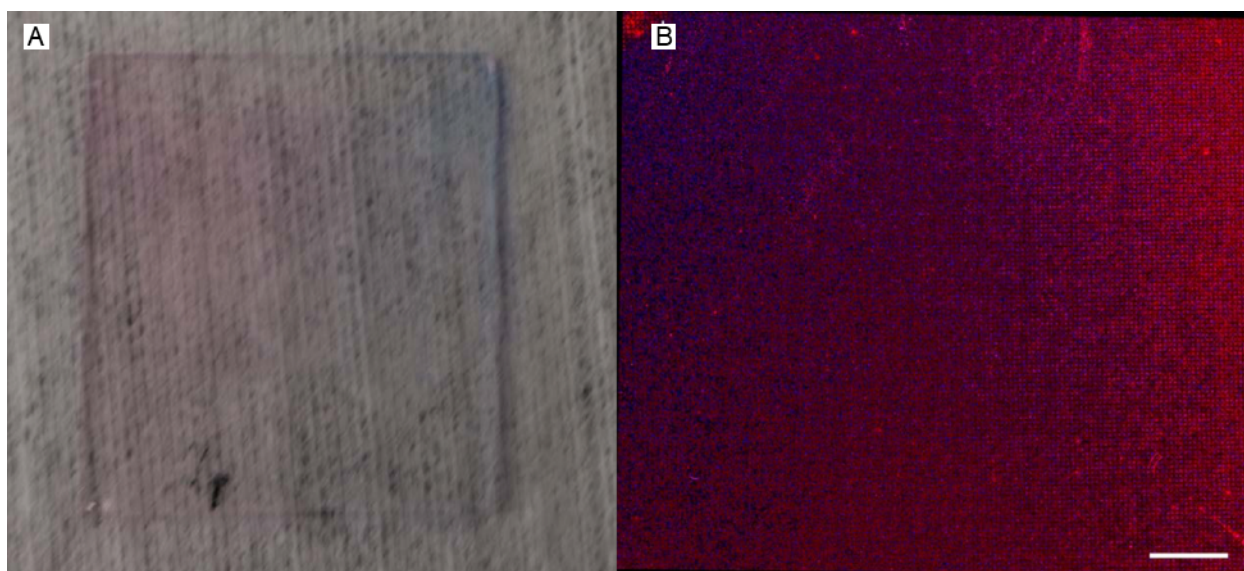
Figure 3.7. PPL array spray-coated with both a size and composition gradient. (A) Photograph and (B) confocal micrograph of the composition and volume gradient spray coated onto the PPL array, which results in a composition and size gradients when patterned.

Following the same patterning protocol as above, the pen array was used to write a massive scale array of dot features which were subsequently characterized with large scale fluorescence microscopy and atomic force microscopy (AFM) (Figure 3.8). Once again, variation of the features along the x axis resulted in a near linear fluorescent intensity gradient, but the features were no longer uniform along the y axis. AFM data show a non-linear gradient from 642 ± 46 nm to 1.1 ± 0.02 µm in diameter and 17 ± 9 to 3.6 ± 0.6 aL in volume (Figure 3.8C).
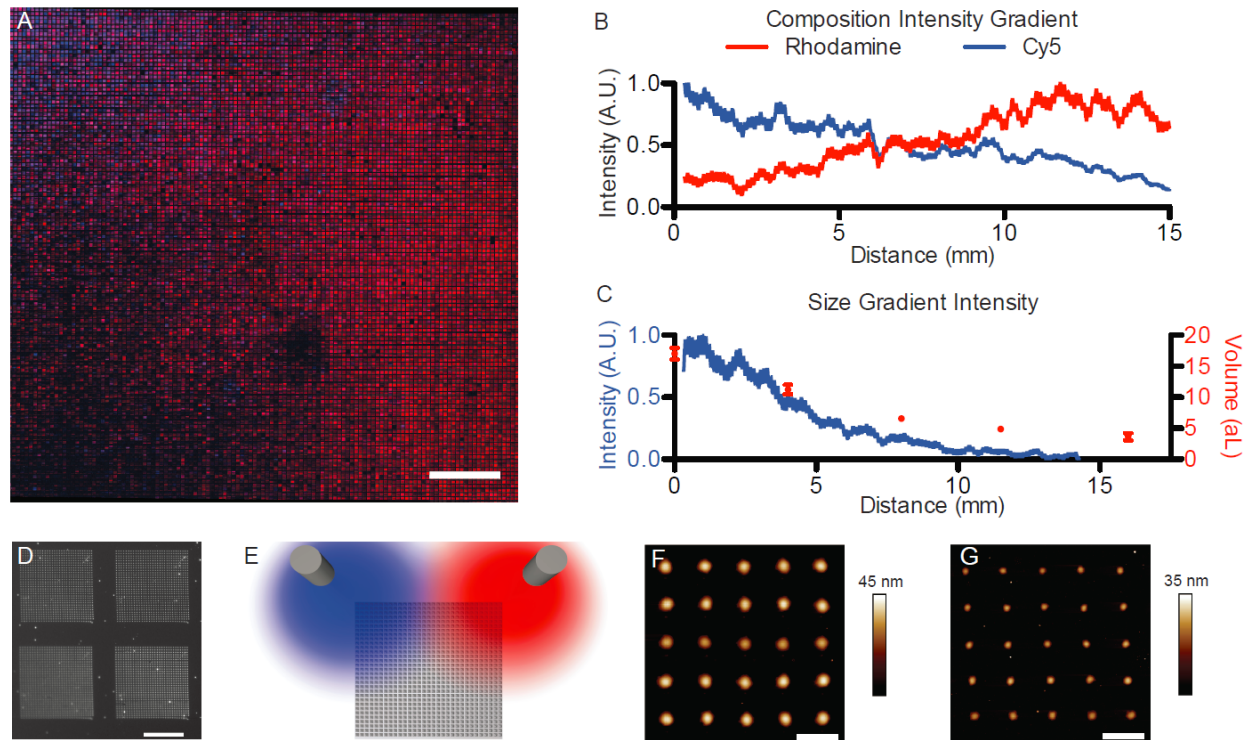
Figure 3.8. Large scale nanopatterned gradients of composition and size. (A) Stitched confocal fluorescence image of compositional and size gradients of two fluorophores in polymeric domes. Scale bar is 2 mm. (B) Average fluorescence intensity of each fluorophore across the array and (C) average total fluorescence intensity (blue curve) in the vertical axis plotted with the average volume of individual features as measured by AFM (red dots, error bars representing standard deviation). (D) High resolution darkfield micrograph of a region showing the patterns written by four pens. Scale bar is 50 μm. (E) Schematic of the airbrush position during spraying. (F) AFM of the largest patterned features (1.10 ± 0.02 μm) at the top of the array, and (G) AFM of the smallest patterned features (642 ± 46 nm) at the bottom of the array. Scale bars are 3 μm.

3.4. Nanoparticle Megalibraries and Their Applications

With the power to synthesize megalibraries, the key is to pair it with the right screening technique. While my PhD was the development of the synthesis side, I have been able to work with great collaborators to start to answer this problem for certain applications. The original idea of the megalibraries platform was to pair it with scanning probe block copolymer lithography (SPBCL). To go into greater detail from Chapter 1, SPBCL is a technique that was invented in the Mirkin group (Scheme 3.2)[154, 156, 157] that deposits attoliter volumes of ink with high spatial

resolution. The ink is composed of two components: a block copolymer and a metal precursor that is coordinated to the vinyl pyridine group of the block copolymer. The patterned polymer dome acts like a nanoreactor, forcing all the metallic precursors to aggregate together and form a single nanoparticle through a two-step heating process. In the first step, the temperature is heated up such that the polymer does not degrade but the metallic precursor starts to dissociate with the pyridine group and subsequently aggregate together. Then the nanoreactors are heated up to 500°C where the polymer burns away and the metallic precursor is reduced to form a single nanoparticle. In addition, multiple metallic precursors can be incorporated into the ink. In this way a single multimetallic nanoparticle can be synthesized in each nanoreactor. Furthermore, this process is not limited to metals that are miscible with each other. This feature allows the formation of Janus nanoparticles that have two or more separate domains and a phase boundary. Since the nanoreactor forces the precursors to form a single nanoparticle, nanoparticles can be made that are not currently possible by any other method. This has allowed for the synthesis of monometallic to pentametallic nanoparticles with every combination in between. This combinatorial way of synthesizing nanoparticles is making it possible to simply and efficiently synthesize nanoparticles that can be screened.
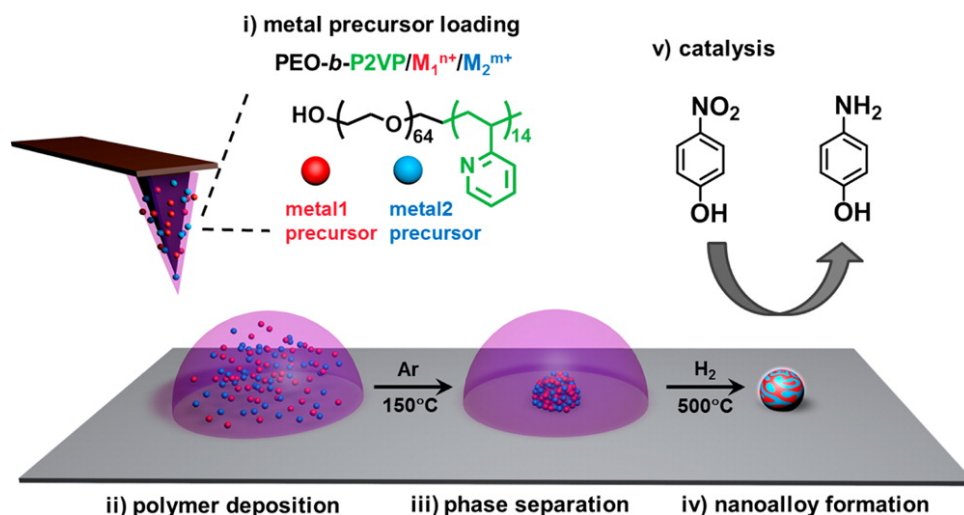
Scheme 3.2. "Polymer-Mediated Tip-Directed Synthesis of Alloy Nanoparticles Using SPBCL The process consists of five steps: (i) Multiple metal ion precursors are coordinated onto a block copolymer, poly(ethylene oxide)-*block*-poly(2-vinylpyridine) (PEO-*b*-P2VP). (ii) The polymer is cast onto AFM tips or polymer pen arrays and then deposited at desired locations on a substrate. (iii) The substrate is annealed at 150 °C under Ar, allowing the metal ions to aggregate in the polymer nanoreactors. (iv) The substrate is thermally annealed at 500 °C under H_2 to reduce the metal ions and decompose the polymer, forming single alloy nanoparticles in each reactor. (v) The as-prepared alloy nanoparticles are utilized to catalyze the reduction of 4-nitrophenol into 4-aminophenol."[157] Reprinted with permission from ref (157). Copyright 2015 American Chemical Society.

While the previous sections with dual spray coating experiments focused on patterning gradients with easy to detect fluorophores as a proof-of-concept, it is important to validate that combinatorial libraries may be generated using substances where the function can in principle dramatically change across the array. When combined with SPBCL, functional multimetallic nanoparticles with gradients of composition can be synthesized. To determine if combining SPBCL and dual spray-coating will generate compositional gradients, we explored the patterning of metal ion-loaded block copolymers that can be quantified using X-ray fluorescence (XRF).[171] To explore the patterning of these inks, a pen array was dual spray-coated with spray guns with aqueous solutions of P2VP-*b*-PEO, one with 18.75 mM auric acid and the other with 18.75 mM sodium tetrachloropalladate. Following spray inking, this pen array was used to pattern features

on a hexamethyldisilazane- coated silicon wafer. The resulting features were characterized using XRF, which allowed for the calculation of the local atomic ratio of Au to Pd in sections across the array (Figure 3.9). As expected, the atomic ratio of Au to total Au and Pd varied from 9% to 88%. Therefore, this is an effective technique for preparing PPL arrays, inked with compositional gradients, and useful for synthesizing combinatorial libraries of nanoparticles by SPBCL.
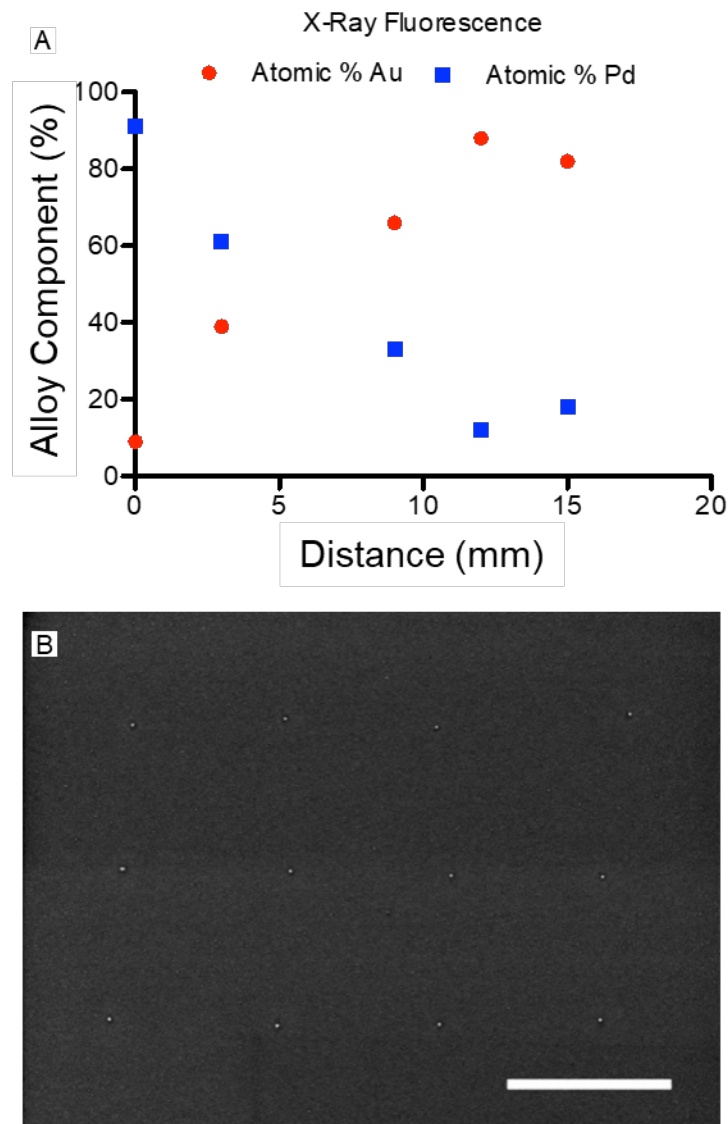
Figure 3.9. 14 million bimetallic nanoparticles synthesized in parallel with a compositional gradient. (A) X-ray fluorescence profile of Au-Pd alloy composition of SPBCL patterned array taken with a 3 mm slit, note that the last point is at the edge of the array. (B) SEM of SPBCL Au-Pd nanoparticles. Scale bar is 2 μm.

Qualitatively, it is observable (Figure 3.9 that going from the Au-rich (right) to Pd-rich (left) side of the substrate, the Au Lβ fluorescence intensity decreases while the Pd Kα fluorescence intensity increases as would be expected (Figure 3.10). Quantitative analysis of the Au and Pd relative atomic percentages were conducted using corrected areas under the Pd Kα (21177 eV) and

Au Lβ (11443 eV) fluorescence lines, with peak areas fit to a Gaussian distribution after background subtraction using Origin 8.6 graphing software. Intensity values were corrected for dead-time, incident beam intensity, elemental cross-sections, detector efficiency, and attenuation due to species present between the sample and detector at the relative fluorescence line energies.
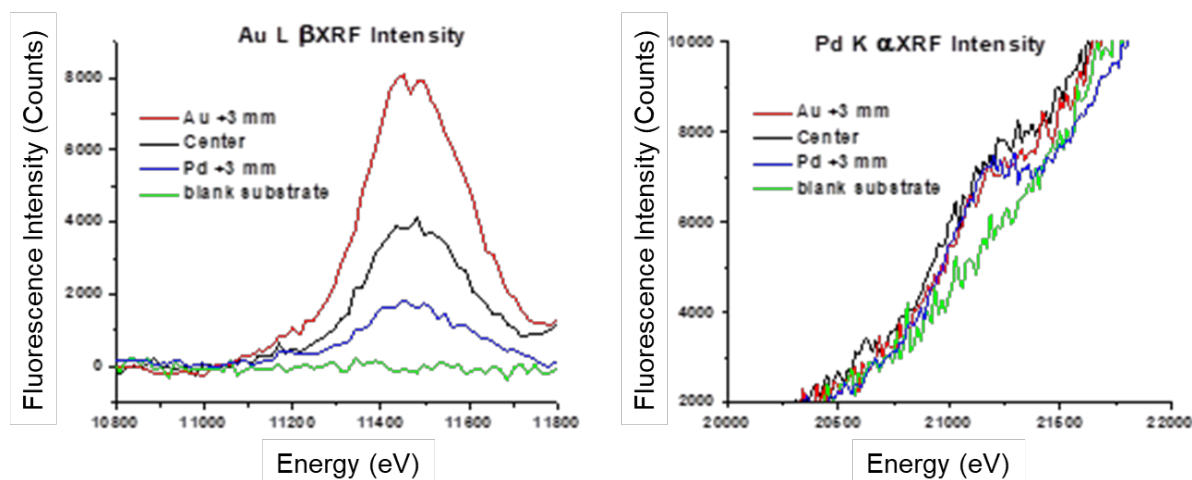
Figure 3.10. Au Lβ and Pd Kα Fluorescence Intensities. The Au Lβ fluorescence line intensity (left) increases towards the Au-rich side of the sample and decreases towards the Pd-rich side. No signal is observed for the case of a blank substrate (green). The Pd Kα fluorescence line intensity (right) decreases towards the Au-rich side of the sample and increases to a well-defined peak (blue) towards the Pd-rich side of the spectrum. +3 Au refers to a 3 mm offset from the sample center towards the Au-rich (right) side, and +3 Pd refers to a 3 mm offset from the sample center towards the Pd-rich (left) side.

Here, we have shown that by spray-inking PPL pen arrays, it is possible to synthesize combinatorial megalibraries containing millions of sub-micron features over centimeter-scale regions. The physical processes that make this capability possible include the mixing of sprayed inks during the drying process and capillary effects that bring the majority of the applied material to the pens. These relationships suggest a subtle connection between ink viscosity, volatility, and surface tension which warrant further exploration.

Importantly, the simplicity with which it is possible to define these combinatorial arrays of nanomaterials bears important consequences for many fields of study as such arrays could be

useful as discovery platforms in areas as diverse as nanophotonics, heterogeneous catalysis, and drug discovery. The applications and possibilities of this megalibrary system has already been demonstrated with the discovery of a new optimal carbon nanotube catalyst as outlined in Chapter One. Gradients of Au-Cu bimetallic nanoparticles were synthesized and screened for activity by *in situ* Raman spectroscopy with respect to single-walled carbon nanotube (SWNT) growth. Au_3Cu was identified as the most active composition (Figure 1.4 D). This composition of nanoparticle has never been identified as a catalyst for SWNT growth before this experiment. With more studies like this not only will new materials for applications be discovered, but also a deeper understanding of structure-function relationships can be derived.

4. Chapter Four

Liquid Mask Etching and Nanoscale 3D Printing
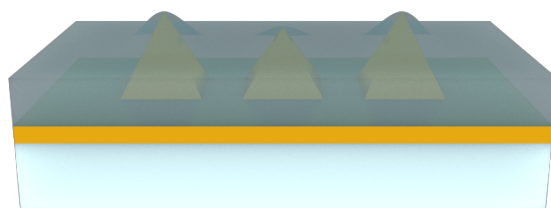
4.1. Liquid Masks for Microfabrication Processes

Utilizing polymer pen lithography (PPL), large area combinatorial libraries have been fabricated and screened through direct deposition of material onto the surface. While this system is powerful, it is limited to direct patterning of materials. Beam pen lithography (BPL) was developed to further broaden the nanolithography capabilities of cantilever-free lithography by delivering energy rather than material. In this way, it opens cantilever-free scanning probe lithography to the toolbox of chemistries available and well developed for photolithography. This gains access to a large library of materials, but with a higher resolution and without the need of a clean room. BPL utilizes the pyramidal pens from PPL that are coated with a reflective surface coating such as gold with apertures at the apex of the tip of each pen. These apertures allow the user to deliver energy via light in a highly-controlled manner by funneling the light sent through the pyramid to the apertures. When the aperture is smaller than the diffraction limit of light and the array is sufficiently close to the surface, sub-diffraction limit features can be obtained.[46] One major limitation in BPL as is the case with PPL is an inhomogeneity in the apertures formed over large areas due to a pen-to-pen height variation inherent to the fabrication of cantilever-free arrays. This variation occurs during the fabrication of the silicon master that acts as a mold to cast the polymer pen array due to variations in the etching of the array as well as the tolerances of the square base dimension from the photolithography steps. These ultimately result in height variations of the array that can be greater than 1 µm in size. The most notable way to solve this is by having higher tolerances at every step of the master fabrication. This has shown some success with smaller arrays in the low thousands but does not work as one scales from 9,100 pens to well over a million pens. For this reason, a new technique for a new aperture fabrication or master fabrication is

needed. While master fabrication improvements are possible, the most viable solutions are outside the realm of research labs and thus would never see adoption, so I pursued a new aperture fabrication method. For this same reason, hard transparent arrays were developed in Chapter 2.
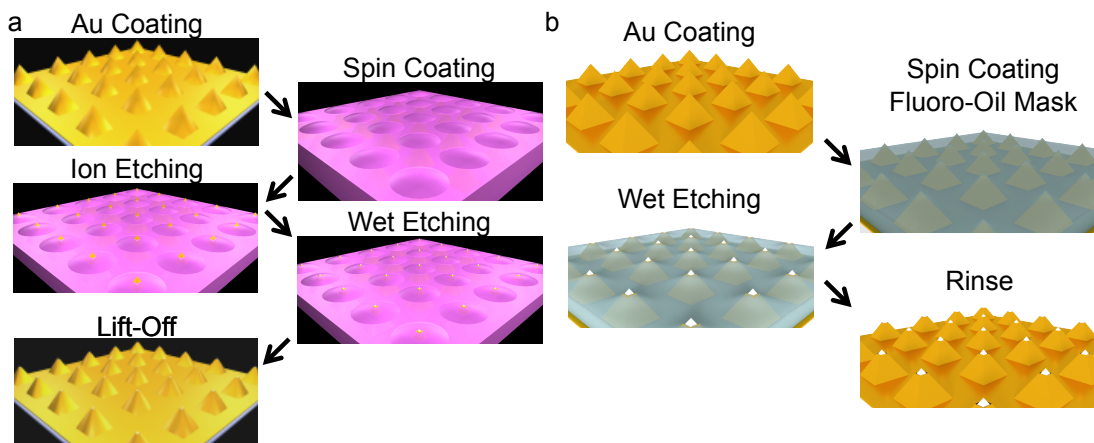
Scheme 4.1. Etching beam pen arrays both previous method and liquid mask etching. (A) Etching beam pen arrays through a spin coated photoresist mask.[46] (B) Liquid mask etching of beam pen arrays that enables even etching across inhomogeneous arrays.

In the BPL system, this pen-to-pen height variation issue still needs to be addressed since it results in variations in aperture size as a result of how it is fabricated. The current method for etching apertures into beam pen arrays is to 1) spin coat a uniform layer of photoresist onto an Au coated pen array, 2) perform a top down dry etch to expose the pyramid tip at a given height from the base of the pyramid, 3) perform a wet etching step to remove the exposed gold, and 4) remove the remaining photo resist (Scheme 4.1A).[172] E-beam lithography has also been successful in defining sub-diffraction apertures.[86] However, this technique is prohibitively time consuming and impractical for defining apertures in a large scale. To scale up to millions of pyramids, it is necessary to develop a new method for etching that accounts for pen-to-pen height variation. When spin coating over large BPL arrays, there exists local uniformity (on the millimeter scale) but global inhomogeneity from one side of an array to another (several centimeters). This is most

evident in when there is a gradient in the backing layer thickness from one side of an array to the other. In this situation, attempting to apply an even masking layer on top of the pens with a height gradient will cause a gradient of tip exposure through the masking layer (i.e. some features will be over exposed and above the mask while some will remain well below the mask completely un-exposed). Such variations in exposed areas eventually leads to inhomogeneous structures in etching of the apertures. Also, while the local uniformity equates to an even layer of photoresist, the pen to pen variation requires a different coating condition for each pen. Thus, aperture variation can be multiple microns in size even with a target of nanometer scale apertures. To advert such an occurrence, a self-leveling mask can be implemented to adopt the contours of the features by coating the irregular surface in way that leaves evenly exposed features. Having a mask that can evenly coat the tip of every pen rather than evenly coat relative to the base is necessary for even etching. To create this, a new type of protective mask has to be used: liquid mask.
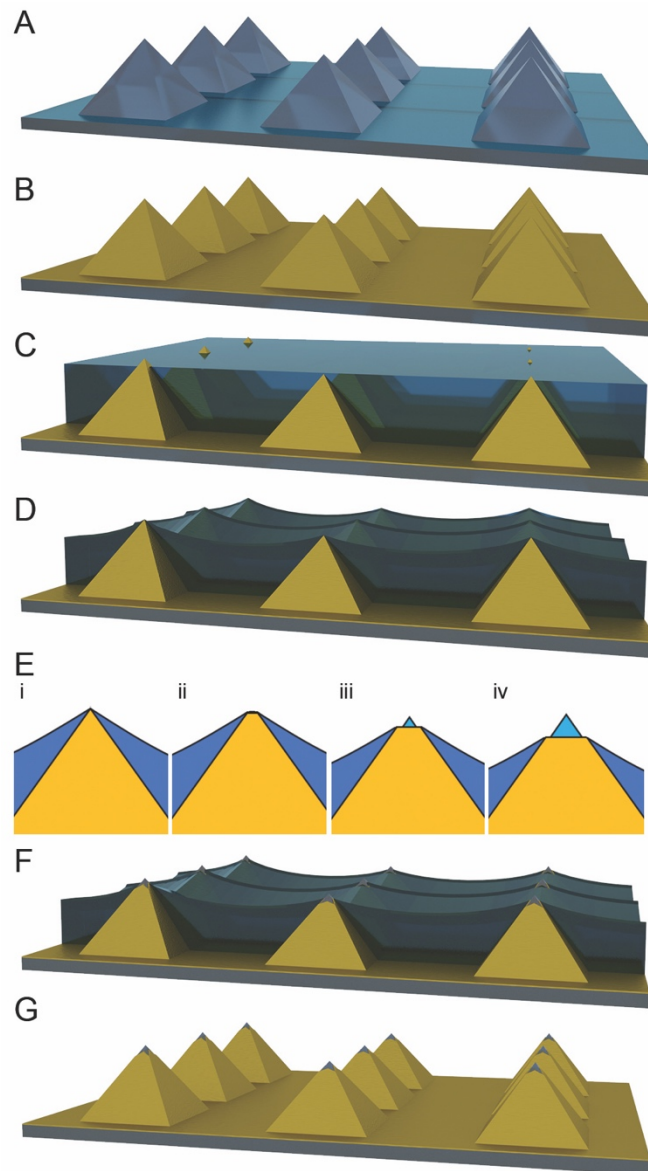
Scheme 4.2. Liquid mask etching process. (A) The process starts with polymer pen lithography array. (B) Gold is deposited onto the array followed by thiol fluorinated surface treatment. (C) Oil is spin-coated onto the array and (D) heat treated to allow oil to form menisci between the pens. (E) Etching process in gold etchant bath as the oil layer retracts as the gold resolves from (i-iv). (F) Beam pen arrays after etching with oil still on that is then (G) washed to remove the oil and is then ready for use.

By spin coating a fluoro-oil over a fluoro functionalized BPL array, this self-leveling liquid mask can be used rather than a photoresist that is chemically inert to the etching solutions (Scheme

1B and 2). When the oil layer is thinner than the height of the BPL array, the interaction between the oil and the BPL array enables the oil to wet the pyramids and form meniscuses between each pyramid. Since a meniscus is formed rather than a flat layer, the tip exposure is not dependent on the pen height since the oil wicks up to the apex of the tip (Figure 4.1A). This eliminates microscale problems of tip to tip variation and macroscale problems like backing layer variation across the array.
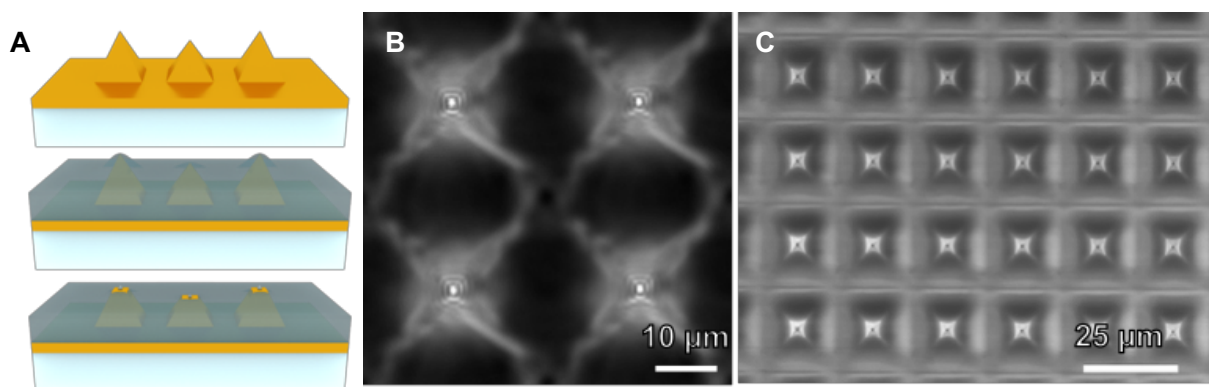
Figure 4.1. Beam pen array etching process. (A) Scheme of liquid mask evenly covering tips regardless of height, (B) diffraction pattern formed as the oil wicks up the tip apex, and (C) exposed apertures by overspinning after etching to better visionalize the array.

Many different fluoro-oils were experimented with to optimize the etching of BPL arrays. While lower viscosity oils coated the array more uniformly, it is more prone to displacement by the etching solution when submerged into the etching bath. Higher viscosity oils on the other hand would not properly wet the array at room temperature but performed better as a mask since the higher viscosity gave properties closer to that of a photoresist. In order to obtain both of these features together, a high viscosity oil was spin coated onto a BPL array. Then, the array was heated on a hot plate to lower the viscosity and allow the oil to evenly wet the array (Scheme 4.2D). This

was followed by a final spin coating step to create the proper three-phase interface at the apex of each pen. This three-phase interface consisted of the solid pen, liquid oil, and air (Scheme 4.2E). By having all three come perfectly together, it enables etching to occur right at this point. Under the microscope, this can be seen by diffraction lines appearing at the tip (Figure 4.1B). The array was then allowed to cool back to room temperature prior to being placed into the etching bath.

Now, multimillion pen arrays can be uniformly etched over a 1.75" by 1.75" area with an average aperture size of 266 nm by 354 nm and a 3-9% variance in size across the entire array (Figure 4.2). This method has increased uniformity and shows promise for reaching sub diffraction apertures with future optimization of etchant and spin coating conditions.
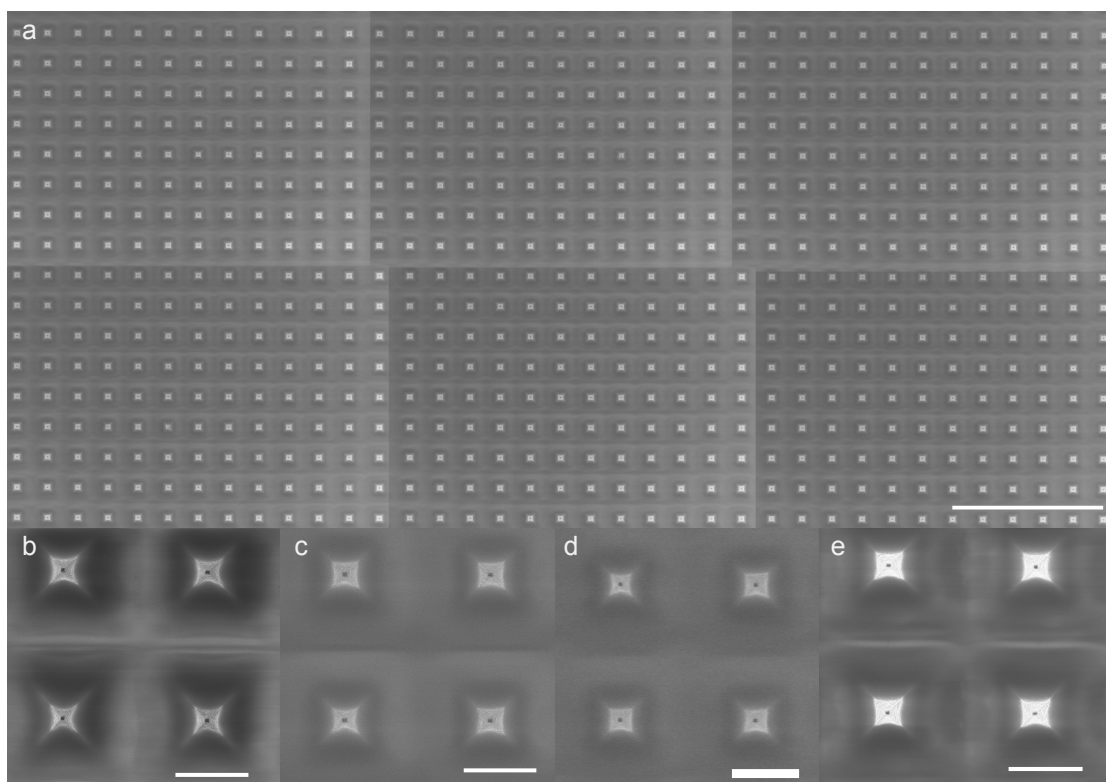
Figure 4.2. Large area uniform beam pen etching. (A) Stitched SEM image of hundreds of uniformly etched pyramids, scale bar 100 μm. Zoom in SEM image of the (B) top left, (C) top right, (D) bottom right, and (E) bottom left corners of the array showing high aperture uniformity across the entire array, scale bar 10 μm.

This new conformal-masking technique enables the fabrication of mega-BPL arrays, consisting of over 4 million individual pens with highly uniform aperture dimensions. This represents over a 500-fold increase in the number of successfully etched beam-pens on a single array from previous reports.[46] The surface-tension of fluids gives them the propensity to overcome gravitational forces at the micro-scale and to climb surfaces forming menisci. By exploiting this interaction, we are able to generate conformal masks which coat the pens from the apex down, irrespective of pen-to-pen height variations, prior to wet etching of the metallic layer. We can then use etchant reaction time and concentration to control the size of aperture formation. Importantly, the high degree of reproducibility of BPL pen array fabrication allows for standardization of BPL array hardware and its integration into semi-automated printing systems. We have integrated our pen designs with automated patterning tools provided by Tera-Print, LLC so as to enable the wide-scale application of this highly versatile platform technology. With the Tera-Print E-series, a pattern was fabricated with varying the exposure time and force. This resulted in a pattern with feature sizes varying from 350 nm to 1.2 µm utilizing 300 nm aperture beam pen array (Figure 4.3). Ultimately, this method has increased uniformity and shows promise for reaching sub diffraction apertures with future optimization of etchant and spin coating conditions.

Force (400-1200mN)
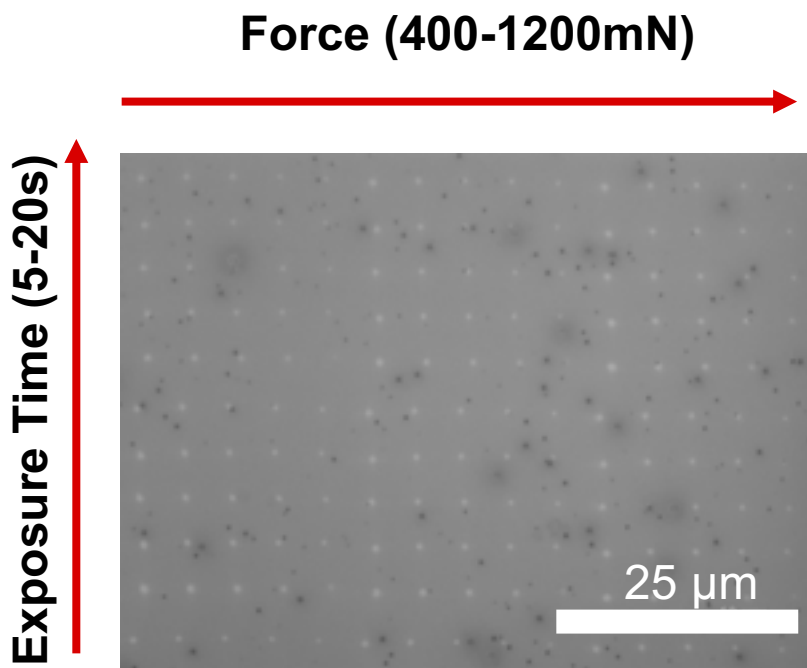
Figure 4.3. Pattern made using liquid masked etched array and Tera-Print E-Series instrument. Each pen was spaced 30 µm apart and patterned a dot array that had variations in exposure time and contact force resulting in feature size range from 350 nm to 1.3 µm from 350 nm apertures.

4.2. Nanoscale 3D Printing over Macro Length Scales

BPL has been optimized to print a library of hard and soft materials on a 2D surface. Furthermore, BPL builds off of traditional photolithography, enabling an even larger library of materials yet to be utilized and adapted to BPL. When transitioning from two to three dimensions in a print, new factors must be considered. One of the most important factors is that continuous printing can lead to fouling of the BPL array. In a solution, polymerization occurs at the tip leaving a residue of polymerized ink, which does not occur for a traditional photoresist. This will build up over time and result in either blocked light or shearing off gold from the array resulting in enlargement of the aperture. To overcome this challenge, I have developed an antifouling coating.

This coating is made from a fluoro-oil that thinly coats the pen array. With this liquid coating, any damage cause by polymerized ink will self-heal by the very nature of being a liquid. In addition, the inert nature of the fluoro-oil makes it compatible with our orthogonal ink chemistries.

To ensure that the ink phase does not wet between the oil and array, two steps have been put in place. First, the gold surface has been fluorinated to promote adhesion between the array and oil layer. Second, the entire beam pen system has been inverted and an ultra-high density fluoro-oil has been chosen. In order to utilize this new configuration with an anti-fouling layer, a whole new system was built. Previous PPL and BPL systems were made by modifying atomic force microscopes (AFMs), but this route is not possible for an inverted system. Here, I have built a dedicated system from the ground up (Figure 4.4A). Utilizing a force sensor, an actuator in the z direction is placed in contact with the surface of the array. UV light was then turned on and the substrate was retracted at 1 µm/s (Figure 4.4B). With a 2 µm aperture, 4 µm pillars were printed (Figure 4.4C).
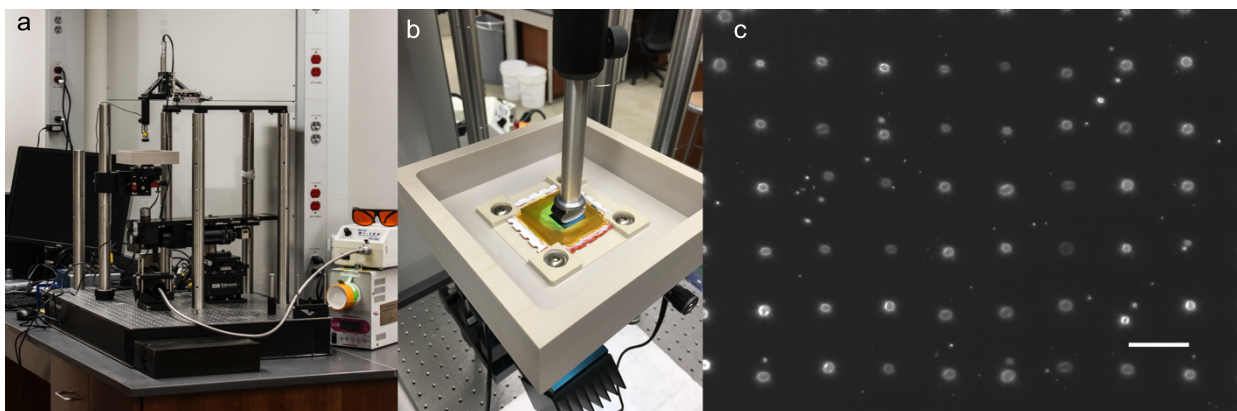
Figure 4.4. Cantilever-free scanning probe lithography 3D printer. (A) Image of inverted BPL system designed for continuous nanoscale printing. (B) Image of the fluid cell with print coming off of inverted beam pen array. (C) Patterned polymer pillars from inverted BPL system, scale bar 20 µm.

5. Chapter Five

High Area Rapid Printing with Fluid Flow Technology
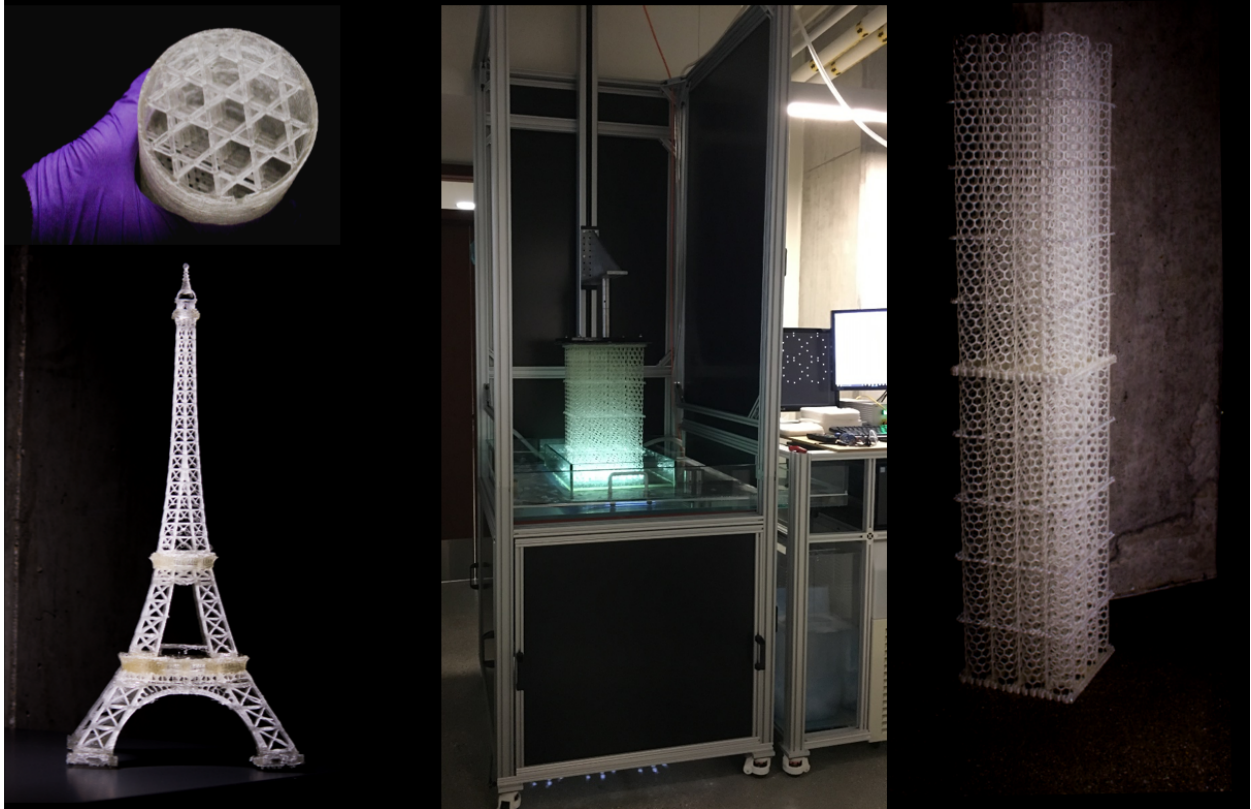
5.1. Introduction

Additive manufacturing has been a disruptive force in the fields of design and manufacturing [173-178]. It has been used primarily for prototyping, drastically reducing the time between product ideation to manufacturing, but has recently begun to make notable progress in the manufacturing sector [179, 180]. While there have been many important advances in the printing of 3D plastics [181], one of the most promising additive manufacturing approaches is stereolithography (SLA), which utilizes photocurable liquid resins that can be chemically formulated to yield materials with a large range of attractive mechanical properties [182, 183]. Conventional SLA operates by using UV light to cure liquid photoactive resins on a vertically moving plate; this is done repeatedly and results in a desired 3D object consisting of stacked 2D layers [184]. DeSimone and co-workers introduced a field-changing variation on SLA called continuous liquid interface printing (CLIP), which utilizes oxygen inhibition to create a reaction 'dead-layer' [185, 186]. This 'dead-layer' prevents adhesion between the emerging part and the bottom of the print vat, removing the need to repeatedly mechanically cleave the part from the vat [184]. This continuous print approach increases vertical print speeds 100-fold, while simultaneously removing material defects intrinsic to the aforementioned layer-by-layer lamination approaches. With this advance, SLA was transitioned from prototyping to direct manufacturing. However, with CLIP, it is the oxygen 'dead-layer' that is both its enabler and limiter. The polymerization reactions employed in SLA photoresins are highly exothermic, and at 100-fold faster print speeds, heat dissipation is daunting [187, 188]. Moreover, by requiring a dead-layer, which is delivered in the form of a gas and acts as a thermal insulator, CLIP has limited cooling options which can span the area of the print bed. For this reason, commercial systems that utilize CLIP rely on small print beds or

slower vertical print speeds so that structures can be printed without generating temperatures that result in part degradation.

In this chapter a 'dead-layer' free approach to rapid SLA printing, HARP (high-area rapid printing), which is capable of continuously printing over large areas and at rapid vertical print speeds. The printer operates on the principle of a UV-curable resin floating on a bed of flowing immiscible fluorinated oil to minimize interfacial adhesion at the build region. Aizenberg and co-workers have demonstrated the great breadth of de-wetting behavior possible when utilizing fluorinated liquids imbedded within solid matrices for applications in medicine and marine biofouling [189, 190]. HARP builds upon this concept by keeping the fluorinated phase in constant motion relative to the emerging printed part, further decreasing the adhesion forces (i.e., static vs. dynamic) and generating a solid-liquid slip boundary. By replacing traditionally static and solid interfaces with a mobile liquid, the HARP 3D printer has the vertical print speed of CLIP but with, in principle, a limitless print bed size. The oil can be recirculated through a heat exchanger to cool or heat the build region and maintain thermostatic control across the entire print bed. Additionally, the oil can be continuously filtered to remove the micro-particulate solids, which are generated by SLA and decrease resolution through light-scattering (commonly referred to as 'clouding') [191]. Finally, since HARP does not require an oxygen 'dead-layer', it can be used with both oxygen-sensitive and insensitive ink chemistries, significantly increasing the scope of applicable resins and resulting materials.

5.2. Flow Profile of Flowing Interface
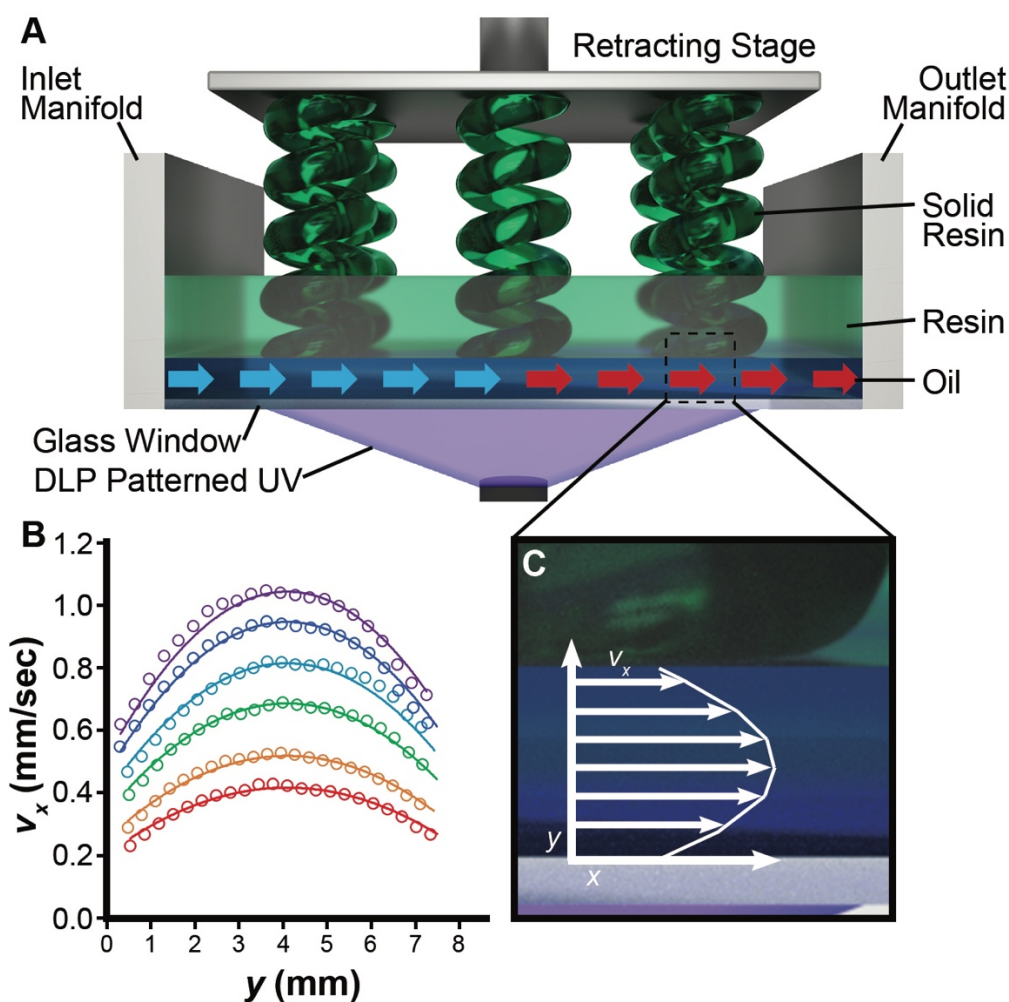
Figure 5.1. Flow profile of a mobile interface that enables continuous printing. (A) Scheme of a 3D printed part emerging from the HARP 3D printer, (B) velocity profile under printed part at different flow speeds demonstrating the presence of a slip boundary (colors represent increasing volumetric fluxes, q; *red* is $q = 0.21$ mm/sec, *orange* is $q = 0.30$ mm/sec, *green* is $q = 0.44$ mm/sec, *teal* is $q = 0.56$ mm/sec, *blue* is $q = 0.66$ mm/sec, *violet* is $q = 0.75$ mm/sec; open markers are experimental data points from particle imaging velocimetry and continuous lines are fits from an analytical model), and (C) scheme inset of the slip-boundary flow profile under the part with a representative flow profile depicted.

HARP operates through a mobile liquid interface which creates a shear stress beneath the emerging part and results in a slip boundary (Figure 5.1). The slip boundary allows for the solidified part to be continuously retracted from the print interface, without the need for a rate-limiting mechanical cleavage step. In the system here, fluorinated oils (perfluoropolyether copolymers, such as Solvay Fomblin Y or Chemours Krytox GPL) were chosen for their omni-phobic properties and higher densities relative to that of common SLA resins. While other immiscible liquid systems were explored, including densified water and glycols, neither of these aqueous options produced the same quality of de-wetting behavior with the emerging 3D printed part and resulted in lower-quality print production (Figure 5.2). A pair of inlet and outlet manifolds were fabricated to distribute a laminar flow of oil across the print-bed with a uniform velocity profile (Figure 5.3). This flow profile ensures that the oil layer remains optically uniform across the build platform (i.e., no turbulence giving rise to optical distortions at the oil/resin interface) and results in a uniform interfacial-shear stress being applied to all solidified parts. Additionally, the oil flowing through this system can be cooled and used as a UV-transparent heat sink that spans the build platform, enabling thermostatic control of the print process. Heat removal from the build-region becomes a limiting bottle-neck for other rapid-print techniques, forcing the print process to slow down to maintain thermostatic control. Here, we have integrated active heat dissipation in direct contact with the build-region to maximize the rate of overall heat dissipation without the added thermal resistance of a glass-window or oxygen feed layer.
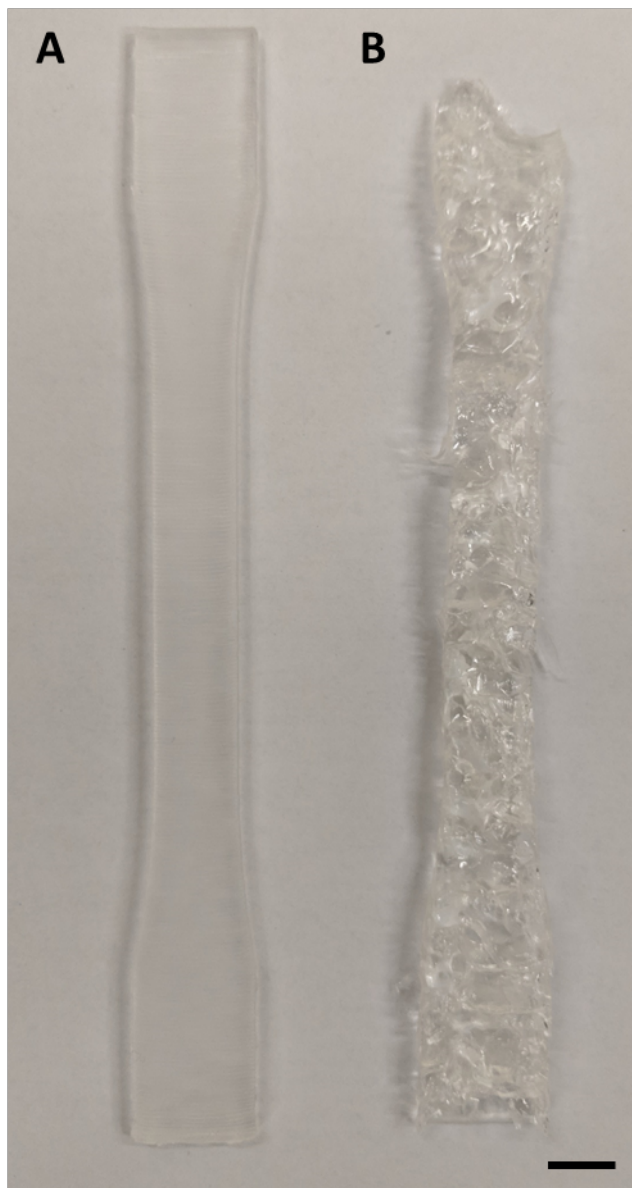
Figure 5.2. Example Part Printed on Glycol. ASTM D638 Type 1 dog bones printed on (A) fluorinated oil, and (B) glycerin. As can be seen, parts printed on glycerin result in 'flaky' and hollow parts owing to the subpar de-wetting behavior of the immiscible phase. Scalebar is 1 cm.
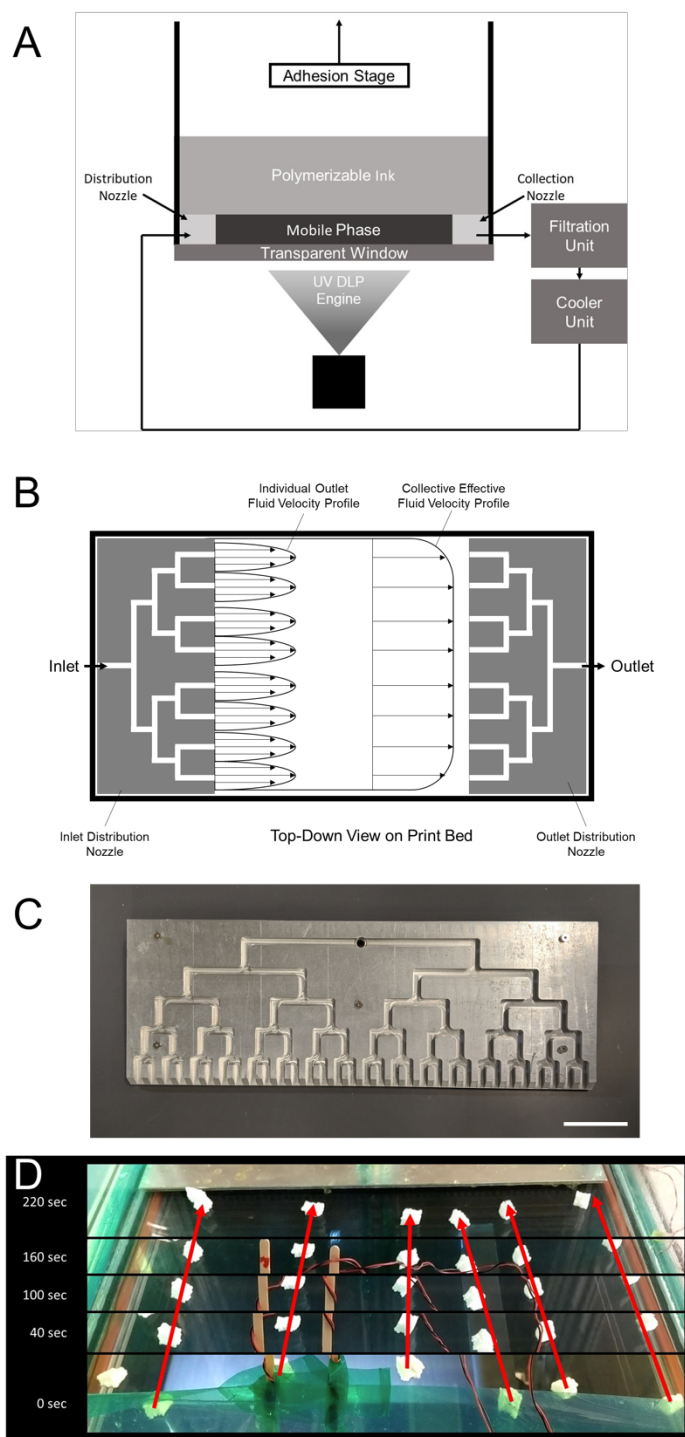
Figure 5.3. Manifold flow profile. (A) Scheme depicting the oil flow loop, (B) scheme of the manifold system and flow profile that ensures a uniform flow across the print bed, (C) image of a machined aluminum manifold design; 15" wide with 2" scale bar, and (D) time lapse of tracer particles floating within the uniform flow field at a consistent rate (30" wide, 18" deep).

To confirm our hypothesis of a slip-boundary being central to our printer's operation, particle imaging velocimetry was used to analyze the cross-sectional fluid-flow profile as the oil passed beneath a printed part (Figure 5.4).[192] Slip-boundary conditions are notoriously difficult to observe due to randomized optical reflections which occur at the interfaces under study, resulting in noisy data.[193, 194] To rectify this problem an analytical model, allowing for the possibility of either a *slip* or *non-slip* boundary condition, was fit to the center of the flow-profile (*i.e.*, where high quality data can be collected). The model allowed for a classical Navier slip-boundary to arise when the interfacial shear-stress exceeded a given critical shear-stress.[195] From this analysis, the slip-boundary model best captured the dynamics of the experimental data (Figure 5.1B, Section 5.4, and Figure 5.5). This is best reflected in the experimental velocity profiles ($v_x(y)$, open markers in Figure 5.1B) as a function of the oil flow rate (increasing volumetric flux, from red to violet) and the corresponding Navier slip model fits (solids lines, Figure 5.1B).
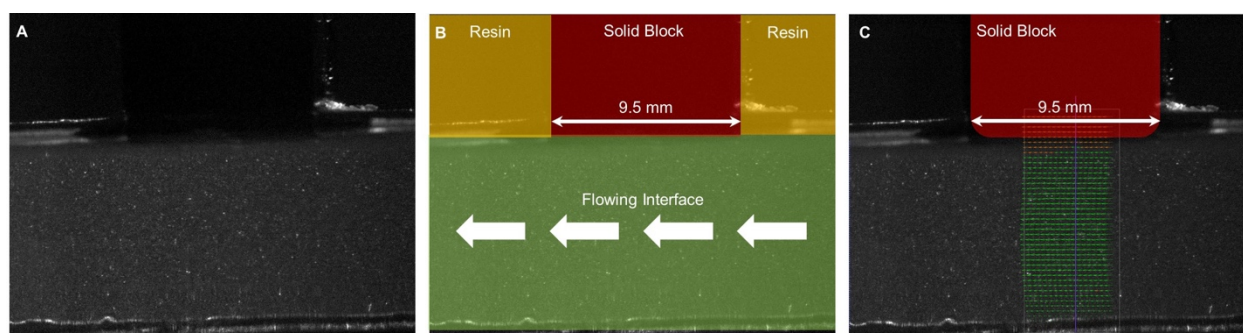
Figure 5.4. Particle flow velocimetry. (A) Optical image of the PIV experiment in process. The bottom layer consists of oil with light scattering micro-particles (white dots). (B) Labeled overlay of (A) with components color-coded for clarity. (C) Representative flow profile of the mobile interface calculated from particle-tracking analysis; the white box represents the region of interest and the blue line represents the poly-line from which $v_x(y)$ is exported, and the small green arrows represent the flow velocity vector field at each point.
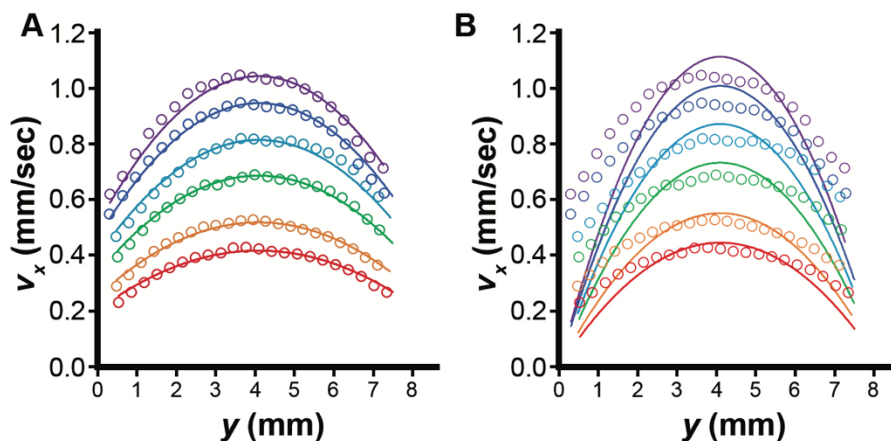
Figure 5.5. Fluid Flow Profiles and Model Fit. (A) velocity profile under printed part at different flow speeds demonstrating the presence of a slip-boundary (colors represent increasing volumetric fluxes, q; *red* is $q = 0.21$ mm/sec, *orange* is $q = 0.30$ mm/sec, *green* is $q = 0.44$ mm/sec, *teal* is $q = 0.56$ mm/sec, *blue* is $q = 0.66$ mm/sec, *violet* is $q = 0.75$ mm/sec; open markers are experimental data points from particle imaging velocimetry and continuous lines are fits from an analytical model). (B) The same experimental velocity profiles as in (A), but overlaid with model fits when the model is constrained to *non-slip* boundary conditions.

5.3. Oil Flow, Particle Image Velocimetry, and Modeling of Slip Boundary

Central to the HARP 3D printing technology is the mobile liquid interface. This flow is critical as it generates a shear-stress with the emerging object and mitigates the adhesive and cavitation forces between the bottom of the printed part and the oil. In scenarios without oil flow, as the cross-sectional area becomes larger the oil is pulled above the average oil level in the vat to create a bubble of oil. Eventually, gravity overcomes this force and the bubble of oil drops, often resulting in the failure of the part. Alternatively, when the oil is allowed to flow at even modest fluxes a slip-boundary is formed, and the cross-sectional area of the part being printed can be drastically increased.

Particle image velocimetry (PIV) was used to observe the oil flow behavior as a function of the volumetric pump flow rate (50% to 100% power). Video was collected of right-angle

scattering, and then processed in PIVlab. Within PIVlab, the following settings were used to generate a velocity map profile:

(i)   a region of interest was defined under the printed part (corresponding roughly to the area indicated in Figure 5.4C)

(ii)   the image stack was pre-processed with the CLAHE filter (10 px), high pass filter (50 px), denoise filter (5 px), and auto contrasting

(iii)   the PIV analysis was performed with the default settings of a FFT PIV algorithm, a Pass 1 integration area of 64 px and step of 32 px, a Pass 2 integration area of 32 px and step of 16 px, a linear deformation interpolator, and a Gauss 2x3 sub-pixel estimator

(iv)   post-processing vector validation was performed with a v_x limit of 20 px/frame and removal of vectors outside of 2x the standard deviation of the vector set; this removes outlier reflections at the interfaces or in regions where there are solid objects

(v)   a vertical poly-line was drawn through the region of interest (starting in the glass aquarium bottom, up through the oil, and into the solid 'printed' object); the lateral velocity (v_x) along this y axis was exported for analysis

(vi)   each volumetric flux condition (50%, 60%, 70%, 80%, 90%, and 100% pump intensity) was off-set corrected based upon where the poly-line from step (v) began and ended (i.e. Δy offset correction between data series)

(vii)   vectors overlapping with solid objects or influenced by the 'moving-average' integration area (based upon the pass integration areas used in step (*iii*)) near the

edges of the solid object were discarded; this was easily detected by looking for

the inflection point in the 2nd differential of the experimental data ($d^2(v_x)/dy^2$);

typically this was data within 500-1000 μm of a boundary

The resulting experimental data of this PIV analysis is plotted in Figure 5.1B, $v_x(y)$, as

open data points for a range of pump speeds. The velocity data can be integrated across the y-

axis to give rise to the volumetric fluxes, q, for each pump speed (i.e. red corresponds to 50%

pump speed or $q = 0.21$ mm/sec, orange is 60% pump speed or $q = 0.30$ mm/sec, green is 70%

pump speed or $q = 0.44$ mm/sec, teal is 80% pump speed or $q = 0.56$ mm/sec, blue is 90% pump

speed or $q = 0.66$ mm/sec, and violet is 100% pump speed or $q = 0.75$ mm/sec). Not surprisingly,

there is a direct linear relation between the pump seed and volumetric flux with $R^2=0.995$.

A quick inspection of the velocity profiles suggests that there is a slip boundary at the

glass/oil interface as well as the oil/part interface; this is based on the fact that simple extrapolation

of the data near the walls would not result in $v_x(y=0\text{mm}) \approx 0$mm/sec or $v_x(y=8.19\text{mm}) \approx 0$mm/sec.

Based upon this observation, an analytical model was applied assuming that the boundary

conditions would abide by the Navier slip above a critical slip yield stress and would be symmetric.

The Navier critical-stress slip boundary condition was applied to the planar Poiseuille flow

simplification of the Navier-Stokes equation. The derivation is included below for completeness.

The full Navier-Stokes equation for pressure-driven flow between two infinite plates (*i.e.*,

Poiseuille flow) spaced 2h apart can be simplified to:

$$\frac{d^2v_x}{dy^2} = \frac{-G}{\mu} \text{ , where } G \equiv \frac{-dP}{dx} \text{ is an unknown constant} \qquad \text{equation (\textit{i})}$$

The Navier critical-stress slip boundary condition can be described as:

$$v_x|_{y=\pm h} = \begin{cases} 0 & ; \tau|_{y=\pm h} \leq \tau_c \\ \frac{1}{\beta}\left((\tau|_{y=\pm h}) - \tau_c\right); & \tau|_{y=\pm h} > \tau_c \end{cases}$$

equation (*ii*)

where the velocity at the walls (*i.e.*, $v_x|_{y=\pm h}$) is zero and abides the non-slip boundary condition when the wall shear, $\tau|_{y=\pm h}$, is below a certain critical wall shear stress, τ_c. When above that critical shear stress, the velocity at the walls takes on a traditional Navier slip boundary condition where β is the slip coefficient (in this scenario we are assuming $\beta_{glass/oil} \approx \beta_{part/oil} \approx \beta$).

These equations can be made dimensionless by defining the following dimensionless variable groupings. Here, h is the distance from the center of the channel to the wall (i.e. the gap height is $2h$), and μ is the viscosity of the oil:

$$U(\acute{y}) = \frac{v_x \mu}{\tau_c h} \qquad\qquad \acute{G} = \frac{Gh}{\tau_c}$$

$$\acute{t} = \frac{\tau}{\tau_c} \qquad \acute{y} = \frac{y}{h} \qquad B = \frac{\mu}{\beta h}$$

The nondimensional versions of equation (*i*) and (*ii*) are:

$$\frac{d^2(U(\acute{y}))}{d\acute{y}^2} = -\acute{G}$$

equation (*iii*)

$$U|_{\acute{y}=\pm 1} = \begin{cases} 0 & ; \acute{G} \leq 1 \\ B(\acute{G} - 1) & ; \acute{G} > 1 \end{cases}$$

equation (*iv*)

Equation (*iii*) can be integrated twice to yield:

$$U(\acute{y}) = \frac{-\acute{G}\acute{y}^2}{2} + C_1\acute{y} + C_2$$

equation (*v*)

Equation (*iv*) can be used in conjunction with equation (*v*) to solve for C_1 and C_2 under the conditions where $\acute{G} \leq 1$ and $\acute{G} > 1$ to yield:

$$U(\acute{y}) = \begin{cases} \frac{\acute{G}}{2}(1 - \acute{y}^2) & ; \acute{G} \leq 1 \\ \frac{\acute{G}}{2}(1 + 2B - \acute{y}) - B & ; \acute{G} > 1 \end{cases}$$

equation (*vi*)

Equation (*vi*) can be brought back into dimensional space to yield:

$$v_x(y) = \begin{cases} \frac{G}{2\mu}(h^2 - y^2) & ; Gh \leq \tau_c \\ \frac{G}{2\mu}(h^2 - y^2) + \left(\frac{Gh}{\beta} - \tau_c h\right) & ; Gh > \tau_c \end{cases}$$

equation (*vii*)

In equation (*vii*), we find two fitting constants in the conditional statement, G and τ_c. For ease of fitting this discontinuous equation to the experimental dataset it is convenient to define a new grouping, $\alpha = \frac{\tau_c}{G}$, and to eliminate the unknown variable G so that this ratio can be the new fitting constant and used to decide the conditional statement alone (thus allowing for a potential solution to converge quicker during error minimization). This substitution yields:

$$
v_x^{fit}(y) = \begin{cases} \frac{\tau_c}{2\mu\alpha}(h^2 - y^2) & ; \ h \leq \alpha \\ \frac{\tau_c}{2\mu\alpha}(h^2 - y^2) + \left(\frac{\tau_c h}{\alpha\beta} - \tau_c h\right) & ; \ h > \alpha \end{cases}
$$

equation (*viii*)

Now we have an equation describing the lateral velocity as a function the *y*-axis position, $v_x(y)$, with a series of known constants, and unknown fitting constants. The known constants include the viscosity of the oil, μ=0.0722 g/(mm sec), and the height of the gap, 2*h*=8.19 mm. The unknown constants include the critical wall shear-stress at which slip begins to occur, τ_c with units g/(mm sec^2), the slip coefficient, β with units mm^{2}sec/g, and the ratio α with units of mm.

For our dataset, a series of $v_x(y)$ for varying pump speeds, both τ_c and β are global material constants while α is dependent upon G≡-dP/dx and thus the pump speed. In other words, τ_c and β are constant for all data series within the set, but α will change depending upon which data series we are fitting. For this reason, it's useful to redefine the dataset as $v_x(y,i)$ with fitting constants τ_c, β, and α_i where *i* represents the index of a specific data series (*i.e.*, pump speed is 50%, 60%, etc.) for a total of 8 fitting constants. For the five α fitting constants, there is the additional constraint that they must maintain a linear relationship with their corresponding pump speeds.

The total error between the model and dataset can be calculated as $e = \sum_i \sum_y [|v_x(y) - v_x^{fit}(y)|]$, where *i* is the index for each data series within the data set, and minimized as a function of the fitting constants τ_c, β, and α_i. This results in the fitting values converging to $\tau_c = 11\times10^{-6}$ g/(mm.sec^2), $\beta = 7.37\times10^{-2}$ mm^{2}sec/g, and α ranging from 6μm to 2μm for the range of pump speeds (50% to 100%). As expected, the linear relation between α and pump speed is maintained with R^2=0.995. The resultant model fit is represented by the solid lines within

Figure 5.1B of the main text. Lastly, as was qualitatively observed earlier, all experimental conditions appear to have slip-boundaries. This is confirmed given that all values of α are less than *h*=4.1mm. This can be further confirmed by forcing the model to accept the *non-slip* condition (*i.e.*, remove the conditional option during the fit analysis) and then, examining the goodness of fit. Obviously, from the plots in Figure 5.4 the non-slip condition is a substantially inferior model for understanding the dataset.

5.4. Thermal Imaging of Active Heat Dissipation

Central to HARP's high-volumetric throughput is its ability to actively dissipate the heat generated by the photo-polymerization reactions. The fluorinated oil, which constitutes the mobile interface, can be cooled or heated prior to entering the build area to regulate the temperature during the print process. Without this system, rapid vertical print speeds of even modestly sized parts quickly exceed the smoke point of the resin. These extreme temperature swings ($\Delta T \approx 120+ \, °C$) result in variable reactivities across the print-bed, thermal warping/cracking of the printed material, and uncontrolled clouding which limits lateral resolution; ultimately these factors result in a deformed object and failed print (Figure 5.6). HARP regulates the temperature of the build region by actively removing heat directly at the point of generation, rather than passively dissipating the heat into the resin vat and ambient surroundings. This enables the HARP print process to maintain its rapid vertical print speeds without the need to slow down to allow for the system to passively cool itself.

Figure 5.6. Impact of Thermal Control on Part Resolution and Clouding. On the left, a 3D printed part in which thermal control is lost near the base of the part (Figure 5.7A). This loss of control gives rise to 'clouding' and a loss of lateral resolution. On the right, the same 3D printed part with the added benefit of oil flow and cooling to dissipate heat (Figure 5.7C) results in thermal control being maintained and thus lateral resolution of the printed part being maintained. Scalebar is 1 inch.

To quantify this ability, thermal imaging of a small test print (2" x 2" cross-sectional area) was performed in a specialty designed miniature print vat (*i.e.*, low-profile walls to enable imaging across the bed). Three different flow scenarios were conducted: (*i*) printing without a mobile interface or active cooling (Figure 5.7A), (*ii*) printing with a mobile interface to actively dissipate heat, but with no cooling of the oil (Figure 5.7B), and (*iii*) printing with a mobile interface and actively cooling the oil (Figure 5.7C). As can be seen in Figure 5.7, without flow to actively dissipate heat the printed part quickly exceeds the sensor range of the infrared (IR) camera at 150 °C and exceeds the flash point of the resin's primary monomer diluent (1,6-hexanediol diacrylate,

113 °C). Similar experiments involving the generation of parts having larger cross-sectional areas (e.g., 8" x 8") exceed 180 °C (as evidenced by an IR non-contact thermometer gun measurement) in the absence of an active flow to dissipate the accumulating heat. In the case presented here, the accumulation of heat (Figure 5.7A) leads to surface temperatures in excess of 150 °C, and the part cracks during the printing process causing a physical displacement from the stage (observable in the final frame of Figure 5.7A, indicated by white lines overlaid upon the part; Figure 5.6). Alternatively, the flow of oil in Figure 5.7B acts to dissipate this heat into an oil reservoir; over time, this reservoir increases in temperature and loses its ability to effectively dissipate the heat of the reaction. Lastly, in Figure 5.7C the oil is actively cooled while flowing to help stabilize the reservoir temperature and surface temperature of the emerging part to 100-120°C. To further demonstrate the scalability of HARP through cooling, a 15" x 24" x 30" part was printed in 1 hour and 40 minutes (Figure 5.8). The average rate of heat generation during this print exceeds 200 W, with peak thermal outputs surpassing 3,600 W at thicker sections of the print. Typically, such heat generation rates would overwhelm a traditional printer relying upon passive heat dissipation, but with HARP this heat can be removed via a chilling unit (*e.g.*, ThermoFisher Scientific Merlin recirculating chiller) by way of the mobile oil interface and a heat exchanger. It is this combination of active heat dissipation acting in concert with the mobile liquid interface, previously described, which yields print speeds exceeding 430 mm/hr and record-breaking throughput (3.75 ft^3/hr).
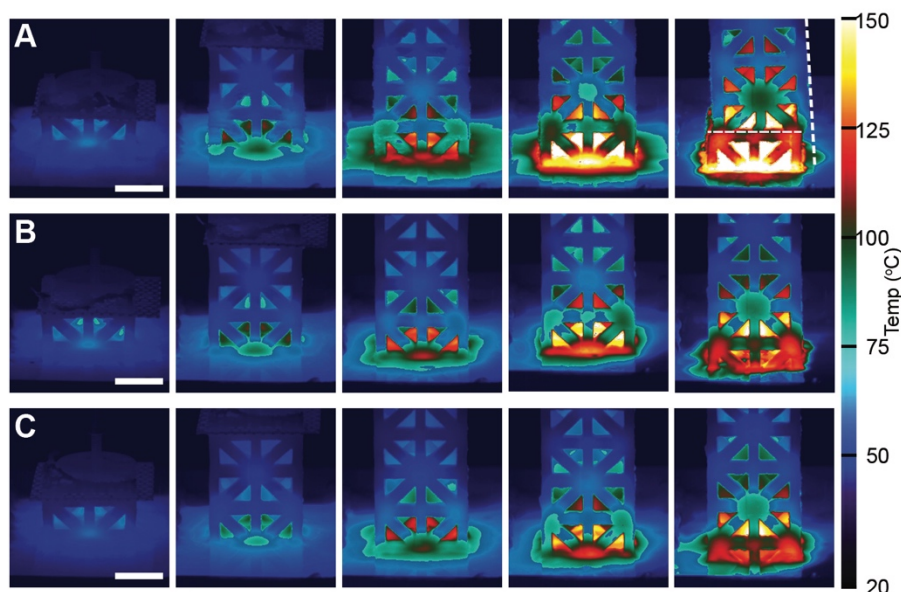
Figure 5.7. IR thermal images of an emerging 3D printed part (2" x 2" cross-section) under 3 different print conditions: (A) a stationary print interface, (B) a mobile interface, and (C) a mobile interface with active cooling. Time is advancing between the panels going from *left* to *right* at ~500 sec increments; scale bars are 1 inch.

Indeed, thermal control is the second critical component to the HARP printing mechanism and is one of the main advantages that allows the technology to reach an unprecedented throughput of 3.75 ft^3/hr (see Figure 5.8). One of the challenges in the SLA space is that when the polymer resin begins to overheat, 'clouding' occurs. Clouding is the polymerization of free-floating micro-particles. These particles are at a size domain (2-20 μm) where they are large enough to scatter light, thus losing control of the optical resolution of the system and of the printed object. As thermal control is lost, clouding becomes an even greater problem – the result is that the UV-projected cross-section begins to blur. This optical blurring results in a 'fuzzy' 3D printed part. An example of this can be seen in the parts which were printed during the thermal imaging experiment presented in Figure 5.7 of the main text. In Figure 5.6, the part on the left is an optical image of the part printed in Figure 5.7A. On the right is the part printed with flow and cooling

(corresponding to Figure 5.7C). At the base of the part (Figure 5.6, *left*) a loss of optical resolution clearly coincides with a loss of thermal control, as evidenced by how the crisp edges of the part beginning to fade as the print progressed. Additionally, the cracking and displacement mentioned can be clearly seen. For the part on the right in Figure 5.6, thermal control allows for the part edges to remain crisp throughout the entire print process.
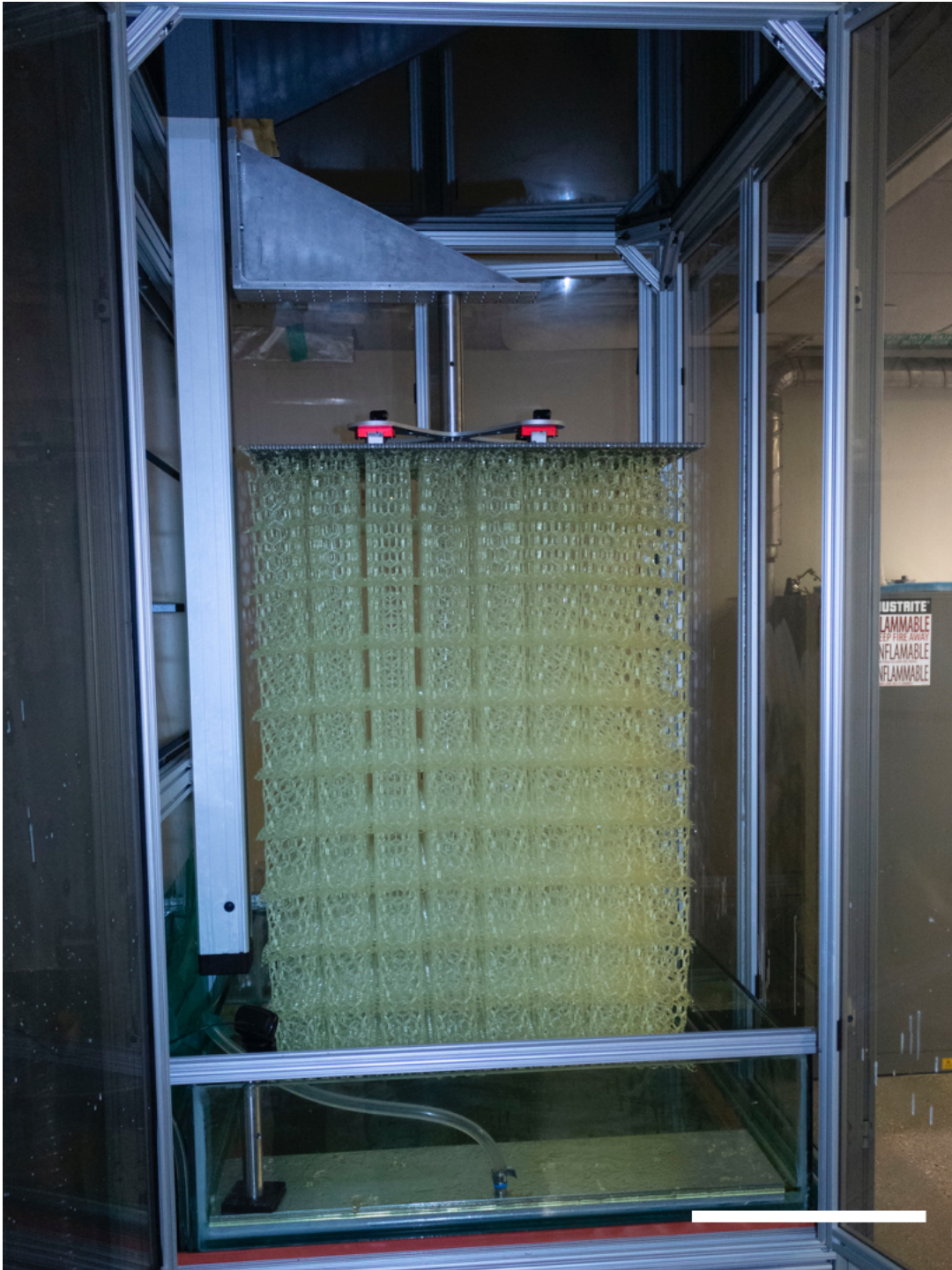
Figure 5.8. High Area Rapid Printing Embodied. 3D printed part within a HARP 3D printer with dimensions of 24" by 15" by 30" and a print time of 1 hr and 40 min. The design here is an extended version of the lattice structure presented in Figure 5.9F. Scale bar is 1 ft.

5.5. Expansive Library of Inks

HARP has extensive library of materials that can be printed. By not relying upon oxygen quenching, HARP is capable of printing both oxygen-sensitive and oxygen-insensitive resin chemistries. To demonstrate this ability, four different resins with varying properties were printed on the HARP 3D printer to generate four different classes of materials with varied properties: a hard polyurethane acrylate, an elastomeric polyurethane acrylate, an elastomeric butadiene rubber, and a silicon carbide ceramic (Figure 5.9). These resins are a mix of resins found in the literature, as well as one developed for the HARP printer.[196, 197] As with all SLA systems, each resin needs to be optimized in terms of initiators and quenchers to perform in conjunction with the light engine used and the desired vertical print rate out of the vat. The hard and elastomeric polyurethane resins printed optimally under vertical print speeds of 120 μm/sec. The ceramic resin is unique in that it utilizes thiolene-click chemistry, a chemistry known to be relatively oxygen-insensitive, to cross-link the polymeric resin and produce a 'green' part.[198, 199] As previously reported, this polymeric silicone can be post-treated in a furnace at 1000°C to undergo pyrolysis to eliminate the organic components and produce a silicon carbide structure.[196] Finally, the butadiene rubber resin required a slower print speed (30 μm/sec) owing to its lower reactivity and higher viscosity. While the post-processing and print conditions differed for each resin, all the resins were compatible with HARP. This makes HARP printing generally useful with stereolithographic resins currently available through literature or commercial formulations.[199, 200]To evaluate the properties of a part made via the HARP continuous print process, mechanical testing was performed on a Type 1 dog bone structure printed from an ABS-like urethane resin formulation. This was done using the protocols

of ASTM standard D638.[201] The results show that the HARP printed material maintains isotropic mechanical properties (Figure 5.10A) comparable to a molded part and unlike the structures made from layered 3D printing approaches, such as fused deposition modeling (FDM; Figure 5.10B, solid lines). The latter structures exhibit properties that are highly dependent on their print orientation. Remarkably, the HARP printed parts exhibit mechanical properties exceeding those of injection molded ABS plastic (Figure 5.10B, dashed vs solid black lines), one of the most ubiquitous materials used in the manufacturing of consumer goods. In addition, the HARP printed structures can be made with high print fidelity (Figure 5.10C-D) with a feature resolution as small as 300 μm (the theoretical optical resolution is 100 μm and is a function of the light patterning engine).

Taken together, these advances in throughput, interface design, heat management, and materials generality are poised to transform the way polymeric structures are prototyped and manufactured, regardless of intended use.
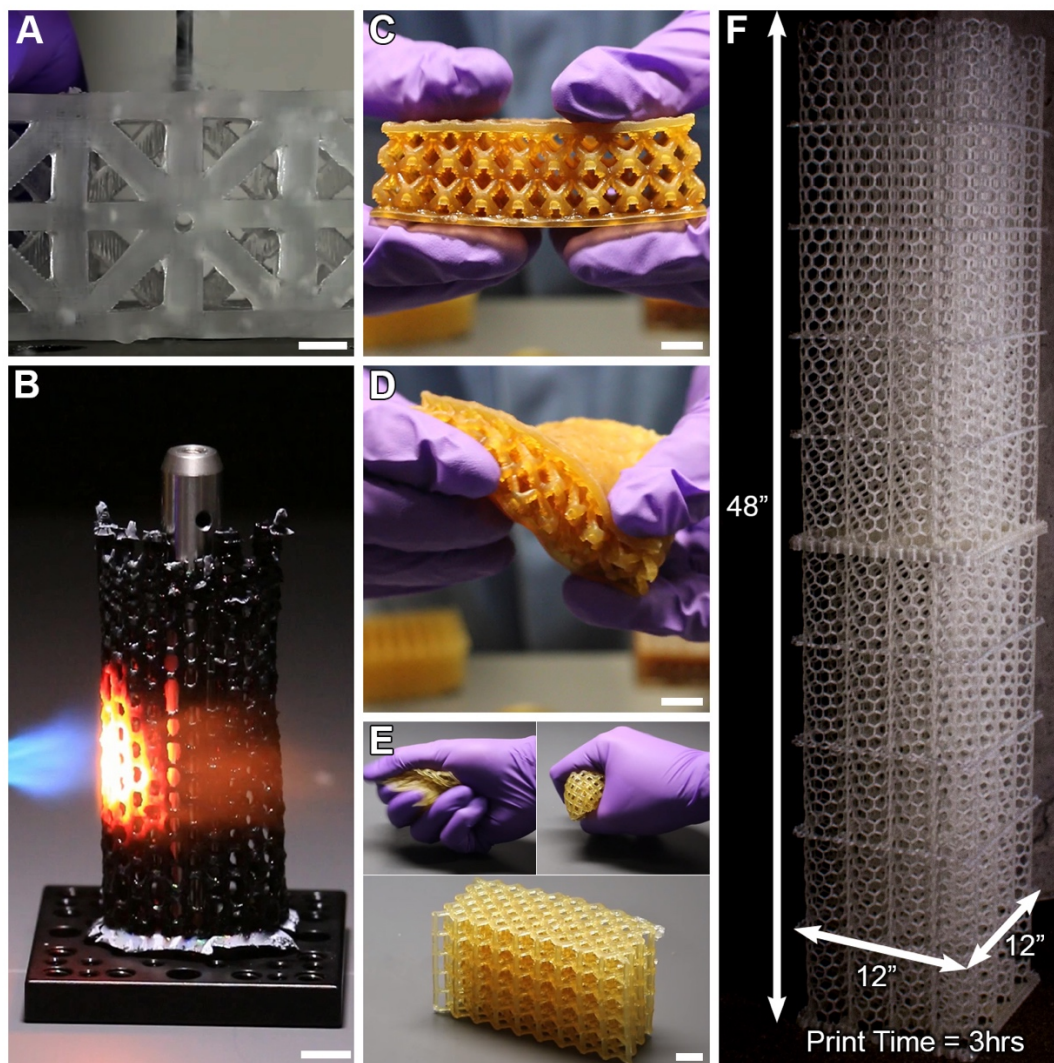
Figure 5.9. A wider palette of resins. (A) A hard, machinable polyurethane acrylate part (120 µm/sec print rate, 100 µm optical resolution) with a hole drilled against the print direction to demonstrate durability and isotropic properties, (B) a silicon carbide ceramic printed lattice (120 µm/sec print rate of green polymer precursor, 100 µm optical resolution) stands up to a propane torch (~2,000°C), (C, D, E) a printed butadiene rubber structure (C) a relaxed state and (D) under tension (30 µm/sec print rate, 100 µm optical resolution), (E) polybutadiene rubber returns to expanded lattice after compression (30 µm/sec print rate, 100 µm optical resolution), (F) a ~1.2 m tall hard polyurethane lattice printed in under 3 hours (120 µm/sec vertical print rate, 250 µm optical resolution). Scale bars in (A-E) are 1 cm.
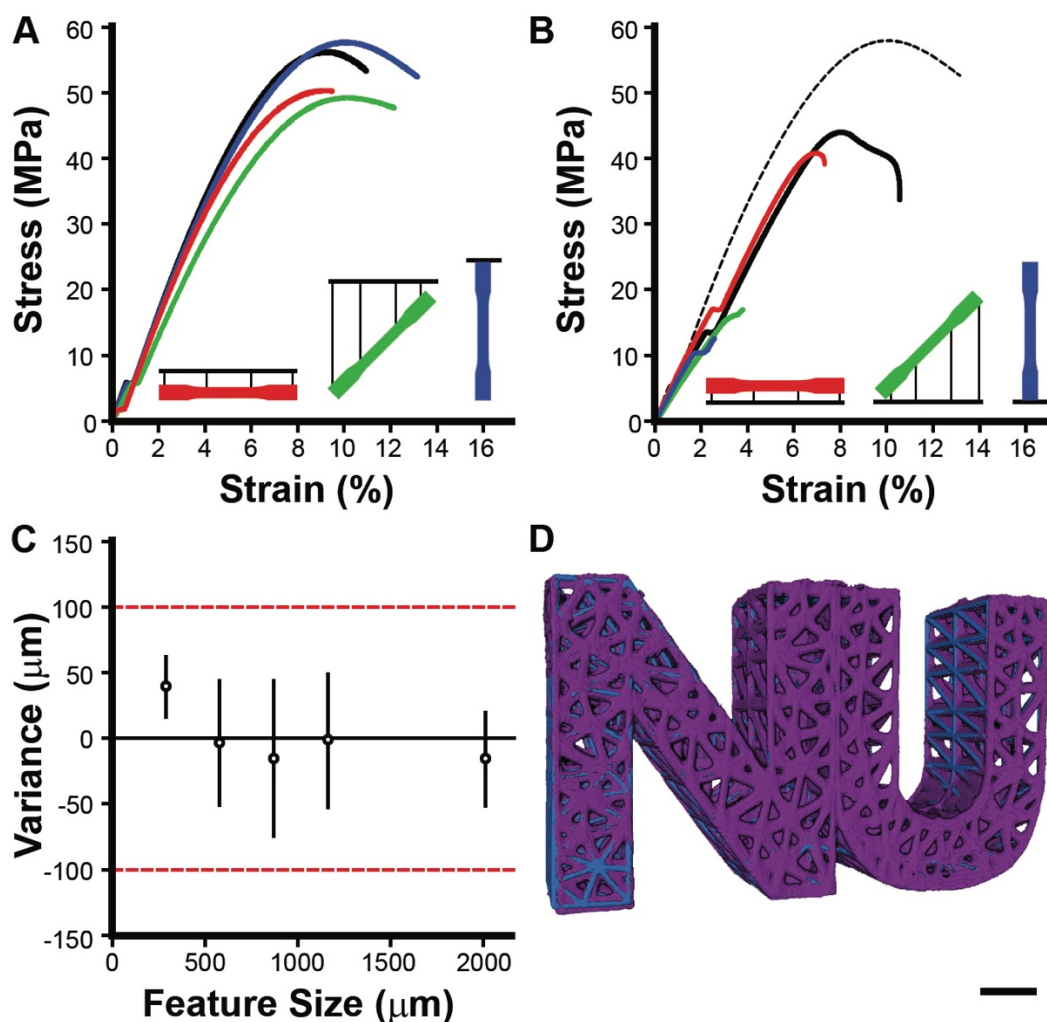
Figure 5.10. Manufacturing ready materials and resolution. (A) Type 1 dog bone structures made from an ABS-like polyurethane acrylate resin exhibit isotropic mechanical properties (ASTM D638) and are comparable to a part cast from the same resin (solid black line). (B) Fused deposition modeling with ABS yields parts with anisotropic and weaker mechanical properties (red, green, and blue lines) when compared to injection molded parts (solid black line; ASTM D638, Type 4 dog bones). For comparison, the vertically printed HARP part is shown (dashed black line, ASTM D638, Type 1 dog bone) and exceeds both the tensile strength and elongation of the injection molded ABS. HARP also enables high spatial resolution and print fidelity as evidenced by: (C) the variation between designed and printed features as a function of feature size down to a size of ~300 µm (below this, the ability to resolve parts becomes inconsistent) using a light-patterning engine with an optical resolution of 100 µm. Data points are mean values, and error bars represent the standard deviation across ten 5 mm tall posts printed in differing regions of the print-bed. Red lines represent the bounding constraints of ±1 pixel for the light patterning engine. (D) a CT (computed tomography) scan between a printed part and its CAD design file to reveal volumetric correlation. Scale bar is 1 cm.

5.6. Conclusions

With increasing adoption of 3D printing technologies in the manufacturing space, the need to increase the throughput of printers is critical to continuing this trend. Continuous SLA systems enable rapid vertical speeds and superior material properties, but they have not been able to scale-up due to the extensive heat generated by the polymerization reactions. HARP's mobile liquid interface solves this problem. The mobile interface allows for continuous printing, is self-regenerating, and can be used to actively dissipate heat during part production; this allows one to create printers with larger print beds (the limit has not been reached), achieve higher throughput, and expand the palette of printable resins. Taken together, these advances are poised to transform the way polymeric structures are prototyped and manufactured, regardless of intended use.

6. Chapter Six

Conclusions and Future Outlook

Lithography has been around for hundreds of years, and its influences are critical to our daily lives. From the fabrication of computer chips to photography to basic research, lithography is seemingly everywhere. Surprisingly with a field as old and prevalent as lithography, advances in this field are not uncommon. Over the past several decades, lithography has been expanding in two key areas: nanoscale resolution and going from 2D to 3D with stereolithography. As computers have grown more advanced, the need to create smaller and more complex devices has risen. This required moving down from the macro scale to the micro and then to the nanoscale. The boundary of lithography resolution has been pushed to what one can call its limits with the ability to manipulate single atoms. With these capabilities possible, the next stage is making these technologies accessible to a wider audience through new applications. The first necessary component of this was through increasing the throughput of the lithographic systems. In context of this Thesis for nanolithography, this was increasing polymer pen lithography patterning density with hard transparent arrays and increasing beam pen lithography for thousands to millions of pens with liquid mask etching. For stereolithography, it is getting the throughput to a point where production time rivals that of injection molding.

The field of nanocombinatorics outlined by the first three chapters of this Thesis layout the tools that have the potential to change the material landscape if properly used. The materials genome encompasses a massive parameter space that has been traditionally slow to go through and characterize. This space is further broadened when length scale becomes an additional parameter. To date, we have only discovered and developed a tiny fraction of all the possible structures and materials attainable through combinations of the 103 elements that define the Periodic Table on the nanoscale. Traditionally, most major advances have been derived from serial

approaches that involve trial and error, along with uncertainty. However, due to the precision that these materials require to be created, a systematic and quantitative approach is necessary. The development of nanocombinatorics, a field dedicated to systematic evaluation of nanomaterials, enables synthesis and characterization en masse to probe the vast landscape of potential compositions and geometries.

Ultimately, the discovery and development of the next generation nanomaterials will drive the global economy and will be dependent upon systematic, efficient, and controlled synthesis and characterization using nanocombinatorial approaches. One field in particular that this can impact is catalysis. Catalysis is a thriving industry with a current demand of $19.2 billion worldwide that was projected to increase to $24 billion by 2018.[202] Increasingly, metal nanoparticles are becoming an important part of the heterogeneous catalysis field due to their high activity and selectivity compared to their bulk counterparts.[203] Moreover, the high surface area to volume ratio reduces the total mass of precious metal needed. The need for efficient catalysts is not limited to a single industry as they are essential for pharmaceutical, manufacturing, and oil production. Catalysts are often only active over a narrow range of sizes and compositions making nanocombinatorics an attractive approach for their discovery and optimization. This new multimetallic synthesis platform not only has the potential to shape the field of catalysis, but also enhance diverse fields including photonics, plasmonics, magnetism, solar energy, biology, and nanomedicine. In order to make all of this possible, the next step relies on the development of characterization platforms. With the possibility of synthesizing more materials on a single chip 1 cm^2 than in the materials database, an equally powerful screening platform is necessary. If future researchers answer this call, then the field of nanocombinatorics will be very bright indeed.

Over the next couple of decades, additive manufacturing will start transitioning from a prototyping instrument to a manufacturing one. With the increased throughput that HARP offers, a door has been opened to use 3D printing over injection molding. HARP solves the problems currently limiting the 3D printing field. This new technique fabricates continuous parts at production speeds regardless of part size. Ultimately though, this just a stepping stone in a much bigger ecosystem. As the field of 3D printing advances further into manufacturing over the coming decades, there will not be a one be-all end-all technique that solves every need. Each product that is manufactured needs custom parts. As printers such as HARP are developed and used, the next component is to create a library of materials. This is an area that is only just starting to begin to develop. As 3D printing becomes a larger component of the manufacturing sector, chemical pipelines will start making resins. This will drop the material prices down and further push 3D printing's reach. This will be part of the pathway forward that will enable 3D printing to shape the future.

This Thesis has outlined the development and applications of new tools in the field of lithography through the bridging of length scales. When properly used, these tools can help to bring about a greater understanding of fundamental studies as well as be applied to industrial applications. Through the developments of the fields of manufacturing with stereolithography and nanocombinatorics, new industries and sectors will rise and give the possibility of a greener future.

This greener future will be possible with more efficient catalysts discovered by megalibraries as well as by moving manufacturing from injection molding to additive manufacturing. By creating better catalysts, byproducts in chemical reactions can be minimized and potentially reducing the number of steps. This ultimately reduces both waste and energy

require at the chemical plant. With additive manufacturing, fabricating components is a mold free process. By removing the need for mold fabrications, a large reduction in material consumption is possible. Furthermore, with the ability to print on demand, warehouses of inventory are no longer needed. Thus, it removes the need to store parts for decades in warehouses. All of these things hold the potential to substantially impact society for the better.

References

References

1.   Moore, G. E. In *Lithography and the future of Moore's law*, SPIE's 1995 Symposium on Microlithography, International Society for Optics and Photonics: 1995; pp 2-17.

2.   Lundstrom, M., Moore's law forever? *Science* **2003,** *299* (5604), 210.

3.   Isaacoff, B. P.; Brown, K. A., Progress in Top-Down Control of Bottom-Up Assembly. *Nano Lett.* **2017,** *17* (11), 6508–6510.

4.   Waldrop, M. M., The chips are down for Moore's law. *Nature* **2016,** *530*, 144–147.

5.   Astruc, D.; Lu, F.; Aranzaes, J. R., Nanoparticles as Recyclable Catalysts: The Frontier between Homogeneous and Heterogeneous Catalysis. *Angew. Chem. Int. Ed.* **2005,** *44* (48), 7852-7872.

6.   Bettinger, C. J.; Langer, R.; Borenstein, J. T., Engineering Substrate Topography at the Micro- and Nanoscale to Control Cell Function. *Angew. Chem. Int. Ed.* **2009,** *48* (30), 5406-5415.

7.   Giam, L. R.; Massich, M. D.; Hao, L.; Shin Wong, L.; Mader, C. C.; Mirkin, C. A., Scanning probe-enabled nanocombinatorics define the relationship between fibronectin feature size and stem cell fate. *Proceedings of the National Academy of Sciences* **2012,** *109* (12), 4377.

8.   Bell, A. T., The Impact of Nanoscience on Heterogeneous Catalysis. *Science* **2003,** *299* (5613), 1688-1691.

9.   Khademhosseini, A.; Langer, R.; Borenstein, J.; Vacanti, J. P., Microscale technologies for tissue engineering and biology. *Proc. Natl. Acad. Sci. USA* **2006,** *103* (8), 2480-7.

10.   Lopez, G. P.; Albers, M. W.; Schreiber, S. L.; Carroll, R.; Peralta, E.; Whitesides, G. M., Convenient methods for patterning the adhesion of mammalian cells to surfaces using self-assembled monolayers of alkanethiolates on gold. *J. Am. Chem. Soc.* **1993,** *115* (13), 5877-5878.

11.   Kane, R. S.; Takayama, S.; Ostuni, E.; Ingber, D. E.; Whitesides, G. M., Patterning proteins and cells using soft lithography. *Biomaterials* **1999,** *20* (23–24), 2363-2376.

12.   Wilbur, J. L.; Kumar, A.; Kim, E.; Whitesides, G. M., Microfabrication by microcontact printing of self-assembled monolayers. *Adv. Mater.* **1994,** *6* (7-8), 600-604.

13.   Wilbur, J. L.; Kim, E.; Xia, Y.; Whitesides, G. M., Lithographic molding: A convenient route to structures with sub-micrometer dimensions**. *Adv. Mater.* **1995,** *7* (7), 649-652.

14.   Jung Moo, H.; Fatih, M. O.; Jun, Z., A micromachined elastomeric tip array for contact printing with variable dot size and density. *J. Micromech. Microeng.* **2008,** *18* (1), 015003.

15.   Huo, F.; Zheng, Z.; Zheng, G.; Giam, L. R.; Zhang, H.; Mirkin, C. A., Polymer Pen Lithography. *Science* **2008,** *321* (5896), 1658-1660.

16.   Mirkin, C. A., The Power of the Pen: Development of Massively Parallel Dip-Pen Nanolithography. *ACS Nano* **2007,** *1*, 79.

17.   Bullen, D.; Chung, S. W.; Wang, X.; Zou, J.; Mirkin, C. A.; Liu, C., Parallel Dip-Pen Nanolithography with Arrays of Individually Addressable Cantilevers. *Appl. Phys. Lett.* **2004,** *84*, 789.

18.   Salaita, K.; Lee, S. W.; Wang, X.; Huang, L.; Dellinger, T. M.; Liu, C.; Mirkin, C. A., Sub-100 Nm, Centimeter-Scale, Parallel Dip-Pen Nanolithography. *Small* **2005,** *1*, 940.

19.   Braunschweig, A. B.; Huo, F.; Mirkin, C. A., Molecular printing. *Nature Chem.* **2009,** *1* (5), 353-358.

20.   Giam, L. R.; Mirkin, C. A., Cantilever-Free Scanning Probe Molecular Printing. *Angew. Chem. Int. Ed.* **2011,** *50* (33), 7482-7485.

21.   Giam, L. R.; Senesi, A. J.; Liao, X.; Wong, L. S.; Chai, J.; Eichelsdoerfer, D. J.; Shim, W.; Rasin, B.; He, S.; Mirkin, C. A. In *Direct-write scanning probe lithography: towards a desktop fab*, Proc. SPIE 8031, Micro- and Nanotechnology Sensors, Systems, and Applications III, Orlando, Florida, USA, George, T.; Islam, M. S.; Dutta, A. K., Eds. SPIE: Orlando, Florida, USA, 2011; pp 803103-7.

22.   Urtizberea, A.; Hirtz, M.; Fuchs, H., Ink transport modelling in Dip-Pen Nanolithography and Polymer Pen Lithography. In *Nanofabrication*, 2016; Vol. 2.

23.   Brown, K. A.; Eichelsdoerfer, D. J.; Liao, X.; He, S.; Mirkin, C. A., Material Transport in Dip-Pen Nanolithography. *Front. Phys.* **2014,** *9*, 385.

24.   He, Q.; Tan, C.; Zhang, H., Recent Advances in Cantilever-Free Scanning Probe Lithography: High-Throughput, Space-Confined Synthesis of Nanostructures and Beyond. *ACS Nano* **2017,** *11* (5), 4381-4386.

25.   Liao, X.; Braunschweig, A. B.; Zheng, Z.; Mirkin, C. A., Force- and Time-Dependent Feature Size and Shape Control in Molecular Printing Via Polymer-Pen Lithography. *Small* **2010,** *6*, 1082.

26.   Eichelsdoerfer, D. J.; Brown, K. A.; Wang, M. X.; Mirkin, C. A., Role of Absorbed Solvent in Polymer Pen Lithography. *J. Phys. Chem. B* **2013,** *117*, 16363.

27.   Chai, J.; Huo, F.; Zheng, Z.; Giam, L. R.; Shim, W.; Mirkin, C. A., Scanning Probe Block Copolymer Lithography. *Proc. Natl. Acad. Sci. U. S. A.* **2010,** *107*, 20202.

28.   Demers, L. M.; Mirkin, C. A., Combinatorial Templates Generated by Dip-Pen Nanolithography for the Formation of Two-Dimensional Particle Arrays. *Angew. Chem.* **2001,** *113*, 3159.

29.   Vega, R. A.; Maspoch, D.; Salaita, K.; Mirkin, C. A., Nanoarrays of Single Virus Particles. *Angew. Chem.* **2005,** *117*, 6167.

30.   Liu, X.; Guo, S.; Mirkin, C. A., Surface and Site-Specific Ring-Opening Metathesis Polymerization Initiated by Dip-Pen Nanolithography. *Angew. Chem.* **2003,** *115*, 4933.

31.   Zhang, H.; Li, Z.; Mirkin, C. A., Dip-Pen Nanolithography-Based Methodology for Preparing Arrays of Nanostructures Functionalized with Oligonucleotides. *Adv. Mater.* **2002,** *14*, 1472.

32.   Fu, L.; Liu, X.; Zhang, Y.; Dravid, V. P.; Mirkin, C. A., Nanopatterning of "Hard" Magnetic Nanostructures Via Dip-Pen Nanolithography and a Sol-Based Ink. *Nano Lett.* **2003,** *3*, 757.

33.   Nam, J. M.; Han, S. W.; Lee, K. B.; Liu, X.; Ratner, M. A.; Mirkin, C. A., Bioactive Protein Nanoarrays on Nickel Oxide Surfaces Formed by Dip-Pen Nanolithography. *Angew. Chem.* **2004,** *116*, 1266.

34.   Farmakidis, N.; Brown, K. A., Quantifying Liquid Transport and Patterning Using Atomic Force Microscopy. *Langmuir* **2017,** *33*, 5173.

35.   Eichelsdoerfer, D. J.; Brown, K. A.; Mirkin, C. A., Capillary Bridge Rupture in Dip-Pen Nanolithography. *Soft Matter* **2014,** *10*, 5603.

36.   Sheehan, P. E.; Whitman, L. J.; King, W. P.; Nelson, B. A., Nanoscale Deposition of Solid Inks Via Thermal Dip Pen Nanolithography. *Appl. Phys. Lett.* **2004,** *85*, 1589.

37.   Yang, M.; Sheehan, P. E.; King, W. P.; Whitman, L. J., Direct Writing of a Conducting Polymer with Molecular-Level Control of Physical Dimensions and Orientation. *J. Am. Chem. Soc.* **2006,** *128*, 6774.

38.   Piner, R. D.; Zhu, J.; Xu, F.; Hong, S.; Mirkin, C. A., Dip-Pen″ Nanolithography. *Science* **1999,** *283*, 661.

39.   Eichelsdoerfer, D. J.; Liao, X.; Cabezas, M. D.; Morris, W.; Radha, B.; Brown, K. A.; Giam, L. R.; Braunschweig, A. B.; Mirkin, C. A., Large-area molecular patterning with polymer pen lithography. *Nat. Protoc.* **2013,** *8* (12), 2548-2560.

40.   Dong-Jin, L.; Kwang, H.; Hyungwoo, L.; Hochan, C.; Byung Yang, L., Selective adsorption of metal nanowires on molecularly patterned substrates using surface-to-volume ratio-dependent strategies. *Applied Physics Express* **2014,** *7* (11), 115001.

41.   Ma, X.; Li, F.; Xie, Z.; Xue, M.; Zheng, Z.; Zhang, X., Size-tunable, highly sensitive microelectrode arrays enabled by polymer pen lithography. *Soft Matter* **2017,** *13* (20), 3685-3689.

42.   Bog, U.; de los Santos Pereira, A.; Mueller, S. L.; Havenridge, S.; Parrillo, V.; Bruns, M.; Holmes, A. E.; Rodriguez-Emmenegger, C.; Fuchs, H.; Hirtz, M., Clickable Antifouling Polymer Brushes for Polymer Pen Lithography. *ACS Appl. Mater. Interfaces* **2017**.

43.   Huang, L.; Braunschweig, A. B.; Shim, W.; Qin, L.; Lim, J. K.; Hurst, S. J.; Huo, F.; Xue, C.; Jang, J.-W.; Mirkin, C. A., Matrix-Assisted Dip-Pen Nanolithography and Polymer Pen Lithography. *Small* **2010,** *6* (10), 1077–1081.

44.   Wu, J.; Zan, X.; Li, S.; Liu, Y.; Cui, C.; Zou, B.; Zhang, W.; Xu, H.; Duan, H.; Tian, D.; Huang, W.; Huo, F., In situ synthesis of large-area single sub-10 nm nanoparticle arrays by polymer pen lithography. *Nanoscale* **2014**.

45.   Biswas, S.; Brinkmann, F.; Hirtz, M.; Fuchs, H., Patterning of Quantum Dots by Dip-Pen and Polymer Pen Nanolithography. *Nanofabrication* **2015,** *2* (1), 19-26.

46.   Liu, G.; Eichelsdoerfer, D. J.; Rasin, B.; Zhou, Y.; Brown, K. A.; Liao, X.; Mirkin, C. A., Delineating the Pathways for the Site-Directed Synthesis of Individual Nanoparticles on Surfaces. *Proc. Natl. Acad. Sci. U. S. A.* **2013,** *110*, 887.

47.   Bian, S.; Schesing, K. B.; Braunschweig, A. B., Matrix-assisted polymer pen lithography induced Staudinger Ligation. *Chem. Commun.* **2012,** *48* (41), 4995-4997.

48.   Jang, J.; Hong, S.; Schatz, G. C.; Ratner, M. A., Self-assembly of ink molecules in dip-pen nanolithography: A diffusion model. *J. Chem. Phys.* **2001,** *115* (6), 2721–2729.

49.   Liu, G.; Zhou, Y.; Banga, R. S.; Boya, R.; Brown, K. A.; Chipre, A. J.; Nguyen, S. T.; Mirkin, C. A., The role of viscosity on polymer ink transport in dip-pen nanolithography. *Chem. Sci.* **2013,** *4* (5), 2093–2099.

50.   Eichelsdoerfer, D. J.; Brown, K. A.; Mirkin, C. A., Capillary bridge rupture in dip-pen nanolithography. *Soft Matter* **2014,** *10*, 5603–5608.

51.   Liao, X.; Braunschweig, A. B.; Zheng, Z.; Mirkin, C. A., Force- and Time-Dependent Feature Size and Shape Control in Molecular Printing via Polymer-Pen Lithography. *Small* **2010,** *6* (10), 1082-1086.

52.   Shuangping, L.; Monica, O. d. l. C., Deformation of elastomeric pyramid pen arrays in cantilever-free scanning probe lithography. *Journal of Polymer Science Part B: Polymer Physics* **2018,** *56* (9), 731-738.

53.   Han, X.; Bian, S.; Liang, Y.; Houk, K. N.; Braunschweig, A. B., Reactions in Elastomeric Nanoreactors Reveal the Role of Force on the Kinetics of the Huisgen Reaction on Surfaces. *J. Am. Chem. Soc.* **2014**.

54.   Bian, S.; Scott, A. M.; Cao, Y.; Liang, Y.; Osuna, S.; Houk, K. N.; Braunschweig, A. B., Covalently Patterned Graphene Surfaces by a Force-Accelerated Diels–Alder Reaction. *J. Am. Chem. Soc.* **2013**, *135* (25), 9240-9243.

55.   Liao, X.; Braunschweig, A. B.; Mirkin, C. A., "Force-Feedback" Leveling of Massively Parallel Arrays in Polymer Pen Lithography. *Nano Lett.* **2010**, *10* (4), 1335-1340.

56.   Noh, H.; Jung, G.-E.; Kim, S.; Yun, S.-H.; Jo, A.; Kahng, S.-J.; Cho, N.-J.; Cho, S.-J., "Multipoint Force Feedback" Leveling of Massively Parallel Tip Arrays in Scanning Probe Lithography. *Small* **2015**, n/a-n/a.

57.   Wang, S.; Hosford, J.; Heath, W. P.; Wong, L. S., Large-area scanning probe nanolithography facilitated by automated alignment of probe arrays. *RSC Advances* **2015**, *5* (75), 61402-61409.

58.   Kumar, R.; Urtizberea, A.; Ghosh, S.; Bog, U.; Rainer, Q.; Lenhert, S.; Fuchs, H.; Hirtz, M., Polymer Pen Lithography with Lipids for Large-Area Gradient Patterns. *Langmuir* **2017**, *33* (35), 8739-8748.

59.   Hong, J. W.; Studer, V.; Hang, G.; Anderson, W. F.; Quake, S. R., A nanoliter-scale nucleic acid processor with parallel architecture. *Nat. Biotechnol.* **2004**, *22* (4), 435-9.

60.   Squires, T. M.; Quake, S. R., Microfluidics: Fluid physics at the nanoliter scale. *Rev. Mod. Phys.* **2005**, *77*, 50.

61.   Han, Y.; Liu, C., Pneumatically actuated active polymer pen lithography. *Sens. Actuators A* **2011**, *167*, 433–437.

62.   Li, S.; Dellinger, T. M.; Wang, Q.; Szegedi, S.; Liu, C., Pneumatically actuated elastomeric device for nanoscale surface patterning. *Appl. Phys. Lett.* **2007**, *91* (2), 023109-3.

63.   Brown, K. A.; Eichelsdoerfer, D. J.; Mirkin, C. A., Cantilever-free thermal actuation. *J. Vac. Sci. Technol., B* **2013**, *31* (6), 06F201-5.

64.   Brown, K. A.; Eichelsdoerfer, D. J.; Shim, W.; Rasin, B.; Radha, B.; Liao, X.; Schmucker, A. L.; Liu, G.; Mirkin, C. A., A cantilever-free approach to dot-matrix nanoprinting. *Proc. Natl. Acad. Sci. USA* **2013**, *110* (32), 12921-12924.

65.   Sarov, Y.; Ivanov, T.; Frank, A.; Rangelow, I. W., Thermally driven multi-layer actuator for 2D cantilever arrays. *Appl. Phys. A* **2011**, *102* (1), 61-68.

66.   Lalinský, T.; Burian, E.; Drzík, M.; Hascík, S.; Mozolová, Z.; Kuzmík, J., Thermal actuation of a GaAs cantilever beam. *J. Micromech. Microeng.* **2000**, *10* (2), 293.

67.   Huang, Z.; Li, L.; Zhang, X. A.; Alsharif, N.; Wu, X.; Peng, Z.; Cheng, X.; Wang, P.; Brown, K. A.; Wang, Y., Photoactuated Pens for Molecular Printing. *Adv. Mater.* **2017**, *30* (8), 1705303.

68.   Brown, K. A.; Eichelsdoerfer, D. J.; Shim, W.; Rasin, B.; Radha, B.; Liao, X.; Schmucker, A. L.; Liu, G.; Mirkin, C. A., A Cantilever-Free Approach to Dot-Matrix Nanoprinting. *Proc. Natl. Acad. Sci. U. S. A.* **2013**, *110*, 12921.

69.   Kluender, E. J.; Hedrick, J. L.; Brown, K. A.; Rao, R.; Meckes, B.; Du, J. S.; Moreau, L. M.; Maruyama, B.; Mirkin, C. A., Catalyst discovery through megalibraries of nanomaterials. *Proceedings of the National Academy of Sciences* **2019**, *116* (1), 40.

70.   Zheng, Z.; Daniel, W. L.; Giam, L. R.; Huo, F.; Senesi, A. J.; Zheng, G.; Mirkin, C. A., Multiplexed Protein Arrays Enabled by Polymer Pen Lithography: Addressing the Inking Challenge. *Angew. Chem.* **2009,** *121*, 7762.

71.   Zheng, Z.; Daniel, W. L.; Giam, L. R.; Huo, F.; Senesi, A. J.; Zheng, G.; Mirkin, C. A., Multiplexed Protein Arrays Enabled by Polymer Pen Lithography: Addressing the Inking Challenge. *Angew. Chem.* **2009,** *121* (41), 7762-7765.

72.   Arrabito, G.; Schroeder, H.; Schröder, K.; Filips, C.; Marggraf, U.; Dopp, C.; Venkatachalapathy, M.; Dehmelt, L.; Bastiaens, P. I. H.; Neyer, A.; Niemeyer, C. M., Configurable Low-Cost Plotter Device for Fabrication of Multi-Color Sub-Cellular Scale Microarrays. *Small* **2014,** *10*, 2870.

73.   Bog, U.; Brinkmann, F.; Kalt, H.; Koos, C.; Mappes, T.; Hirtz, M.; Fuchs, H.; Köber, S., Large-Scale Parallel Surface Functionalization of Goblet-Type Whispering Gallery Mode Microcavity Arrays for Biosensing Applications. *Small* **2014,** *10*, 3863.

74.   Brinkmann, F.; Hirtz, M.; Greiner, A. M.; Weschenfelder, M.; Waterkotte, B.; Bastmeyer, M.; Fuchs, H., Interdigitated Multicolored Bioink Micropatterns by Multiplexed Polymer Pen Lithography. *Small* **2013**, n/a-n/a.

75.   Kumar, R.; Weigel, S.; Meyer, R.; Niemeyer, C. M.; Fuchs, H.; Hirtz, M., Multi-color polymer pen lithography for oligonucleotide arrays. *Chem. Commun.* **2016,** *52* (83), 12310-12313.

76.   Bog, U.; Brinkmann, F.; Kalt, H.; Koos, C.; Mappes, T.; Hirtz, M.; Fuchs, H.; Köber, S., Large-Scale Parallel Surface Functionalization of Goblet-type Whispering Gallery Mode Microcavity Arrays for Biosensing Applications. *Small* **2014,** *10* (19), 3863-3868.

77.   Agusil, J. P.; Torras, N.; Duch, M.; Esteve, J.; Pérez-García, L.; Samitier, J.; Plaza, J. A., Highly Anisotropic Suspended Planar-Array Chips with Multidimensional Sub-Micrometric Biomolecular Patterns. *Adv. Funct. Mater.* **2017**, 1605912-n/a.

78.   Eichelsdoerfer, D. J.; Brown, K. A.; Wang, M. X.; Mirkin, C. A., Role of Absorbed Solvent in Polymer Pen Lithography. *J. Phys. Chem. B* **2013,** *117*, 16363–16368.

79.   Zhong, X.; Bailey, N. A.; Schesing, K. B.; Bian, S.; Campos, L. M.; Braunschweig, A. B., Materials for the preparation of polymer pen lithography tip arrays and a comparison of their printing properties. *Journal of Polymer Science Part A: Polymer Chemistry* **2013,** *51* (7), 1533-1539.

80.   Xie, Z.; Shen, Y.; Zhou, X.; Yang, Y.; Tang, Q.; Miao, Q.; Su, J.; Wu, H.; Zheng, Z., Polymer Pen Lithography Using Dual-Elastomer Tip Arrays. *Small* **2012,** *8* (17), 2664–2669.

81.   Wu, J.; Miao, J. M., Production of Centimeter-Scale Gradient Patterns by Graded Elastomeric Tip Array. *ACS Appl. Mater. Interfaces* **2015**.

82.   Xue, M.; Cai, X.; Chen, G., Colloidal Pen Lithography. *Small* **2014**, n/a-n/a.

83.   Shim, W.; Brown, K. A.; Zhou, X.; Rasin, B.; Liao, X.; Mirkin, C. A., Multifunctional cantilever-free scanning probe arrays coated with multilayer graphene. *Proc. Natl. Acad. Sci. USA* **2012,** *109* (45), 18312-18317.

84.   Mao, Z.; Ganesh, M.; Bucaro, M.; Smolianski, I.; Gross, R. A.; Lyons, A. M., High Throughput, High Resolution Enzymatic Lithography Process: Effect of Crystallite Size, Moisture, and Enzyme Concentration. *Biomacromolecules* **2014**.

85.   Shim, W.; Braunschweig, A. B.; Liao, X.; Chai, J.; Lim, J. K.; Zheng, G.; Mirkin, C. A., Hard-Tip, Soft-Spring Lithography. *Nature* **2011,** *469*, 516.

86.   Huo, F.; Zheng, G.; Liao, X.; Giam, L. R.; Chai, J.; Chen, X.; Shim, W.; Mirkin, C. A., Beam Pen Lithography. *Nat. Nanotechnol.* **2010,** *5*, 637.

87.   Shim, W.; Braunschweig, A. B.; Liao, X.; Chai, J.; Lim, J. K.; Zheng, G.; Mirkin, C. A., Hard-tip, soft-spring lithography. *Nature* **2011,** *469* (7331), 516-520.

88.   Eichelsdoerfer, D. J.; Brown, K. A.; Boya, R.; Shim, W.; Mirkin, C. A., Tuning the Spring Constant of Cantilever-Free Tip Arrays. *Nano Lett.* **2013,** *13* (2), 664–667.

89.   Rabe, U.; Janser, K.; Arnold, W., Vibrations of free and surface-coupled atomic force microscope cantilevers: Theory and experiment. *Rev. Sci. Instrum.* **1996,** *67*, 3281–3293.

90.   Hedrick, J. L.; Brown, K. A.; Kluender, E. J.; Cabezas, M. D.; Chen, P.-C.; Mirkin, C. A., Hard Transparent Arrays for Polymer Pen Lithography. *ACS Nano* **2016,** *10* (3), 3144-3148.

91.   Gates, B. D.; Xu, Q.; Stewart, M.; Ryan, D.; Willson, C. G.; Whitesides, G. M., New Approaches to Nanofabrication: Molding, Printing, and Other Techniques. *Chemical Reviews* **2005,** *105* (4), 1171-1196.

92.   Qin, D.; Xia, Y.; Black, A. J.; Whitesides, G. M., Photolithography with transparent reflective photomasks. *J. Vac. Sci. Technol., B* **1998,** *16* (1), 98-103.

93.   Qin, D.; Xia, Y.; Whitesides, G. M., Elastomeric light valves. *Adv. Mater.* **1997,** *9* (5), 407-410.

94.   Zhou, Y.; Xie, Z.; Brown, K. A.; Park, D. J.; Zhou, X.; Chen, P.-C.; Hirtz, M.; Lin, Q.-Y.; Dravid, V. P.; Schatz, G. C.; Zheng, Z.; Mirkin, C. A., Apertureless Cantilever-Free Pen Arrays for Scanning Photochemical Printing. *Small* **2014,** *11* (8), 913–918.

95.   Huo, F.; Zheng, G.; Liao, X.; Giam, L. R.; Chai, J.; Chen, X.; Shim, W.; Mirkin, C. A., Beam Pen Lithography. *Nature Nanotech.* **2010,** *5*, 637-640.

96.   Liao, X.; Brown, K. A.; Schmucker, A. L.; Liu, G.; He, S.; Shim, W.; Mirkin, C. A., Desktop nanofabrication with massively multiplexed beam pen lithography. *Nat. Commun.* **2013,** *4*, 2103

97.   Liao, X.; Huang, Y.-k.; Mirkin, C. A.; Dravid, V. P., High Throughput Synthesis of Multifunctional Oxide Nanostructures within Nanoreactors Defined by Beam Pen Lithography. *ACS Nano* **2017**.

98.   Huan, H.; Junghoon, Y.; Glennys, M.; Yaofeng, C.; Mark, A. S.; William, P. K., Nano-fabrication with a flexible array of nano-apertures. *Nanotechnology* **2012,** *23* (17), 175303.

99.   Yuan-Jen, C.; Han-Kuan, H. In *Nano-scale tip fabricated by electro-chemical machining for nano lithography*, Nano/Micro Engineered and Molecular Systems (NEMS), 2014 9th IEEE International Conference on, 13-16 April 2014; 2014; pp 126-129.

100.   Chang, Y.-J.; Liao, J.-M., Fabrication of sub-100 nm h-PDMS tip array for tip-based nanolithography by electrochemical machining. *Microsystem Technologies* **2016**, 1-6.

101.   Wu, C.-Y.; Lee, Y.-C., Apertureless beam pen lithography based on fully metal-coated polyurethane-acrylate (PUA) pyramidal microstructure array. *Optics Express* **2014,** *22* (9), 10593-10604.

102.   Huo, F., Parallel Near-field Photolithography with Metal-coated Elastomeric Masks. *Langmuir* **2014**.

103.   Yuan-Jen, C.; Han-Kuan, H., Parallel multi-step nanolithography by nanoscale Cu-covered h-PDMS tip array. *J. Micromech. Microeng.* **2014,** *24* (9), 095022.

104.   Xie, Z.; Gordiichuk, P.; Lin, Q.-Y.; Meckes, B.; Chen, P.-C.; Sun, L.; Du, J. S.; Zhu, J.; Liu, Y.; Dravid, V. P.; Mirkin, C. A., Solution-Phase Photochemical Nanopatterning Enabled by High-Refractive-Index Beam Pen Arrays. *ACS Nano* **2017**.

105.   Yu-Zen, C.; Chun-Ying, W.; Yung-Chun, L., Beam pen lithography based on arrayed polydimethylsiloxane (PDMS) micro-pyramids spin-coated with carbon black photo-resist. *J. Micromech. Microeng.* **2014,** *24* (4), 045007.

106.   He, S.; Xie, Z.; Park, D. J.; Liao, X.; Brown, K. A.; Chen, P.-C.; Zhou, Y.; Schatz, G. C.; Mirkin, C. A., Liquid-Phase Beam Pen Lithography. *Small* **2016,** *12* (8), 988-993.

107.   French, R. H.; Tran, H. V., Immersion Lithography: Photomask and Wafer-Level Materials. *Annu. Rev. Mater. Res.* **2009,** *39* (1), 93-126.

108.   Liu, X.; Zheng, Y.; Peurifoy, S.; Kothari, E.; Braunschweig, A., Optimization of 4D Polymer Printing Within a Massively Parallel Flow-Through Photochemical Microreactor. *Polymer Chemistry* **2016**.

109.   Singh-Gasson, S.; Green, R. D.; Yue, Y.; Nelson, C.; Blattner, F.; Sussman, M. R.; Cerrina, F., Maskless fabrication of light-directed oligonucleotide microarrays using a digital micromirror array. *Nat. Biotechnol.* **1999,** *17* (10), 974-978.

110.   Chen, X.; Venkatachalapathy, M.; Kamps, D.; Weigel, S.; Kumar, R.; Orlich, M.; Garrecht, R.; Hirtz, M.; Niemeyer, C. M.; Wu, Y. W., Molecular Activity Painting": Switch-Like, Light-Controlled Perturbations inside Living Cells. *Angew. Chem., Int. Ed.* **2017,** *56*, 5916.

111.   Bian, S.; Zieba, S. B.; Morris, W.; Han, X.; Richter, D. C.; Brown, K. A.; Mirkin, C. A.; Braunschweig, A. B., Beam pen lithography as a new tool for spatially controlled photochemistry, and its utilization in the synthesis of multivalent glycan arrays. *Chem. Sci.* **2014,** *5* (5), 2023-2030.

112.   Xie, Z.; Zhou, Y.; Hedrick, J. L.; Chen, P.-C.; He, S.; Shahjamali, M. M.; Wang, S.; Zheng, Z.; Mirkin, C. A., On-Tip Photo-Modulated Molecular Printing. *Angew. Chem. Int. Ed.* **2015,** *54* (44), 12894-12899.

113.   Brinkmann, F.; Hirtz, M.; Haller, A.; Gorges, T. M.; Vellekoop, M. J.; Riethdorf, S.; Müller, V.; Pantel, K.; Fuchs, H., A Versatile Microarray Platform for Capturing Rare Cells. *Sci. Rep.* **2015,** *5*, 15342.

114.   Kumar, R.; Bonicelli, A.; Sekula-Neuner, S.; Cato, A. C. B.; Hirtz, M.; Fuchs, H., Click-Chemistry Based Allergen Arrays Generated by Polymer Pen Lithography for Mast Cell Activation Studies. *Small* **2016,** *12* (38), 5330-5338.

115.   Cabezas, M. D.; Mirkin, C. A.; Mrksich, M., Nanopatterned Extracellular Matrices Enable Cell-Based Assays with a Mass Spectrometric Readout. *Nano Lett.* **2017**.

116.   Giam, L. R.; Massich, M. D.; Hao, L.; Shin Wong, L.; Mader, C. C.; Mirkin, C. A., Scanning Probe-Enabled Nanocombinatorics Define the Relationship between Fibronectin Feature Size and Stem Cell Fate. *Proc. Natl. Acad. Sci. U. S. A.* **2012,** *109*, 4377.

117.   Kumar, R.; Bonicelli, A.; Sekula-Neuner, S.; Cato, A. C. B.; Hirtz, M.; Fuchs, H., Click-Chemistry Based Allergen Arrays Generated by Polymer Pen Lithography for Mast Cell Activation Studies. *Small* **2016,** *12*, 5330.

118.   Chen, P. C.; Liu, G.; Zhou, Y.; Brown, K. A.; Chernyak, N.; Hedrick, J. L.; He, S.; Xie, Z.; Lin, Q. Y.; Dravid, V. P.; O'Neill-Slawecki, S. A.; Mirkin, C. A., Tip-Directed Synthesis of Multimetallic Nanoparticles. *J. Am. Chem. Soc.* **2015,** *137*, 9167.

119.   Chen, P.-C.; Liu, G.; Zhou, Y.; Brown, K. A.; Chernyak, N.; Hedrick, J. L.; He, S.; Xie, Z.; Lin, Q.-Y.; Dravid, V. P.; O'Neill-Slawecki, S. A.; Mirkin, C. A., Tip-Directed Synthesis of Multimetallic Nanoparticles. *J. Am. Chem. Soc.* **2015,** *137* (28), 9167–9173.

120.   Chen, P.-C.; Liu, X.; Hedrick, J. L.; Xie, Z.; Wang, S.; Lin, Q.-Y.; Hersam, M. C.; Dravid, V. P.; Mirkin, C. A., Polyelemental nanoparticle libraries. *Science* **2016,** *352* (6293), 1565-1569.

121.   Huang, L.; Chen, P.-C.; Liu, M.; Fu, X.; Gordiichuk, P.; Yu, Y.; Wolverton, C.; Kang, Y.; Mirkin, C. A., Catalyst design by scanning probe block copolymer lithography. *Proceedings of the National Academy of Sciences* **2018**.

122.   Nikolaev, P.; Hooper, D.; Perea-López, N.; Terrones, M.; Maruyama, B., Discovery of Wall-Selective Carbon Nanotube Growth Conditions via Automated Experimentation. *ACS Nano* **2014,** *8* (10), 10214-10222.

123.   Lin, Q. Y.; Mason, J. A.; Li, Z.; Zhou, W.; O'Brien, M. N.; Brown, K. A.; Jones, M. R.; Butun, S.; Lee, B.; Dravid, V. P., Building Superlattices from Individual Nanoparticles Via Template-Confined DNA-Mediated Assembly. *Science* **2018,** *359*, 669.

124.   Giam, L. R.; Massich, M. D.; Hao, L.; Shin Wong, L.; Mader, C. C.; Mirkin, C. A., Scanning probe-enabled nanocombinatorics define the relationship between fibronectin feature size and stem cell fate. *Proceedings of the National Academy of Sciences of the United States of America* **2012,** *109* (12), 4377-82.

125.   Liao, X.; Braunschweig, A. B.; Zheng, Z.; Mirkin, C. A., Force- and time-dependent feature size and shape control in molecular printing via polymer-pen lithography. *Small* **2010,** *6* (10), 1082-6.

126.   Brown, K.; Eichelsdoerfer, D.; Shim, W.; Rasin, B.; Radha, B.; Liao, X.; Schmucker, A.; Liu, G.; Mirkin, C., A cantilever-free approach to dot-matrix nanoprinting. *Proceedings of the National Academy of Sciences* **2013,** *110* (32), 12921-12924.

127.   Weeks, B. L.; Noy, A.; Miller, A. E.; De Yoreo, J. J., Effect of Dissolution Kinetics on Feature Size in Dip-Pen Nanolithography. *Physical Review Letters* **2002,** *88* (25).

128.   Piner, R. D.; Zhu, J.; Xu, F.; Hong, S.; Mirkin, C. A., "Dip-Pen" Nanolithography. *Science* **1999,** *283* (5402), 661-663.

129.   Ginger, D. S.; Zhang, H.; Mirkin, C. A., The evolution of dip-pen nanolithography. *Angewandte Chemie* **2004,** *43* (1), 30-45.

130.   Salaita, K.; Wang, Y.; Mirkin, C. A., Applications of dip-pen nanolithography. *Nat Nano* **2007,** *2* (3), 145-155.

131.   Vega, R. A.; Shen, C. K.; Maspoch, D.; Robach, J. G.; Lamb, R. A.; Mirkin, C. A., Monitoring single-cell infectivity from virus-particle nanoarrays fabricated by parallel dip-pen nanolithography. *Small* **2007,** *3* (9), 1482-5.

132.   Smith, J. C.; Lee, K.-B.; Wang, Q.; Finn, M. G.; Johnson, J. E.; Mrksich, M.; Mirkin, C. A., Nanopatterning the Chemospecific Immobilization of Cowpea Mosaic Virus Capsid. *Nano letters* **2003,** *3* (7), 883-886.

133.   Liu, X.; Fu, L.; Hong, S.; Dravid, V. P.; Mirkin, C. A., Arrays of Magnetic Nanoparticles Patterned via "Dip-Pen" Nanolithography. *Advanced Materials* **2002,** *14* (3), 231-234.

134.   Eichelsdoerfer, D. J.; Liao, X.; Cabezas, M. D.; Morris, W.; Radha, B.; Brown, K. A.; Giam, L. R.; Braunschweig, A. B.; Mirkin, C. A., Large-area molecular patterning with polymer pen lithography. *Nature protocols* **2013,** *8* (12), 2548-60.

135.   Zhou, Y.; Xie, Z.; Brown, K. A.; Park, D. J.; Zhou, X.; Chen, P. C.; Hirtz, M.; Lin, Q. Y.; Dravid, V. P.; Schatz, G. C.; Zheng, Z.; Mirkin, C. A., Apertureless cantilever-free pen arrays for scanning photochemical printing. *Small* **2015,** *11* (8), 913-8.

136.   Shim, W.; Braunschweig, A. B.; Liao, X.; Chai, J.; Lim, J. K.; Zheng, G.; Mirkin, C. A., Hard-tip, soft-spring lithography. *Nature* **2011,** *469* (7331), 516-20.

137.   Eichelsdoerfer, D. J.; Brown, K. A.; Boya, R.; Shim, W.; Mirkin, C. A., Tuning the spring constant of cantilever-free tip arrays. *Nano letters* **2013,** *13* (2), 664-7.

138.   Huo, F.; Zheng, G.; Liao, X.; Giam, L. R.; Chai, J.; Chen, X.; Shim, W.; Mirkin, C. A., Beam pen lithography. *Nature nanotechnology* **2010,** *5* (9), 637-40.

139.   Xie, Z.; Shen, Y.; Zhou, X.; Yang, Y.; Tang, Q.; Miao, Q.; Su, J.; Wu, H.; Zheng, Z., Polymer pen lithography using dual-elastomer tip arrays. *Small* **2012,** *8* (17), 2664-9.

140.   Schmid, H.; Michel, B., Siloxane Polymers for High-Resolution, High-Accuracy Soft Lithography. *Macromolecules* **2000,** *33*, 3042-3049.

141.   Odom, T. W.; Love, J. C.; Wolfe, D. B.; Paul, K. E.; Whitesides, G. M., Improved Pattern Transfer in Soft Lithography Using Composite Stamps. *Langmuir* **2002,** *18*, 5314-5320.

142.   Bowden, N.; Brittain, S.; Evans, A. G.; Hutchinson, J. W.; Whitesides, G. M., Spontaneous formation of ordered structures in thin films of metals supported on an elastomeric polymer. *Nature* **1998,** *393*, 146-149.

143.   Genzer, J.; Groenewold, J., Soft matter with hard skin: From skin wrinkles to templating and material characterization. *Soft Matter* **2006,** *2* (4), 310.

144.   Imburgia, M. J.; Crosby, A. J., Rolling wrinkles on elastic substrates. *Extreme Mechanics Letters* **2016,** *6*, 23-30.

145.   Ebata, Y.; Croll, A. B.; Crosby, A. J., Wrinkling and strain localizations in polymer thin films. *Soft Matter* **2012,** *8* (35), 9086.

146.   Khang, D.-Y.; Rogers, J. A.; Lee, H. H., Mechanical Buckling: Mechanics, Metrology, and Stretchable Electronics. *Advanced Functional Materials* **2009,** *19* (10), 1526-1536.

147.   Nania, M.; Matar, O. K.; Cabral, J. T., Frontal vitrification of PDMS using air plasma and consequences for surface wrinkling. *Soft Matter* **2015,** *11* (15), 3067-75.

148.   Liao, X.; Braunschweig, A. B.; Mirkin, C. A., "Force-feedback" leveling of massively parallel arrays in polymer pen lithography. *Nano letters* **2010,** *10* (4), 1335-40.

149.   Zheng, Z.; Daniel, W. L.; Giam, L. R.; Huo, F.; Senesi, A. J.; Zheng, G.; Mirkin, C. A., Multiplexed protein arrays enabled by polymer pen lithography: addressing the inking challenge. *Angewandte Chemie* **2009,** *48* (41), 7626-9.

150.   Basabe-Desmonts, L.; Reinhoudt, D. N.; Crego-Calama, M., Combinatorial Fabrication of Fluorescent Patterns with Metal Ions Using Soft Lithography. *Advanced Materials* **2006,** *18* (8), 1028-1032.

151.   Wang, Y.; Giam, L. R.; Park, M.; Lenhert, S.; Fuchs, H.; Mirkin, C. A., A self-correcting inking strategy for cantilever arrays addressed by an inkjet printer and used for dip-pen nanolithography. *Small* **2008,** *4* (10), 1666-70.

152.   Zhong, J.; Sun, G.; He, D., Classic, liquid, and matrix-assisted dip-pen nanolithography for materials research. *Nanoscale* **2014,** *6* (21), 12217-28.

153.   Eichelsdoerfer, D. J.; Brown, K. A.; Mirkin, C. A., Capillary bridge rupture in dip-pen nanolithography. *Soft Matter* **2014,** *10* (30), 5603-8.

154.   Chai, J.; Huo, F.; Zheng, Z.; Giam, L. R.; Shim, W.; Mirkin, C. A., Scanning probe block copolymer lithography. *Proceedings of the National Academy of Sciences of the United States of America* **2010,** *107* (47), 20202-6.

155.   Chai, J.; Wong, L. S.; Giam, L.; Mirkin, C. A., Single-molecule protein arrays enabled by scanning probe block copolymer lithography. *Proceedings of the National Academy of Sciences of the United States of America* **2011,** *108* (49), 19521-5.

156.   Liu, G.; Eichelsdoerfer, D.; Rasin, B.; Zhou, Y.; Brown, K. A.; Liao, X.; Mirkin, C. A., Delineating the pathways for the site-directed synthesis of individual nanoparticles on surfaces. *Proceedings of the National Academy of Sciences of the United States of America* **2013,** *110* (3), 887-891.

157.   Chen, P. C.; Liu, G.; Zhou, Y.; Brown, K. A.; Chernyak, N.; Hedrick, J. L.; He, S.; Xie, Z.; Lin, Q. Y.; Dravid, V. P.; O'Neill-Slawecki, S. A.; Mirkin, C. A., Tip-Directed Synthesis of Multimetallic Nanoparticles. *Journal of the American Chemical Society* **2015,** *137* (28), 9167-73.

158.   Nie, Z.; Kumacheva, E., Patterning surfaces with functional polymers. *Nature materials* **2008,** *7*, 277-290.

159.   Mayr, L. M.; Bojanic, D., Novel trends in high-throughput screening. *Current opinion in pharmacology* **2009,** *9* (5), 580-8.

160.   Fonseca, M. H.; List, B., Combinatorial chemistry and high-throughput screening for the discovery of organocatalysts. *Curr Opin Chem Biol* **2004,** *8* (3), 319-26.

161.   Weidenhof, B.; Reiser, M.; Stowe, K.; Maier, W. F.; Kim, M.; Azurdia, J.; Gulari, E.; Seker, E.; Barks, A.; Laine, R. M., High-throughput screening of nanoparticle catalysts made by flame spray pyrolysis as hydrocarbon/NO oxidation catalysts. *Journal of the American Chemical Society* **2009,** *131* (26), 9207-19.

162.   Mei, Y.; Saha, K.; Bogatyrev, S. R.; Yang, J.; Hook, A. L.; Kalcioglu, Z. I.; Cho, S. W.; Mitalipova, M.; Pyzocha, N.; Rojas, F.; Van Vliet, K. J.; Davies, M. C.; Alexander, M. R.; Langer, R.; Jaenisch, R.; Anderson, D. G., Combinatorial development of biomaterials for clonal growth of human pluripotent stem cells. *Nature materials* **2010,** *9* (9), 768-78.

163.   Al-Lazikani, B.; Banerji, U.; Workman, P., Combinatorial drug therapy for cancer in the post-genomic era. *Nature biotechnology* **2012,** *30* (7), 679-92.

164.   Khandurina, J.; Guttman, A. s., Microchip-based high-throughput screening analysis of combinatorial libraries. *Current Opinion in Chemical Biology* **2002,** *6*, 359-366.

165.   Battersby, B. J.; Trau, M., Novel miniaturized systems in high-throughput screening. *TRENDS in Biotechnology* **2002,** *20* (4), 167-173.

166.   Pham, N. P.; Burghartz, J. N.; Sarro, P. M., Spray coating of photoresist for pattern transfer on high topography surfaces. *Journal of Micromechanics and Microengineering* **2005,** *15* (4), 691-697.

167.   Shimizu, T.; Kenndler, E., Capillary electrophoresis of small solutes in linear polymer solutions: Relation between ionic mobility, diffusion coefficient and viscosity. *Electrophoresis* **1999,** *20*, 3364-3372.

168.   Dai, Q.; Rettner, C. T.; Davis, B.; Cheng, J.; Nelson, A., Topographically directed self-assembly of goldnanoparticles. *Journal of Materials Chemistry* **2011,** *21* (42), 16863.

169.   Kim, B. Y.; Shim, I. B.; Monti, O. L.; Pyun, J., Magnetic self-assembly of gold nanoparticle chains using dipolar core-shell colloids. *Chemical communications* **2011,** *47* (3), 890-2.

170.   Su, G.; Guo, Q.; Palmer, R. E., Colloidal Lines and Strings. *Langmuir* **2003,** *19*.

171.   Fahrni, C. J., Biological applications of X-ray fluorescence microscopy: exploring the subcellular topography and speciation of transition metals. *Curr Opin Chem Biol* **2007,** *11* (2), 121-7.

172.   Liao, X.; Brown, K. A.; Schmucker, A. L.; Liu, G.; He, S.; Shim, W.; Mirkin, C. A., Desktop Nanofabrication with Massively Multiplexed Beam Pen Lithography. *Nat. Commun.* **2013,** *4*, 2103.

173.   Gross, B. C.; Erkal, J. L.; Lockwood, S. Y.; Chen, C.; Spence, D. M., Evaluation of 3D Printing and Its Potential Impact on Biotechnology and the Chemical Sciences. *Analytical Chemistry* **2014,** *86* (7), 3240-3253.

174.   Huang, S. H.; Liu, P.; Mokasdar, A.; Hou, L., Additive manufacturing and its societal impact: a literature review. *The International Journal of Advanced Manufacturing Technology* **2013,** *67* (5), 1191-1203.

175.   Kruth, J. P.; Leu, M. C.; Nakagawa, T., Progress in Additive Manufacturing and Rapid Prototyping. *CIRP Annals* **1998,** *47* (2), 525-540.

176.   Petrick, I. J.; Simpson, T. W., 3D Printing Disrupts Manufacturing: How Economies of One Create New Rules of Competition. *Research-Technology Management* **2013,** *56* (6), 12-16.

177.   Kelly, B. E.; Bhattacharya, I.; Heidari, H.; Shusteff, M.; Spadaccini, C. M.; Taylor, H. K., Volumetric additive manufacturing via tomographic reconstruction. *Science* **2019,** *363* (6431), 1075.

178.   de Beer, M. P.; van der Laan, H. L.; Cole, M. A.; Whelan, R. J.; Burns, M. A.; Scott, T. F., Rapid, continuous additive manufacturing by volumetric polymerization inhibition patterning. *Science Advances* **2019,** *5* (1), eaau8723.

179.   Ngo, T. D.; Kashani, A.; Imbalzano, G.; Nguyen, K. T. Q.; Hui, D., Additive manufacturing (3D printing): A review of materials, methods, applications and challenges. *Composites Part B: Engineering* **2018,** *143*, 172-196.

180.   Wohlers, T.; Caffrey, T., *Additive Manufacturing: Going Mainstream*. 2013; Vol. 150, p 67-73.

181.   Truby, R. L.; Lewis, J. A., Printing soft matter in three dimensions. *Nature* **2016,** *540*, 371-378.

182.   Zheng, X.; Lee, H.; Weisgraber, T. H.; Shusteff, M.; DeOtte, J.; Duoss, E. B.; Kuntz, J. D.; Biener, M. M.; Ge, Q.; Jackson, J. A.; Kucheyev, S. O.; Fang, N. X.; Spadaccini, C. M., Ultralight, ultrastiff mechanical metamaterials. *Science* **2014,** *344* (6190), 1373-1377.

183.   Yagci, Y.; Jockusch, S.; Turro, N. J., Photoinitiated Polymerization: Advances, Challenges, and Opportunities. *Macromolecules* **2010,** *43* (15), 6245-6260.

184.   Bártolo, P. J., *Stereolithography: materials, processes and applications*. Springer Science & Business Media: 2011.

185.   Tumbleston, J. R.; Shirvanyants, D.; Ermoshkin, N.; Janusziewicz, R.; Johnson, A. R.; Kelly, D.; Chen, K.; Pinschmidt, R.; Rolland, J. P.; Ermoshkin, A.; Samulski, E. T.; DeSimone, J. M., Continuous liquid interface production of 3D objects. *Science* **2015,** *347* (6228), 1349-1352.

186.   Janusziewicz, R.; Tumbleston, J. R.; Quintanilla, A. L.; Mecham, S. J.; DeSimone, J. M., Layerless fabrication with continuous liquid interface production. *Proceedings of the National Academy of Sciences* **2016,** *113* (42), 11703-11708.

187.   Hiroyuki, N.; Fumiki, T.; Takeshi, K.; Satoru, I.; Katsumasa, S., Reaction heat effects on initial linear shrinkage and deformation in stereolithography. *Rapid Prototyping Journal* **1999,** *5* (3), 120-128.

188.   Corcione, C. E.; Greco, A.; Maffezzoli, A., Temperature evolution during stereolithography building with a commercial epoxy resin. *Polymer Engineering & Science* **2006,** *46* (4), 493-502.

189.   Wong, T.-S.; Kang, S. H.; Tang, S. K. Y.; Smythe, E. J.; Hatton, B. D.; Grinthal, A.; Aizenberg, J., Bioinspired self-repairing slippery surfaces with pressure-stable omniphobicity. *Nature* **2011,** *477*, 443–447.

190.   Amini, S.; Kolle, S.; Petrone, L.; Ahanotu, O.; Sunny, S.; Sutanto, C. N.; Hoon, S.; Cohen, L.; Weaver, J. C.; Aizenberg, J.; Vogel, N.; Miserez, A., Preventing mussel adhesion using lubricant-infused materials. *Science* **2017,** *357* (6352), 668-673.

191.   Unkovskiy, A.; Bui, P. H.-B.; Schille, C.; Geis-Gerstorfer, J.; Huettig, F.; Spintzyk, S., Objects build orientation, positioning, and curing influence dimensional accuracy and flexural properties of stereolithographically printed resin. *Dental Materials* **2018,** *34* (12), e324-e333.

192.   Thielicke, W.; Stamhuis, E. J., PIVlab – Towards User-friendly, Affordable and Accurate Digital Particle Image Velocimetry in MATLAB. *Journal of Open Research Software* **2014,** *2* (1), 30.

193.   Huang, P.; Guasto, J. S.; Breuer, K. S., Direct measurement of slip velocities using three-dimensional total internal reflection velocimetry. *Journal of Fluid Mechanics* **2006,** *566*, 447-464.

194.   Tretheway, D. C.; Meinhart, C. D., Apparent fluid slip at hydrophobic microchannel walls. *Physics of Fluids* **2002,** *14* (3), L9-L12.

195.   Kaoullas, G.; Georgiou, G. C., Newtonian Poiseuille flows with slip and non-zero slip yield stress. *Journal of Non-Newtonian Fluid Mechanics* **2013,** *197*, 24-30.

196.   Eckel, Z. C.; Zhou, C.; Martin, J. H.; Jacobsen, A. J.; Carter, W. B.; Schaedler, T. A., Additive manufacturing of polymer-derived ceramics. *Science* **2015,** *351* (6268), 58.

197.   Liew, L.-A.; Liu, Y.; Luo, R.; Cross, T.; An, L.; Bright, V. M.; Dunn, M. L.; Daily, J. W.; Raj, R., Fabrication of SiCN MEMS by photopolymerization of pre-ceramic polymer. *Sensors and Actuators A: Physical* **2002,** *95* (2–3), 120-134.

198.   Husár, B.; Ligon, S. C.; Wutzel, H.; Hoffmann, H.; Liska, R., The formulator's guide to anti-oxygen inhibition additives. *Progress in Organic Coatings* **2014,** *77* (11), 1789-1798.

199.   Ligon, S. C.; Liska, R.; Stampfl, J.; Gurr, M.; Mülhaupt, R., Polymers for 3D Printing and Customized Additive Manufacturing. *Chemical Reviews* **2017,** *117* (15), 10212-10290.

200.   Eckel, Z. C.; Zhou, C.; Martin, J. H.; Jacobsen, A. J.; Carter, W. B.; Schaedler, T. A., Additive manufacturing of polymer-derived ceramics. *Science* **2016,** *351* (6268), 58-62.

201.   ASTM D638-10, Standard Test Method for Tensile Properties of Plastics, ASTM International, West Conshohocken, PA, 2010, www.astm.org.

202.   Eichelsdoerfer, D. J.; Liao, X.; Cabezas, M. D.; Morris, W.; Radha, B.; Brown, K. A.; Giam, L. R.; Braunschweig, A. B.; Mirkin, C. A., Large-Area Molecular Patterning with Polymer Pen Lithography. *Nat. Protoc.* **2013,** *8*, 2548.

203. Dumesic, J. A.; Huber, G. W.; Boudart, M., Principles of Heterogeneous Catalysis. In *Handbook of Heterogeneous Catalysis*, Wiley-VCH Verlag GmbH & Co. KGaA: 2008.

204. Huo, F.; Zheng, Z.; Zheng, G.; Giam, L. R.; Zhang, H.; Mirkin, C. A., Polymer pen lithography. *Science* **2008,** *321* (5896), 1658-60.

Appendix I: Materials and Methods

Materials:

Polydimethylsiloxane was made from a 10 to 1 ratio of Slygard 184 from Dow Corning. 16-mercaptohexadecanoic acid (MHA), hexamethyldisilazane were obtained from Sigma-Aldrich. Poly(ethylene oxide)-*b*-poly(2-vinyl pyridine) (PEO-*b*-P2VP, Mn=2.8-*b*-1.5 kg·mol^{-1}) was obtained from Polymer Source. Glass slides (2 in.) were obtained at VWR. Monomers were obtained from Sigma-Aldrich and TCI America. Sulfo-cyanine5 NHS ester was obtained from Lumiprobe Corporation. Metal compounds, auric acid, sodium tetrachloropalladate, and cupric nitrate, were purchased from Sigma-Adrich, Inc. and used without further purification. Harder Steenbeck Infinity 2 in 1 CR plus airbrush with Harder Steenbeck fine pressure valve and Iwata Power Jet Pro IS-975 Dual Piston Compressor were obtained from Chicago Air Supply. 4" P doped silicon oxide wafers were obtained from Nova Electronic Materials. Oligomers were obtained from Dymax Corporation and Gelest. Photoinitiators were obtained from BASF and IGM Resins. The fluorinated oils were purchased from The Chemours Company and Solvay

Fabrication:

Standard fabrication of PPL arrays were made as previously reported.[134, 204] PPL arrays were then inserted into PECVD chamber to be coated with silica at 900 mTorr while introducing 500 sccm SH_4 and 1420 sccm O_2 and 30 W of high frequency power for 320 s with a base plate temperature of 200 ºC using a STS LpX CVD.

Ink preparation:

Solutions of 10 mM MHA in ethanol and 5 mg/ml of PEO-*b*-P2VP in water were prepared. All arrays were plasma cleaned for 2 min under oxygen at 60 W. Fluorophore-containing inks were aqueous solutions were composed of 5 mg/mL of PEO-*b*-P2VP along with 10 mg/mL of a

fluorophore (either rhodamine 6G or sulfo-cyanine5 NHS ester). Solutions with fluorophore compounds were wrapped in foil and kept on a shaker for 1 h. Inks for metal nanoparticle synthesis were composed of 5 mg/mL of PEO-*b*-P2VP and a concentration of metal precursors with a molar ratio of pyridine groups to metal atoms ranging from 64 (XRF measurements) to 256 (SWNT growths). The pH of solutions containing metal precursors were brought to pH values of 3-4 and shaken for 12-24 h.

Spray Coater:

All pen arrays were plasma cleaned for 2 min under oxygen at 60 W prior to spray inking. The ink solutions (150 µL per gun) were spray-coated onto the array using 0.15 mm needles at 20 psi airflow using Harder Steenbeck Infinity CR plus airbrushes with an Iwata Power Jet Pro IS-975 dual piston compressor. The two airbrushes were sprayed in unison. After spraying, the pen arrays were placed with the pens facing up and covered for 15 min while the solution dried. Custom airbrush holders were designed on TinkerCad, rendered in Slic3r, and 3D printed out of acrylonitrile butadiene styrene using a SeeMeCNC Orion Delta 3D printer.

Substrate preparation:

PEO-*b*-P2VP based ink was patterned on silicon wafers that had been vapor coated in a desiccator for 24 hours with hexamethyldisilazane to render it hydrophobic. MHA features were patterned onto Au-coated silicon wafers. These wafers were coated with 5 nm Ti followed by 35 nm Au using a Kurt J. Lesker Co. PVD 75 electron-beam evaporator.

Patterning:

PPL patterning was performed with a Park XE-150 in a humidity control chamber at a relative humidity between 70-95% and at room temperature. BPL patterning was performed with TeraPrint E-series both force and exposure time where varied.

Nanoparticle Synthesis:

In order to convert polymer features into nanoparticles, the substrate was put into a tube furnace and thermally annealed. The heating conditions were programmed as follows: ramp to 120 °C under Ar (flow rate: 1.1 L/min) in 1 h, hold at 120 °C for 48 h, then cool back to room temperature in 4 h, switch the atmosphere into H_2 (flow rate: 4.2 L/min), ramp to 500 °C in 2 h, calcine the substrate at 500 °C for 12 h, and finally cool down to room temperature over 6 h.

Imaging:

Atomic force microscope (AFM) measurements were performed on a Dimension Icon (Bruker) to obtain 3D profiles of the patterns. Tapping mode was used for polymeric features and lateral force microscopy was used for MHA features. Images were processed in Nanoscope Analysis. Optical images were taken with a Zeiss Imaginer.M2m and Zeiss LSM 800 Confocal Microscope. Images were processed with ImageJ and Zen Blue. X-ray fluorescence was carried out at the Northwestern J.B.Cohen X-Ray Diffraction Facility using a 18 kW Mo Rigaku. Relative fluorescence intensities of gold and palladium were calculated from the fluorescent peaks and compared in order to give relative concentrations of the two elements.

X-Ray Fluorescence

Data was collected at sector 5 BMD of the Advanced Photon Source. Fluorescence spectra were collected at an incident energy of 24.8 keV using two four-element Vortex ME-4 silicon drift diode detectors. The sample was placed in a glancing-incidence geometry with respect to the X-ray beam,

at an angle of ~0.1°. A horizontal slit size of 3 mm was used and the sample translated in order to probe the Au-Pd gradient at various points on the sample. The vertical slit size was adjusted according to footprint calculation, such that the entire sample length would be measured, in order to both maximize fluorescence counts from the elements of interest and achieve a global representation of the Au-Pd gradient.

Beam Pen Fabrication:

BPL pen arrays are generated from Polymer-Pen Lithography (PPL) pen arrays. Once the PDMS pyramidal arrays are formed on a 2"x2" quartz slide, these pens can be coated with 200 nm of Au via electron-beam vapor deposition with a 2-5 nm titanium adhesion layer used to prevent gold lift-off. Once a Au coated PPL array is formed, the array can be incubated in a 10 mM methanolic solution of 1H,1H,2H,2H-perfluorodecanethiol (PFDT) for 8 to 24 hours to form a fluorinated self-assembled monolayer (SAM). This SAM promotes wetting of a fluorinated oil masking material on the pen array in subsequent steps.

A spin-coater is then used to apply the fluorinated oil masking layer, Krytox GPL-1000. Because the viscosity of the oil varies drastically with temperature, the exact spin-recipe must be constantly adjusted to account for minor shifts in the ambient temperature. An example spin-sequence typically resembles an acceleration of 100 RPM/sec from 0 to 7,5000 RPM and then held at this speed for 30 seconds; the sample is then decelerated at 500 RPM/sec until 0 RPM. The goal of the spin-coating procedure is to achieve a thin oil layer which spans the entire pen array and whose thickness is approximately 1 μm below the apex of the gold coated pens. At room temperature, the viscosity of the oil is quite high (~2,610 cST at 20°C); at these micro-scale thicknesses (~15 μm) the oil behaves as a solid. The mask can be 'melted' by heating the sample

on a hotplate at 60°C for 3 minutes. This step allows for two critical aspects. First, as the oil begins to flow it will self-level across the entire pen array in the event there are any remnant variations in oil thickness across the array. Secondly, allowing the oil to flow allows for the liquid mask to climb to the apex of the gold coated pens and to form a meniscus. After 3 minutes, the pen array is removed from the heat and allowed to cool on a level surface. This allows for the oil to thicken and re-solidify. The meniscus around each pen can be visualized in dark-field mode using reflective optical microscopy. A characteristic circular interference pattern can be observed around each pen due to the curvature of the oil layer as it forms a meniscus.

Etching of the masked pen arrays is conducted using an iodine etchant solution. When the masked pens are submerged in the aqueous etchant solution, a three-phase interface is formed. As the gold at the apex is dissolved, the SAM resting upon the gold is removed. As the SAM recedes with further etching, the oil mask begins to retract downward. Both the concentration and exposure time effect the rate at which etching occurs and must be optimized. A typical etching concentration is 2% etchant in deionized water. A typical etching time is 60 seconds. The size of the resulting apertures can be varied by tuning these parameters. The etching can be quenched by removing the pen array from the etchant solution and rinsing it in a deionized water bath.

Following the etching of the gold apertures, the oil mask can be removed using a perfluorinated polyether solvent (Miller Stephenson, PFPE Re-Move) which solubilizes the oil. The pen array is rinsed by this solvent and blown dry with a stream of dry nitrogen. With the oil removed, the pen array and apertures can be imaged by SEM (Hitachi 8030).

Resin Formulations:

Hard, Machinable Urethane Acrylate

IGM Resin Omnirad 819 (Phenylbis(2,4,6-trimethylbenzyl)phosphine oxide, CAS 162881-26-7)

or BASF TPO (Diphenyl(2,4,6-trimethylbenzoyl)phosphine oxide, CAS 75980-60-8)

1,6-Hexanediol diacrylate (HDDA) monomer diluent

Dymax BT-970 (a proprietary polyurethane difunctional acrylate)

Elastomeric Urethane Acrylate

IGM Resin Omnirad 819 (Phenylbis(2,4,6-trimethylbenzyl)phosphine oxide, CAS 162881-26-7)

or BASF TPO (Diphenyl(2,4,6-trimethylbenzoyl)phosphine oxide, CAS 75980-60-8)

Isobornyl Acrylate (IBOA) monomer diluent

Dymax BR-345 (a proprietary polyether-urethane difunctional acrylate)

Ceramic (Formulation Adapted from reference Kaollas and Georgiou[195])

IGM Resin Omnirad 819 (Phenylbis(2,4,6-trimethylbenzyl)phosphine oxide, CAS 162881-26-7)

or BASF TPO (Diphenyl(2,4,6-trimethylbenzoyl)phosphine oxide, CAS 75980-60-8)

Gelest SMS-992, (Mercaptopropyl)methylsiloxane homopolymer (CAS 102783-03-9)

Gelest VMM-010, Vinylmethoxysiloxane homopolymer (CAS 131298-48-1)

Butadiene Rubber (Proprietary Formulation)

IGM Resin Omnirad 819 (Phenylbis(2,4,6-trimethylbenzyl)phosphine oxide, CAS 162881-26-7)

or BASF TPO (Diphenyl(2,4,6-trimethylbenzoyl)phosphine oxide, CAS 75980-60-8)

Mixture of Poly(butadiene) oligomers, monomer diluents, and polymerization additives

ABS-Like Urethane Acrylate (Proprietary Formulation)

IGM Resin Omnirad 819 (Phenylbis(2,4,6-trimethylbenzyl)phosphine oxide, CAS 162881-26-7)

or BASF TPO (Diphenyl(2,4,6-trimethylbenzoyl)phosphine oxide, CAS 75980-60-8)

Mixture of polyurethane oligomers, monomer diluents, and polymerization additives

3D Object Design, Slicing, Video Preparation, and UV Projection:

3D STL objects were designed in Blender, an open source CAD rendering software geared towards graphic arts and video processing. These objects were then transferred into Autodesk Netfabb, in which support structures (as needed) could be applied. Netfabb was used to slice the STL objects and accompanying supports into 10µm layer JPEG images with lateral resolutions corresponding to the UV projection source. Once an image stack was generated, the images were loaded back into Blender and compiled into AVI video files playing at 12 frames per second (12fps x 10µm/frame = 120 µm/sec video). Once compiled, these videos could be played via standard video codecs and media players, such as VLC media player. Additionally, the frame rate of said videos could be advanced or slowed within these media players (allowing the user to run the video at a 30, 60 or 240 µm/sec rate). The videos were projected through a series of DLP (Digital Light Processing) projectors modified to project UV light. Lamp sources varied between different printers; some projection systems utilized medium pressure Hg lamps while others used monochromatic UV LEDs. The projectors were stitched together to create a continuous large projection field of view (maximum projection field of view was 15" x 24" at 240 µm pixel resolution).

Fluid Flow System:

The fluid flow system consists of a low-iron glass aquarium, an outlet manifold, a four-lobe diaphragm pump, a series of microparticulate filters, a thin-wall plate heat exchanger, and a return inlet manifold. The inlet and outlet manifolds, responsible for removing the oil and returning the oil to the glass aquarium, were designed to generate a uniform velocity profile

across the build region. A recirculating chiller was plumbed through the heat exchanger to cool the oil; the chiller unit was sized to correspond to the printers build region (i.e. smaller printers only require a bench-top recirculating chiller, whereas the larger 15"x24" build region mentioned above required a larger Thermo Scientific Merlin-M150 industrial chiller to sufficiently remove heat from the system).

Printing Procedure:

Prior to printing, the fluid flow system was turned on to allow for the oil temperature to equilibrate to a temperature between 10 ℃ and 15 ℃. At this point the flow was temporarily stopped to pour resin into the system, so as to avoid resin entering the outlet oil manifold, and the flow restarted. The print stage, held by a ball-screw actuator arm, was then brought into contact with the oil-resin interface. A 30 second UV exposure time was used to generate the initial adhesive layer of resin onto the steel build platform, and then the video was started in conjunction with the retraction of the build platform at 120 µm/sec. While print speeds of 240 µm/sec could be achieved, the quality of such prints and the reliability of the print process dropped substantially.

Post Processing:

After the print was finished, the part was removed from the stage and washed in methanol to remove any unsolidified resin. Support structures were then removed from the part manually. Finally, 'green' (i.e., not fully cured) parts were placed under a high intensity Hg arc UV lamp to complete the curing process to give the final material properties.

Particle Image Velocimetry:

Particle image velocimetry (PIV) was used to map the flow velocity of the system as a function of the volumetric flow rate (50% - 100% power of the positive displacement pump utilized). The print vat was filled with oil and resin (without photo-initiator) and the oil phase recirculated using a pair of flow manifolds. A block was then placed in the vat at the resin-oil interface to represent a cured part, while particulate matter was mixed with the oil and flown across the field of view (Figure 5.4). A line laser was projected from the bottom of the vat to illuminate the particulate matter in the oil phase to enable tracking of the oil flow profile via right-angle scattering into an Edmunds Optics EO-1312M camera (Figure 5.4A). Videos were then converted into image stacks using VLC media player and then processed using PIVlab, an application designed for MATLAB to analyze the flow profile (Figure 5.4C).[190]

Photomicrography:

All optical images and videos of objects were taken with a Canon 70D camera. Particle image velocimetry videos were collected with an Edmunds Optics EO-1312M camera. Thermal imaging was performed using FLIR SC7650 IR camera calibrated for a sensor range of 20 $^{\circ}$C to 150 $^{\circ}$C.

Energy Cure and Penetration Depth Testing of Resins:

The energy cure response and depth of light penetration into the resin are critical parameters in ensuring that a resin formulation will perform on the HARP printer. These parameters can be measured using the protocol documented by Joe Bennett of the National Institute of Standards and Technology (NIST, Gaithersburg, MD, USA) *(29)*. In brief, the penetration of our UV light being projected into the pool of resin can be described by the Beer-Lambert relationship:

$P(z)=P_o\cdot\exp[-z/D_p]$

Where P is the UV power (mW/cm^2) at some depth, z (μm), away from the print interface,

P_o is the power at the interface where $z = 0$ μm, and D_p (μm) is the characteristic distance

parameter describing how the intensity of light decreases as it enters the pool of resin. From this

relationship, we can rearrange to solve for the Jacobs' working curve equation:

$C_d=D_p\cdot\ln(E_o/E_c)$

Where C_d is the cure depth (or thickness of solidified resin, μm), E_o is the energy of UV

light delivered at the interface (i.e., $E_o=\int P_o dt$; mJ/cm^2), and E_c is the critical energy of UV light

(mJ/cm^2) that must be delivered to cause a solidification of resin at some corresponding depth

C_d.

With the working curve equation, one can now expose resin on a glass substrate to a known

amount of UV light from the UV source of interest (in this case, our UV patterning projector

systems for varying amounts of time) and then measure the resulting height of the cured part, C_d,

using a caliper. A series of data points corresponding to different exposure times (and thus

different values of E_o) can be plotted and fit to a logarithmic curve using a non-linear least-

squares solver to yield the constants E_c and D_p specific to the resin chemistry and the optical

system being tested.

The resin chemistries most compatible with HARP typically have low E_c values ranging between 10-30 mJ/cm^2 and penetration depths, D_p, ranging between 300 to 800 μm. In a typical experiment, a resin with a E_c value between 10-20 mJ/cm^2 can be successfully printed at vertical print rates of 120 μm/s (lower E_c corresponds with higher chemical reactivity and stronger photo-response). Less reactive resins with a higher E_c value between 20-30 mJ/cm^2 can be successfully printed at vertical print rates ranging between 20-60 μm/s depending on the penetration depth.

CURRICULUM VITAE

JAMES HEDRICK

Jameshedrick2013@u.northwestern.edu
(925) 202-1467

Education: **Northwestern University**   Evanston, IL
Candidate for Doctor of Philosophy in Chemical and Biological Engineering,
Supervisor: Professor Chad Mirkin
Expected graduation date April 2019
GPA: 3.8/4.0

Northwestern University, Kellogg School of Management   Evanston, IL
Certificate Program, Management for Scientists and Engineers
August 2017

Massachusetts Institute of Technology   Cambridge, MA
Bachelor of Science degree in Chemical-Biological Engineering
with Minor in Biology, February 2013
GPA: 4.3/5.0

Publications: Walker†, D. A.; **Hedrick†, J. L.;** Mirkin, C. A., "The structural evolution of Three-Component Nanoparticles in Polymer Nanoreators." Science Submitted.

Gosavi, A.A.; **Hedrick, J. L.;** Chen, P.; Notestein, J. M.; Mirkin, C. A., "_A tri-layer approach to controlling nanopore formation in oxide supports." Nano Res 2019, 1-6.

Brown†, K.A.; **Hedrick†, J. L.;** Eichelsdoerfer, D. J.; Mirkin, C. A., " Nanocombinatorics with Cantilever-Free Scanning Probe Arrays." ACS Nano 2019, 13, 8-17.

Kluender†, E. J.; **Hedrick†, J. L.;** Brown, K.; Rao, R.; Meckes, B Du, J. S.; Moreau, L. M.; Maruyama, B.; Mirkin, C. A., "Catalyst discovery through megalibraries of nanomaterials." PNAS 2019, 116, 40-45. Highlighted in *Science* and *Nature Reviews Chemistry.*

Chen, P.; Du, J. S.; Meckes, B.; Huang, L.; Xie, Z.; **Hedrick, J. L.;** Dravid, V. P.; Mirkin, C. A., "The structural evolution of Three-Component Nanoparticles in Polymer Nanoreators." J. Am. Chem. Soc. 2017, 139, 9876–9884.

Chen, P.; Liu, X.; **Hedrick, J.L.;** Xie, Z.; Wang, S.; Lin, Q.; Hersam, M.C.; Dravid, V.P.; and Mirkin, C.A., "Polyelemental nanoparticle libraries." Science 2016, 352, 1565-1569.

Fevre, M.; Wojtecki, R.J.; **Hedrick, J.;** Garcia, J.M.; Hedrick, J.L., " Tailorable Thermal Properties Through Reactive Blending Using Orthogonal Chemistries and Layer-by-Layer Deposition of Poly (1, 3, 5-hexahydro-1, 3, 5-triazine) Networks." Advanced Functional Materials 2016, 26, 5560-5568.

Hedrick†, J.L.; Brown†, K.A.; Kluender, E.J.; Chen, P.; Cabezas, M.D.; Mirkin, C.A., " Hard Transparent Arrays for Polymer Pen Lithography." ACS Nano 2016, 10, 3144–3148.

Xie, Z.; Zhou, Y.; Chen, P.; **Hedrick, J.L.;** He, S.; Shahjamali, M.; Wang, S.; Zheng, Z.; Mirkin, C.A., "On-Tip Photo-Modulated Molecular Printing." Angew. Chem. Int. Ed. Engl. 2015, 54, 12894-12899.

Chen, P.; Liu, G.; Zhou, Y.; Brown, K.A.; Chernyak, N.; **Hedrick, J.L.;** He, S.; Xie, Z.; Lin, Q.; Dravid, V.P.; Mirkin, C.A., "Tip-Directed Synthesis of Multimetallic Nanoparticles." J. Am. Chem. Soc. 2015, 137, 9167–9173.

Lee, J.; Lin, E-W.; Lau, U. Y.; **Hedrick, J. L.;** Bat E.; Maynard, H. D., "Trehalose glycopolymers as excipients for protein stabilization." Biomacromolecules 2013, 14, 2561-2569.

Opatkiewicz, J.P.; LeMieux, M.C.; Liu, D.; Vosgueritchian, M.; Barman, S.N.; Elkins, C.M.; **Hedrick, J.L.;** Bao, Z., "Using nitrile functional groups to replace amines for solution-deposited single-walled carbon nanotube network films." ACS Nano 2012 6 (6), 4845-4853.

Venkataraman, S.; **Hedrick, J. L.;** Ong, Z. Y.; Yang, C., Ee, P. L. R.; Hammond, P. T.; Yang, Y. Y., "The effects of polymeric nanostructure shape on drug delivery." Advanced Drug Delivery Reviews 2011, published online.

Attia†, B. E.; Ong†, Z. Y.; **Hedrick†, J. L.;** Lee, P. P.; Hammond, P. T.; Yang, Y. Y., "Mixed micelles self-assembled from block copolymers for drug delivery Current Opinion in Colloid and Interface." Science 2011, 16, 182–194.

Patents: Hedrick, J.L., Mirkin, C.A., Brown, K.A. "Gradient Spray Coating Polymer Pen Arrays," PCT/US2015/295,914. Granted.

Hedrick, J.L., Mirkin, C.A., Brown, K.A."Silica polymer pen lithography," PCT/US2015/299,565. Granted.

Hedrick, J.L., Mirkin, C.A., Walker, D.A. "Method for the Fabrication of Three-Dimensional Objects and Apparatus for Same," PCT/US2017/35,221.

Hedrick, J.L., Mirkin, C.A., Walker, D.A. "Liquid Masks for Microfabrication Processes" US 62/431,116.

Presentations: Invited Talk - Synthesis and screening of highly tailorable nanoparticle combinatorial libraries; Maynard Group Ten Years after Tenure, UCLA, 2018

Invited Talk - Synthesis of highly tailorable nanoparticle combinatorial libraries; ACS National Fall Meeting, oral, 2017

Synthesis of highly tailorable nanoparticle combinatorial libraries; ACS National Spring Meeting, oral and Sci-Mix poster, 2017

Utilizing hard transparent arrays for polymer pen lithography for high resolution patterning; ACS National Spring Meeting, oral, 2017

Synthesis of highly tailorable nanoparticle combinatorial libraries; Zing Polymer Chemistry Conference, poster, 2016

Combinatorial libraries of alloy nanoparticles individually synthesized through scanning probe spray gradients; ACS National Spring Meeting, oral, 2016

Experience: **Northwestern University**   Evanston, IL
December 2013- Present
Professor Chad Mirkin
Graduate Student in the Department of Chemical and Biological Engineering.
Using cantelever-free lithography to pattern nanoreactors onto substrates for catalytic screening. Extending the capabilities of polymer pen lithography. Nanoscale patterning of multifunctional materials in a 3D architecture.

Massachusetts Institute of Technology   Cambridge, MA
February 2013- May 2013
Professor Alan Hatton
Research Assistant in the Department of Chemical Engineering.
Creating and characterizing carbon nano fibers for supercapacitors, carbon sequestration, and biosensors.

Massachusetts Institute of Technology   Cambridge, MA
January 2010- May 2012
Professor Paula T. Hammond
Internship in the Department of Chemical Engineering.
Worked mainly in drug and gene delivery for cancer research. Created layer by layer (lbl) nanoparticles and block copolymer micelles. Learned and used NMR (Nuclear Magnetic Resonance), Spectrofluorometry, HPLC (High-Performance Liquid Chromatography), and CMC (Critical Micelle Concentration).

University of California Los Angeles   Los Angeles, CA
June-August 2012
Professor Heather D. Maynard
Amgen Scholars Program
Synthesized polymers for protein therapy through free radical polymerization, and analyzed their cytotoxicity.

University of Cagliari   Cagliari, Italy
June-August 2011
Professor Biancamaria Baroli
Internship in the Department of Toxicology.
Observed the functionalization of gold nanoparticles with two separate lipophilic drugs used for the treatment of osteosarcoma through thiol conjugation followed by PEGylation.

Stanford University   Stanford, CA
June-August 2010
Professor Zhenan Bao
Internship in the Department of Chemical Engineering.
Performed research in the area of Carbon Nanotubes (CNTs) sorting, purification, assembly and devices. Optimized plating CNTs on silicon wafers by modifying the surface of the wafer and the deposition solvent of the CNTs. Primarily used Atomic Force Microscope (AFM) in my research.

Imperial College   London, United Kingdom
June-July 2008
Professor Andrew J. George
Internship in the Department of Medicine. Research was focused in the area of organ transplantation and gene therapy research. Learned and performed many different procedures: polymerase chain reaction (PCR) (assembly, purification, real time, midiprep, etc.), western blot, DNA electrophoresis, how to split adherent, nonadherent, primary, and cancer cell line cells.

IBM Almaden Research Center   San Jose, CA
July-August 2007
Internship in the Division of Science and Technology. Operated the Thermal Analysis Laboratory. Specifically operated Thermogravimetric Analysis and Differential Scanning Calorimetry machines.

Companies: **CDJ Technologies**   Evanston, IL
December 2016- Present
Co-founder of industrial 3D printing company for manufacturing.

Design and develop next generation 3D printers for direct manufacturing of commodities.

Fellowships and Awards:
2017, Northwestern Chemical and Biological Engineering Distinguished Graduate Researcher Award Runner Up
2017, Northwestern University Honorary Terminal Year Fellow
2016, Royal Society of Chemistry Polymer Chemistry Best Poster Prize at the Zing Polymer Chemistry Conference
2016, Ryan Fellowship
2014-2017, National Defense Science and Engineering Graduate (NDSEG) Fellowship
2014, National Science Foundation (NSF) Honorable Mention
2013-2014, GEM Associate Fellow

Community Service:
2017, Developed and executed a Science Café workshop at the Museum of Science and Industry on Microfluidics.
2016, Designed and presented nanoscience demo to Boy Scout Troup as part of the Northwestern's STEM & Sports Day
2016, Developed and executed a Science Café workshop at the Museum of Science and Industry on Microfluidics.
2015, Organized Chemical & Biological Engineering departmental park clean-up for Earth Day
2015, Organized Chemical & Biological Engineering departmental Clothing and Food Drive
2014, Organized Chemical & Biological Engineering departmental holiday card making night for Cards For Hospitalized Kids
2014-2016, Presenter and High School Demonstration, International Institute of Nanotechnology

Activities:
Massachusetts Institute of Technology Varsity Football 2009-2011
Boy Scouts of America, Eagle Scout
Music: Tenor Sax, Piano, and Guitar
Guitarist and songwriter for the band Reaching For Titan
ACS: American Chemical Society
AIChE: American Institute of Chemical Engineers
Brother of the Sigma Tau Chapter of Delta Kappa Epsilon
Northwestern Chemical Engineering Graduate Student Forum (GSF) Committee Member 2014-2015 (organizer of departmental community service and social events)

Teaching: Graduate Earth & Planetary Sciences Forming a Habitable Planet Guest Lecturer Spring 2017
Masters of Science in Biotechnology Bioprocess Engineering Teaching Assistant Fall 2016
Graduate Earth & Planetary Sciences Outer Solar System Satellites Guest Lecturer Winter 2016
Undergraduate Chemical and Biological Engineering Thermodynamics Teaching Assistant Fall 2015
Graduate Chemical and Biological Engineering Advances in Biotechnology Teaching Assistant Spring 2015
Masters of Science in Biotechnology Laboratory Teaching Assistant Spring 2014
MIT Chemical Engineering Grader Spring 2013

Specialty Lab Equipment Skills: Scanning Electron Microscope, Transmission Electron Microscopy, DifferentialPulse Voltammetry, Cyclic Voltammetry, Nuclear Magnetic Resonance, Atomic-Force Microscopy, Thermogravimetric Analysis, Differential Scanning Calorimetry, Spectrofluorometry, HighPerformance Liquid Chromatography, Critical Micelle Concentration, Polymerase Chain Reaction, DNA Electrophoresis, Western Blot, GelPermeation Chromatography, Gas Chromatography Mass Spectrometry, ImageJ, Confocal Microscope, Dip-pen Nanolithography, PolymerPen Lithography, Beam Pen Lithography, Photolithography, Plasma-enhanced Chemical Vapor Deposition, Atomic Layer Deposition, Focused Ion Beam, Plasma Cleaner, Profilometer, E-beam Evaporator, Desktop Scanning Electron Microscope, Electrospraying, Spray Coating, Spin Coating, Column Chromatography, Matlab, SuperPro Design, Aspen Plus, National Renewable Energy Laboratory's System Advisor Model, Labview, Modules for Experiments in Stellar Astrophysics, Java

Photography: Nikon Small World Competition Top 100 Winning Image 2016
Northwestern University Science in Society Image Contest 2016 Honorable Mention
Northwestern University Science in Society Image Contest 2015 2nd Place
NUANCE Center Fall 2016 Image Gallery Honorable Mention
Northwestern University Science in Society Image Contest 2015 2nd Place
NUANCE Center Spring 2015 Image Gallery Honorable Mention
Viewbug Staff Winter Selection 2015,
Partial Solar Eclipse Photo published in Space.com October 24, 2015